

[Ru(bpy)₃]^{2+*} and other remarkable metal-to-ligand charge transfer (MLCT) excited states*

David W. Thompson¹, Akitaka Ito^{2,†}, and Thomas J. Meyer^{2,‡}

¹*Department of Chemistry, Memorial University of Newfoundland, St. John's, Newfoundland A1B 3X7, Canada;* ²*Department of Chemistry, The University of North Carolina at Chapel Hill, Chapel Hill, NC 27599-3290, USA*

Abstract: In 1974, the metal-to-ligand charge transfer (MLCT) excited state, [Ru(bpy)₃]^{2+*}, was shown to undergo electron transfer quenching by methylviologen dication (MV²⁺), inspiring a new approach to artificial photosynthesis based on molecules, molecular-level phenomena, and a “modular approach”. In the intervening years, application of synthesis, excited-state measurements, and theory to [Ru(bpy)₃]^{2+*} and its relatives has had an outsized impact on photochemistry and photophysics. They have provided a basis for exploring the energy gap law for nonradiative decay and the role of molecular vibrations and solvent and medium effects on excited-state properties. Much has been learned about light absorption, excited-state electronic and molecular structure, and excited-state dynamics on timescales from femtoseconds to milliseconds. Excited-state properties and reactivity have been exploited in the investigation of electron and energy transfer in solution, in molecular assemblies, and in derivatized polymers and oligoprolines. An integrated, hybrid approach to solar fuels, based on dye-sensitized photoelectrosynthesis cells (DSPECs), has emerged and is being actively investigated.

Keywords: excited-state chemistry; metal-to-ligand charge transfer; photochemistry; tris(bipyridine)ruthenium(II) cation.

INTRODUCTION

The metal-to-ligand charge transfer (MLCT) excited states of [Ru(bpy)₃]²⁺ (bpy is 2,2'-bipyridine) and related polypyridyl complexes of Rh^{III}, Ir^{III}, Ru^{II}, Os^{II}, and Re^I have a notable history and outsized impact in photochemistry and photophysics [1–7]. The impact is clear, evidenced by 10 000s of publications to date and a wide range of applications in sensing, displays, electroluminescence, electrochemiluminescence, photoelectrochemistry, and artificial photosynthesis [8–12]. MLCT excited states have crossed the divide between theory and experiment with the results of time-dependent perturbation theory applied to excited-state dynamics and spectroscopic measurements providing deep insight into excited-state electronic and molecular structure and the role that they play in excited-state reactivity and dynamics.

Pure Appl. Chem.* **85, 1257–1513 (2013). Paper based on the acceptance lecture for the 2012 Porter Medal, presented at the XXIVth IUPAC Symposium on Photochemistry, Coimbra, Portugal, 15–20 July 2012.

[†]Current address: Department of Chemistry, Graduate School of Science, Osaka City University, Osaka 558-8585, Japan

[‡]Corresponding author

Coordination chemistry

Progress has come by integrating synthesis, excited-state measurements, and theory. The synthetic chemistry of Ru^{II} and Os^{II} polypyridyl complexes begins in the 1940s and 1950s in a series of papers by Dwyer, Gyarfás, and their co-workers, including Alan Sargeson and David Buckingham. They developed synthetic routes and established a systematic basis for the coordination chemistry [13–20]. Synthesis was further elaborated at The University of North Carolina at Chapel Hill, in the 1970s, notably by Pat Sullivan, and has been extended since by many with notable contributions, for example, by Constable, Balzani, and others [21–26].

The properties of these second- and third-row transition metal $d\pi^6$ complexes are ideal for studies of excited states and electron transfer. Their electronic configurations and the large ligand-field splittings between $d\pi$ and $d\sigma^*$ orbitals (t_{2g} and e_g in O_h symmetry) inhibit ligand substitution. Slow ligand exchange poses a challenge for synthesis but, once complexes are made, they are stable which is essential for studies in photochemistry and electron transfer. For polypyridyl complexes of Ru and Os, coordinative stability extends to other electronic configurations, to $d\pi^5$ and $d\pi^4$ complexes of M^{III} and M^{IV}, and even to $d\pi^3$ complexes of M^V [27,28]. Coordinative stability for non-macrocyclic ligand systems is lost for analogous first transition metal complexes of Fe. For Fe^{II}, the ligand-field splitting between $d\pi$ and $d\sigma^*$ orbitals is decreased by ~30 % compared to Ru. Barriers to ligand substitution are lower and lability greater, which causes a loss of coordinative stability and ligand scrambling.

In strong field ligand environments, notably with backbonding CO ligands, spectroscopically accessible MLCT excited states exist in complexes of other $d\pi^6$ metals such as $[M(\text{bpy})(\text{CO})_4]$ (M = Mo, W) and $[\text{Re}(\text{bpy})(\text{CO})_3(\text{py})]^+$ (py is pyridine). Because of their low oxidation states, stabilization of the $d\pi$ levels by backbonding to CO is required for stability and for creating an appropriate $d\pi-\pi^*(\text{bpy})$ energy gap for accessing lowest-lying MLCT excited states. However, oxidation of these complexes and loss of $d\pi-\pi^*_{\text{CO}}$ backbonding labilizes the CO ligands leading to coordinative instability limiting their use in electron-transfer and excited-state applications [7,29,30].

Coordinative stability in multiple oxidation states for Ru and Os has provided a remarkably rich, high oxidation-state chemistry for these metals, largely oxo-based $d\pi^4$, $d\pi^3$, and $d\pi^2$ M^{IV}, M^V, and M^{VI} oxo and di-oxo complexes [27,28,31]. The polypyridyl ligands are also redox active based on low-lying π^* acceptor levels on the ligands. These levels provide the electronic basis for intramolecular charge transfer and the appearance of accessible MLCT excited states.

Coordinative stability has provided a basis for controlled synthetic modification and with it, the use of synthesis to modify and control light absorption and excited-state properties and excited-state electron and energy transfer systematically. Ligand-based organic synthesis has opened the door to multiple linkage strategies for incorporating MLCT excited states into preformed polymers and peptides, and in ligand-bridged molecular assemblies [32]. Related strategies have been employed to link ground-state precursors to the surfaces of conductors and semiconductors where they provide the light absorption/injection/electron transfer properties at the heart of device applications in dye-sensitized solar cells (DSSCs) and dye-sensitized photoelectrosynthesis cells (DSPECs).

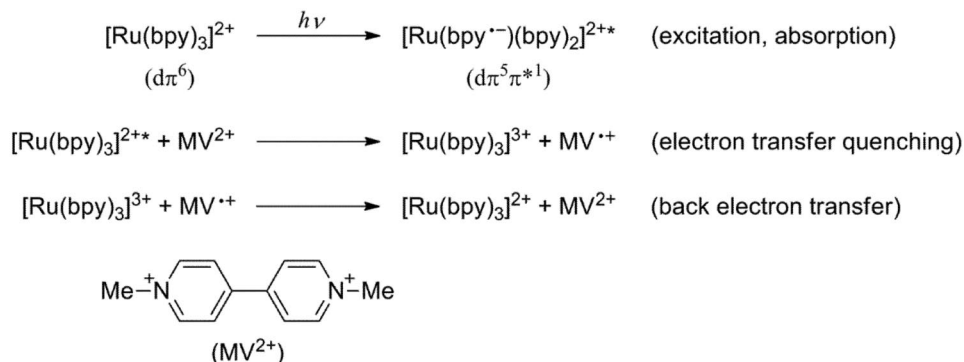
Why are MLCT excited states of interest?

In the early 1970s, Fujishima and Honda made a remarkable discovery [33]. They reported that direct band gap excitation of anatase TiO₂ with an applied bias in a photoelectrochemical cell (PEC) resulted in water splitting into hydrogen and oxygen. Although limited to UV excitation, their observation was provocative in suggesting a way to mimic the natural photosynthetic apparatus in using sunlight to create high energy fuels through “artificial photosynthesis”.

In 1974, excited-state electron transfer by $[\text{Ru}(\text{bpy})_3]^{2+*}$ was first reported [34]. Excited-state electron transfer had been developed earlier by Weller and co-workers for organic excited states in a series of studies [35], and Adamson and co-workers had suggested that excited-state quenching of

[Ru(bpy)₃]^{2+*} by Co^{III} ammine complexes occurred by electron transfer earlier [36], but their results could also be explained by energy transfer.

Electron-transfer quenching of [Ru(bpy)₃]^{2+*} by methylviologen dication, MV²⁺, Scheme 1, was demonstrated at UNC by use of conventional flash photolysis [37]. Excitation of dπ⁶ [Ru(bpy)₃]²⁺ gave the ³(dπ⁵π*_{bpy}¹) MLCT excited state, [Ru(bpy)₃]^{2+*}, and it was sufficiently long-lived, ~1 μs, to undergo diffusional electron-transfer quenching by MV²⁺, Scheme 1.



Scheme 1 Photochemical events in the electron-transfer quenching of [Ru(bpy)₃]^{2+*} by MV²⁺.

The series of reactions in Scheme 1 could be analyzed as the key energy conversion steps underpinning another approach to artificial photosynthesis. In this approach: (i) Molecular-level light absorption by [Ru(bpy)₃]²⁺ to give [Ru(bpy)₃]^{2+*} is a “light-harvesting” step with the incident light transiently stored as excited-state free energy. (ii) Electron transfer quenching of the excited state converts 2.1 eV of excited-state free energy into 1.7 eV of transiently stored redox energy as [Ru(bpy)₃]³⁺ and MV^{•+}. (iii) With their redox potentials—*E*^o = 1.23 V (vs. NHE) for the [Ru(bpy)₃]^{3+/2+} couple and *E*^o = −0.4 V for the MV^{2+/•+} couple—the quenching products are thermodynamically capable of splitting water into hydrogen and oxygen over an extended pH range. This initial observation, and others that soon followed, gave rise to the concepts “chemical approaches to artificial photosynthesis” [8,9,38] and “artificial photosynthesis and solar fuels” with sunlight used to convert water into hydrogen and oxygen or to reduce CO₂ into a reduced carbon source—CO, CH₃OH, or hydrocarbons [12,39,40].

Given its diffusional nature, electron transfer quenching by itself was unproductive. Excitation and quenching are followed by back electron transfer, Scheme 1, and the transiently stored redox equivalents are lost as heat. Exploitation requires integrating a light absorption/electron transfer capability into an architecture where the separate half-reactions for water oxidation and reduction can be driven while minimizing competition from back electron transfer.

Artificial photosynthesis. Attempts to carry out artificial photosynthesis and implement new energy technology strategies have taken on a new sense of urgency driven by the goals of energy security and a sustainable energy future and concerns about environmental damage from the use of hydrocarbon fuels. Photosynthesis in green plants is an inspiration, but also an object lesson in complexity. It is amazingly complex with 5 integrated, membrane-bound assemblies—photosystem I (PSI), photosystem II (PSII), ... —involving thousands of atoms bound in the thylakoid membrane of chloroplasts with the external Calvin cycle used for CO₂ reduction and has remained unchanged for 2.4 B years.

Water oxidation occurs at the reaction center in PSII [33,41–52]. In the first step, the antenna complex sensitizes a chlorophyll excited state, ¹P₆₈₀^{*}, triggering a cascade of five coupled electron-transfer events with timescales ranging from ps to μs. The net result of electron transfer quenching is to drive electron transfer from the oxygen evolving complex (OEC) in the reaction center over a distance of ~50 Å to plastoquinone to give the semiquinone PQ^{•−} (Q_B^{•−}) for later transport to PSI as the

hydroquinone, PQH₂. At this distance, back electron transfer is sufficiently slow that it does not interfere with the water oxidation cycle, which requires three more photon activation steps and three additional oxidative equivalents to reach the OEC and O₂ production to occur [49].

There is a need for a far simpler approach or approaches that can be implemented on vast scales with inexpensive materials in accessible architectures while minimizing environmental impact and overcoming complications from longevity, production, and distribution. At the device level, the basic principles are understood: light absorption; excited-state electron transfer; separation of electron transfer generated oxidative and reductive equivalents by free energy gradients; electron transfer activation of catalysts for multi-electron, multi-proton solar fuel half-reactions; integration/incorporation in a working device.

“Chemical approaches to artificial photosynthesis” based on a “modular approach” provides a way to meet these challenges based on molecular excited states and molecular assemblies [8,9,53]. The modular approach offers the advantage of investigating individual components for light absorption, etc., maximizing their performance, and integrating them into appropriate architectures. The modular approach offers the advantages of rapid iteration by chemical synthesis and the ability to study individual components separately [53–55].

ELECTRONIC STRUCTURE

The major focus of this account is to summarize what we know about the ubiquitous excited state, [Ru(bpy)₃]^{2+*}, and its cousins, and what makes them behave as they do. At first glance, the story seems simple. Following visible near-UV excitation of [Ru(bpy)₃]²⁺, [Ru(bpy)₃]^{2+*} appears, seemingly as a single excited state, sufficiently long-lived to be at equilibrium with its surroundings with its own characteristic free energy content (2.19 eV) and redox potentials with $E^{\circ} = 0.85$ V (vs. SCE in CH₃CN at $I = 0.1$ M) for the excited state as an oxidant at room temperature, [Ru(bpy)₃]^{2+*} + e⁻ → [Ru(bpy)₃]⁺, and $E^{\circ} = -0.92$ V (vs. SCE in CH₃CN at $I = 0.1$ M), for the excited state as a reductant, [Ru(bpy)₃]³⁺ + e⁻ → [Ru(bpy)₃]^{2+*}, (“MLCT Excited States: Redox Potentials” section). As described in the “Excited-State Reactions” section, excited-state redox potentials for [Ru(bpy)₃]^{2+*} have been estimated by a kinetic quenching technique with application of electron-transfer theory [56], or, more straightforwardly, by a Franck–Condon analysis of emission band shapes as described in the “MLCT Excited States: Redox Potentials” section [57,58].

However, as we will see below, describing [Ru(bpy)₃]^{2+*} as a single state is deceiving. Its electronic structure is remarkably complex.

A room temperature absorption spectrum in CH₃CN is shown in Fig. 1 [59]. Visible light absorption is dominated by MLCT transitions of relatively high absorptivity, with molar extinction coefficients in the 10 000s M⁻¹ cm⁻¹. Light absorption into these transitions gives MLCT excited states that are largely singlet in character, $^1(d\pi^6) \xrightarrow{h\nu} ^1(d\pi^5\pi^{*1})$. Although difficult to discern for [Ru(bpy)₃]²⁺, a low absorptivity shoulder also appears on the low-energy (long-wavelength) side of the lowest-energy MLCT absorption band manifold. It arises from a direct MLCT transition from the ground state to a lowest-energy MLCT triplet state (or states, see below), $^1(d\pi^6) \xrightarrow{h\nu} ^3(d\pi^5\pi^{*1})$ (MLCT(1)), to give the “[Ru(bpy)₃]^{2+*}” by direct excitation. From spectroscopic measurements, the energy splitting between the lowest ($d\pi^5\pi^{*1}$) singlet and triplet states is 1700 cm⁻¹ [60].

In the spectrum in Fig. 1a, an additional MLCT band appears in the near-UV between 300 and 350 nm. It arises from a second set of MLCT transitions to the π^*_2 level on the bpy ligands, $^1(d\pi^6) \xrightarrow{h\nu} ^3(d\pi^5\pi^{*2}_1)$ (MLCT(2)). The corresponding triplets for these bands appear at lower-energy and are masked by overlapping absorptions. Absorptivity in the UV is dominated by ligand-based $\pi \rightarrow \pi^*$ transitions.

The band shapes of the MLCT absorption bands include contributions from multiple vibronic contributors. These bands are largely broadened into single, broad absorption bands at room temperature with evidence for vibronic structure. Figure 1b shows the results of a single-mode Franck–Condon

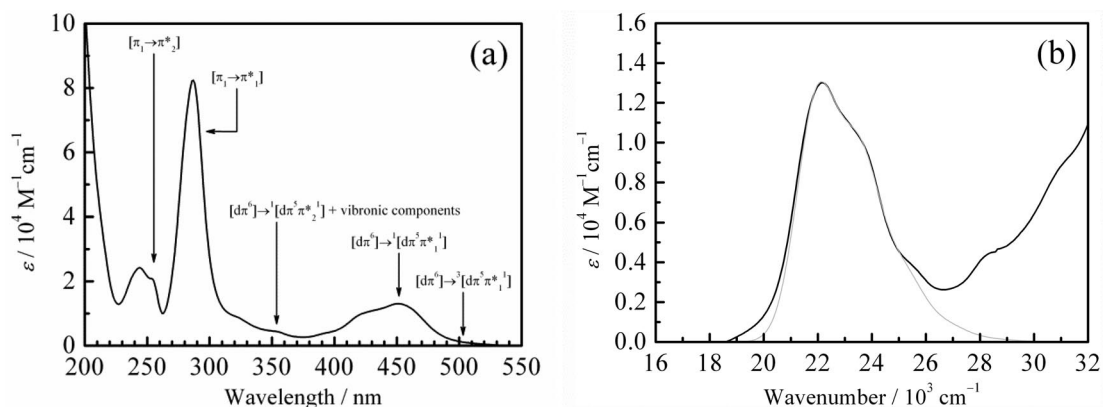


Fig. 1 Absorption spectrum of [Ru(bpy)₃](PF₆)₂ in CH₃CN at room temperature (a) and enlargement for its MLCT absorption band (black in (b)). Gray curve represents the one-mode Franck–Condon theoretical fit with $E_0 = 21\,940\text{ cm}^{-1}$, $\Delta\bar{\nu}_{1/2} = 1770\text{ cm}^{-1}$, $\hbar\omega = 1610\text{ cm}^{-1}$, and $S = 0.68$. See the “MLCT Excited States: Molecular Structure” section for details.

analysis of the low-energy MLCT band, which gives the characteristic parameters E_0 , the $\nu = 0$ to $\nu^* = 0$ energy gap, the vibrational spacing, $\hbar\omega$, and the band width at half-maximum, $\Delta\bar{\nu}_{1/2}$. The spectral fitting procedure will be discussed in more detail for emission in the “Emission spectral fitting” section. At lower temperatures, dramatically at 4.2 K in single crystals, a complex vibronic structure appears in the spectra [61,62]. As discussed in the “MLCT Excited States: Molecular Structure” section, it arises from a series of coupled medium-frequency $\nu(\text{bpy})$ modes with Ru–N and bpy ring torsional modes contributing at lower frequency.

The appearance of nominally spin-forbidden $^1(d\pi^6) \xrightarrow{h\nu} ^3(d\pi^5\pi^*1)$ transitions in the absorption spectrum of [Ru(bpy)₃]²⁺ is due to spin-orbit coupling. Spin-orbit coupling mixes orbital and spin character in the electronic wave functions with the extent of singlet character dictating absorptivity. Singlet-triplet mixing depends on the square of the spin-orbit coupling constant, ζ , which for Ru and Os are $\zeta_{\text{Ru}} = 1100\text{ cm}^{-1}$ and $\zeta_{\text{Os}} = 3000\text{ cm}^{-1}$. Spin-orbit coupling results in 10 % singlet character in the lowest “³MLCT” state for [Ru(bpy)₃]^{2+*}, ~30 % for [Os(bpy)₃]^{2+*}. Its impact on absorption spectra is illustrated by the comparison between [Ru(bpy)₃]²⁺ and two Os^{II} complexes in Fig. 2. The greatly enhanced $^1\text{GS} \rightarrow ^3\text{MLCT}$ absorptivities for the Os^{II} complexes is due to the dependence of the transition dipole on ζ^2 [60,63].

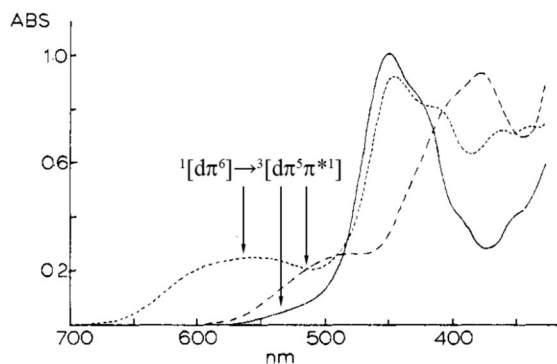


Fig. 2 Absorption spectra in CH₃CN illustrating the low-energy $^1[(d\pi)^6] \rightarrow ^3[(d\pi)^5(\pi^*)^1]$ transitions for [Ru(bpy)₃](PF₆)₂ (solid curve), [Os(bpy)₂(Ph₂PCH₂PPh₂)](PF₆)₂ (broken curve), and [Os(bpy)₂(CH₃CN)₂](PF₆)₂ (dotted curve). Adapted from ref. [59].

A closer look: Multiple MLCT states and transitions

A coordinate axis system for $[\text{Ru}(\text{bpy})_3]^{2+*}$ is shown in Fig. 3. It illustrates the three bpy ligands, labeled as p , q , r , with the excited electron in the lowest triplet MLCT state— $^3(\text{d}\pi^5\pi^*1)$ $^3\text{MLCT}$ —in π^*_1 of bpy ligand p . The corresponding hole in $\text{d}\pi^5$ is shown aligned along the π^* acceptor where it maximizes electrostatic interactions with the excited electron.

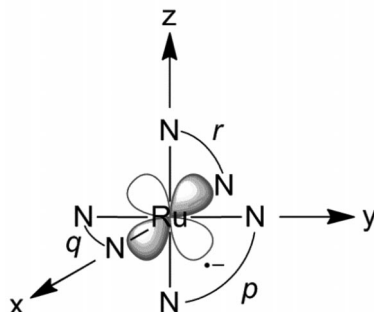


Fig. 3 Coordinate axis system for $[\text{Ru}(\text{bpy})_3]^{2+}$ illustrating the bpy ligands— p , q , r —and the lowest-energy MLCT state with the $\text{d}\pi^5$ hole aligned along the electron acceptor ligand p .

Figure 3 illustrates the donor/acceptor orbital pair for the lowest of three degenerate $^3\text{MLCT}$ states, $^3\text{MLCT}(1)$. With the excited electron held at bpy p , there are two additional MLCT excited states at higher energy. In these states, $^3\text{MLCT}(1')$ and $^3\text{MLCT}(1'')$, the hole in the $\text{d}\pi^5$ core is rotated away from the electron in the acceptor bpy ligand. As noted below in Fig. 4, these states lie ~ 600 and ~ 900 cm^{-1} above $^3\text{MLCT}(1)$ for $[\text{Os}(\text{phen})_3]^{2+*}$ (phen is 1,10-phenanthroline). For all three states, the labels 1, 1', 1'' refer to occupation of the lowest $\pi^*(\text{bpy})$ level on one of the three bpy ligands with the hole in one of three different $\text{d}\pi$ level.

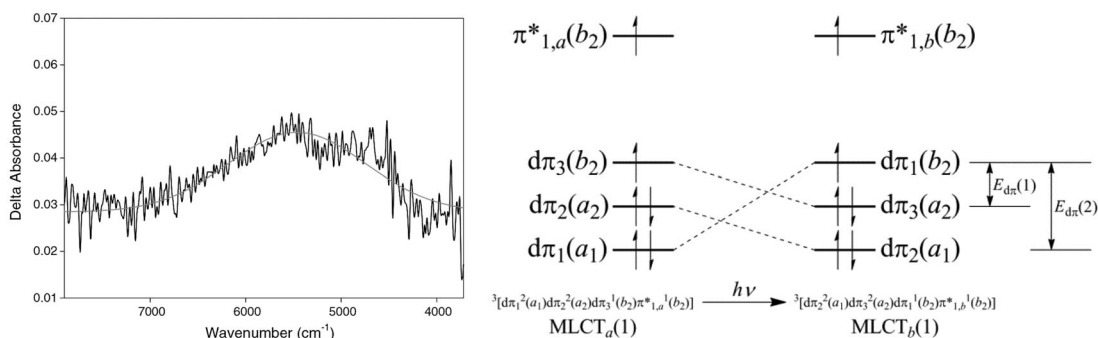


Fig. 4 Transient near-IR spectrum of $[\text{Os}(\text{phen})_3]^{2+}$ in CD_3CN at 298 K (obtained 20–40 ns after 450-nm laser flash excitation) and energy diagram illustrating the orbital basis for the low-energy $^3\text{MLCT}(1) \rightarrow ^3\text{MLCT}(1)$ absorption at 5460 cm^{-1} . Spectrum adapted from ref. [64].

The electronic structure of $[\text{Ru}(\text{bpy})_3]^{2+*}$ is further complicated by the presence of three iso-energetic π^* acceptor levels—on the separate bpy ligands, bpy_p , bpy_q , and bpy_r , labeled as p , q , and r in the original drawing in Fig. 3. Consequently, in $[\text{Ru}(\text{bpy})_3]^{2+*}$ there are *three* degenerate lowest-lying $^3\text{MLCT}(1)$ states, $^3\text{MLCT}_a(1)$, $^3\text{MLCT}_b(1)$, and $^3\text{MLCT}_c(1)$. The added labels define the bpy ligand occupied by the excited electron. Each of these states has two additional higher-energy states with the

hole rotated away from the excited electron, ³MLCT_a(1'), etc. and ³MLCT_a(1''), etc. All told, there are three lowest-energy, degenerate MLCT excited states and *six more MLCT states* sufficiently low-lying to be appreciably populated at or near room temperature and contribute to excited-state properties.

As shown in Fig. 4, there is experimental evidence for multiple MLCT excited states. It shows a transient near-IR spectrum obtained following laser flash MLCT excitation of [Os(phen)₃]²⁺ in CD₃CN [64]. In the spectrum of the MLCT ³(dπ⁵π*¹) excited state(s), characteristic transient features appear in the visible including a broad bleach with λ_{min} = 440 nm arising from loss of ground-state Os^{II} → phen MLCT absorption. A low intensity feature also appears at λ_{max} ~ 600 nm from (phen^{•-}) → Os^{III} ligand-to-metal charge transfer (LMCT) [65]. As shown in Fig. 4, in addition to the visible absorption features, a new, Gaussian-shaped band appears in the near-IR at λ_{max} = 1830 nm ($\tilde{\nu}$ = 5460 cm⁻¹) with ε_{max} ≥ 5000 M⁻¹ cm⁻¹ and Δ $\tilde{\nu}$ _{1/2} = 1840 cm⁻¹ [64]. Transient absorption measurements show that this absorption feature decays exponentially with *k* = 6.1 × 10⁶ s⁻¹ (τ = 160 ns) in reasonable agreement with *k* = 8.3 × 10⁶ s⁻¹ (τ = 120 ns) for [Os(phen)₃]^{2+*} excited-state decay by transient emission measurements.

Consistent with the electronic structure model and Fig. 4, the near-IR band at 5460 cm⁻¹ for [Os(phen)₃]²⁺ can be assigned to a composite of three overlapping transitions that interconvert the low-lying MLCT states in [Os(phen)₃]^{2+*}; ³MLCT(1), ³MLCT(1'), and ³MLCT(1''). All three are spin-allowed, triplet–triplet transitions with the spin character of the excited states highly mixed by spin-orbit coupling.

- At low energy, there is a contribution from degenerate inter-MLCT transitions, ³MLCT_a(1) $\xrightarrow{h\nu}$ ³MLCT_b(1) — ³(dπ₁²dπ₂²dπ₃¹π*_{1,a}¹) $\xrightarrow{h\nu}$ ³(dπ₂²dπ₃²dπ₁¹π*_{1,b}¹) — and ³MLCT_a(1) $\xrightarrow{h\nu}$ ³MLCT_c(1). These transitions result in net dipole rotation and interconversion between the three components of ³MLCT(1). For ³MLCT_a(1) $\xrightarrow{h\nu}$ ³MLCT_b(1), simultaneous transfer of electrons occurs from dπ₁ to dπ₃ and π*_{1,a} to π*_{1,b}.
- At intermediate energy, excitation results in electron transfer from π*_{1,a} to π*_{1,b}, π*_{1,c} with the hole unchanged — ³(dπ₁²dπ₂²dπ₃¹π*_{1,a}¹) $\xrightarrow{h\nu}$ ³(dπ₁²dπ₂²dπ₃¹π*_{1,b}¹). This is a ligand-to-ligand charge transfer (LLCT) transition with conversion from ³MLCT(1) to ³MLCT(1').
- At still higher energy, excitation of ³MLCT(1) to ³MLCT(1'') occurs — ³(dπ₁²dπ₂²dπ₃¹π*_{1,a}¹) $\xrightarrow{h\nu}$ ³(dπ₁²dπ₂¹dπ₃²π*_{1,b}¹). This transition also involves simultaneous dπ → dπ and π* → π* electron transfer and dipole rotation.

The intensity of the absorption band at 5460 cm⁻¹ is dominated by the LLCT transition since it involves single electron excitation and has significant radial character. It is fully allowed with its intensity dependent on the extent of π*_{1,a}–π*_{1,b} electronic wave function mixing through Os^{III}.

Splitting the triplet states

There is an additional complication based on the nominal “triplet” character of the lowest MLCT state(s). As shown by Crosby and co-workers, from temperature-dependent emission lifetime measurements, the lowest ³MLCT “state” is really a manifold of three states. Each of the ³MLCT(1) states, ³MLCT_a(1), etc., are further split by electron-exchange interactions and spin-orbit coupling into three sublevels [66]. Based on a theoretical analysis by Kober et al. [60,67], the lowest of the three is a pure spin triplet with the additional sublevels lying 10 and 61 cm⁻¹ higher in energy [68].

Low-temperature spectra

The complexity of excited-state structure is further shown in the polarized, 8 K single crystal spectra in Fig. 5. Also shown in Fig. 5 is a molecular orbital scheme used to fit the spectra. Based on the results of this analysis, transitions to 24 excited states of varying singlet and triplet character, split by spin-orbit coupling and electron exchange appear in the visible MLCT spectrum [60].

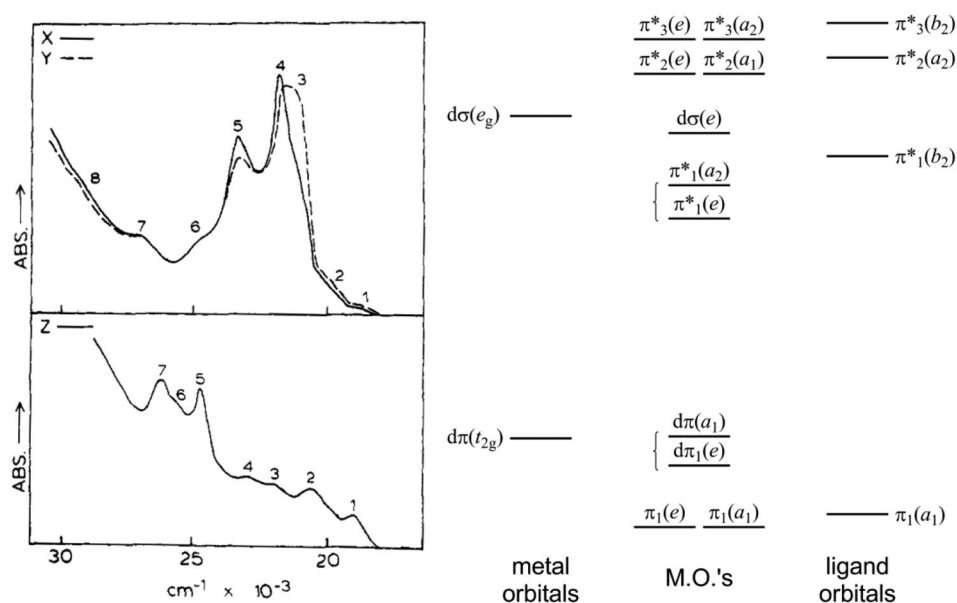


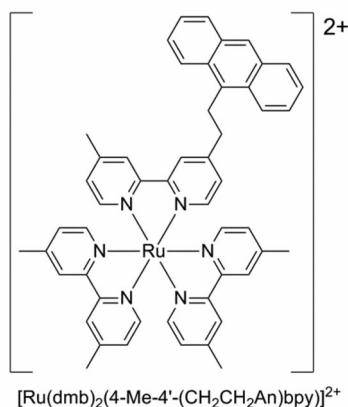
Fig. 5 Polarized absorption spectra for $[\text{Ru}(\text{bpy})_3]^{2+}$ in a single crystal at 8 K and the energy level scheme used to assign the spectra, adapted from ref. [60].

What exactly is $[\text{Ru}(\text{bpy})_3]^{2+*}$?

The results of the analysis of electronic structure are both revealing and disconcerting. What we commonly refer to as “ $[\text{Ru}(\text{bpy})_3]^{2+*}$ ” is really a manifold of three degenerate $^3\text{MLCT}$ states having different orbital compositions and excited-state dipole orientations. The triplet components of each are further split by spin-orbit coupling and electron-exchange interactions. There are two additional sets of degenerate states— $^3\text{MLCT}(1')$ and $^3\text{MLCT}(1'')$ —populated at or near room temperature.

As discussed in the “Excited-state dynamics: Dipole reorientation and ILET” section, time-dependent polarization measurements show that the degenerate MLCT states are dynamically interconverted with rotation of the excited-state dipole occurring in tens of picoseconds [69]. For most purposes, describing $[\text{Ru}(\text{bpy})_3]^{2+*}$ as the excited state “ $^3\text{MLCT}$ ” with electronic configuration $^3(d\pi^5\pi^*1)$ is adequate. However, in lower-symmetry complexes, containing mixed polypyridyl ligands, e.g., $[\text{Ru}(\text{bpy})(\text{bpy}')(\text{bpy}'')]^{2+}$, additional sets of non-degenerate π^* acceptor orbitals are introduced and the degeneracy among $^3\text{MLCT}$ states is lifted, resulting in more complex excited-state dynamics, potentially influencing excited-state reactivity.

As an example, in molecular assemblies with derivatized ligands having attached substituents for electron or energy transfer, interconversion among the low-energy MLCT states can play a dynamic role. This occurs in the anthracene-derivatized complex, $[\text{Ru}(\text{dmb})_2(4\text{-Me-}4'\text{-(CH}_2\text{CH}_2\text{An)bpy})]^{2+}$ (dmb is 4,4'-dimethyl-2,2'-bipyridine; 4-Me-4'-(CH₂CH₂An)bpy is 4-methyl-4'-(9-anthrylethyl)-2,2'-bipyridine). Analysis of ultrafast absorption-time traces following laser flash excitation in CH₃CN showed kinetic components for the appearance of ^3An on timescales of 23 and 72 ps [65]. In one interpretation of the data, the rapid component arises from excitation along the Ru–bpy–An axis followed by rapid, $^3[\text{Ru}^{\text{III}}(\text{bpy}^*)\text{–An}] \rightarrow [\text{Ru}^{\text{II}}(\text{bpy})]\text{–}^3\text{An}$, energy transfer. The slow component arises from Ru–dmb excitation followed by dipole reorientation, $^3[(\text{bpy}^*)\text{Ru}^{\text{III}}(\text{bpy})\text{–An}] \rightarrow ^3[(\text{bpy})\text{Ru}^{\text{III}}(\text{bpy}^*)\text{–An}]$, and then energy transfer. Dipole reorientation dynamics will be discussed in the “Excited-state dynamics: Dipole reorientation and ILET” section.



Localized or delocalized?

In ³(dπ⁵dπ*¹) [Ru(bpy)₃]^{2+*} there is an inherent mixed-valence character with a single excited electron and three acceptor ligands. This ligand-based mixed-valence character is analogous to the metal-based mixed-valence character found in ligand-bridged mixed-valence complexes such as the famous “Creutz-Taube ion”—[(NH₃)₅Ru(pyrazine)Ru(NH₃)₅]⁵⁺ [70–73].

In one limiting description of [Ru(bpy)₃]^{2+*}, the excited electron is “localized” on a single bpy ligand, [Ru^{III}(bpy^{•-})(bpy)₂]^{2+*}, with a corresponding decrease in symmetry from *D*₃ in the ground state to *C*₂ in the excited state. In the other, the excited electron is delocalized over all three ligands, [Ru(bpy^{1/3-})₃]^{2+*}, with the *D*₃ symmetry of the ground state preserved in the excited state.

The factors dictating localization or delocalization, both experimentally and theoretically, are understood [74–77]. In the absence of electronic coupling between sites, either metal–metal or ligand–ligand, the difference in electron content—between Ru^{II} and Ru^{III} or bpy and bpy^{•-}—causes intramolecular structural differences and polarization changes in the surrounding solvent. With electronic coupling and mixing of electronic wave functions, the excess electron is more equally shared between sites, decreasing these differences. In the classical limit, the transition between localization and delocalization occurs when 2*H*_{DA} > λ with λ the classical reorganization energy, the sum of the intramolecular (λ_i) and solvent reorganization energies (λ_o) in the absence of electronic coupling. *H*_{DA} is the resonance energy. Because of the difference in timescales between the coupled intramolecular and solvent modes, the transition between localized and delocalized can be complex and time-dependent [72,78].

The electronic structure model used to describe [Ru(bpy)₃]^{2+*} assumed localization in the excited state. The question of localization vs. delocalization has been the subject of controversy in the past with different interpretations given to the same sets of data [72,79–82]. Theoretical models have been developed that assume delocalization [83], yet, as noted above, a localized model successfully predicts spectral properties. There is other evidence to support localization.

Solvent dependence

MLCT absorption bands are solvent-dependent. Figure 6 shows a plot of the visible MLCT absorption band maximum for [Ru(bpy)₃]²⁺ (*E*_{max}) plotted vs. the dielectric function in eq. 1 in 19 solvents. The relationship in eq. 1 arises from dielectric continuum theory with application of a “dipole-in-a-sphere” model, which is also illustrated. In this model, the initial *D*₃ symmetry of the ground state is instantaneously maintained in the solvent even after localized MLCT excitation occurs to give the *C*₂ excited state. On the timescale for the optical transition, ~10⁻¹⁵ s, the orientational and translational motions of the surrounding solvent molecules are frozen with only the optical (electron cloud) part of the solvent

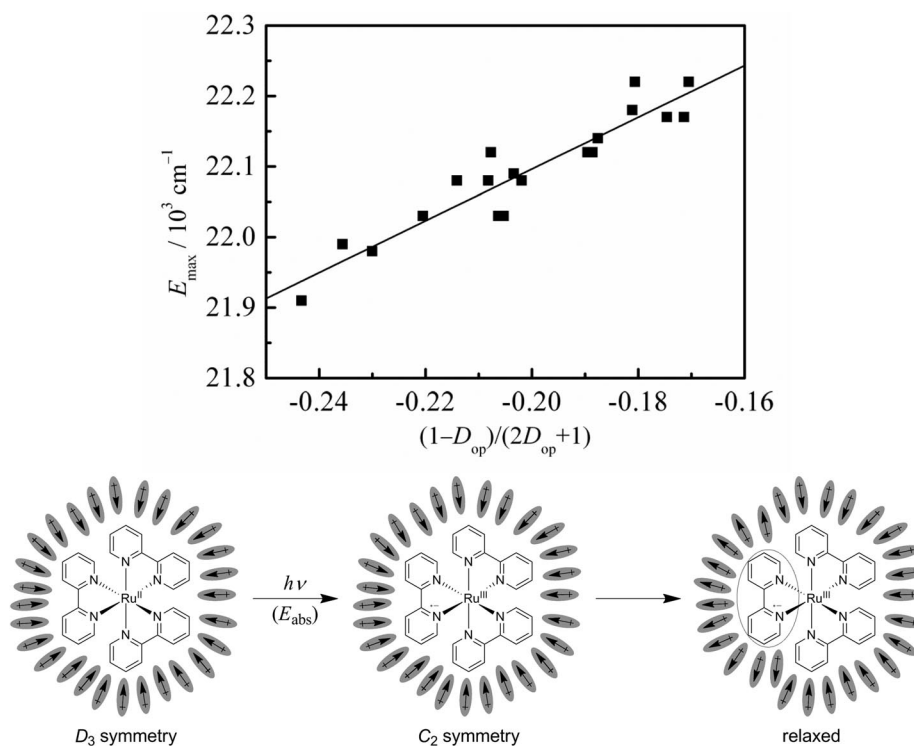


Fig. 6 Effect of solvent on the visible MLCT λ_{\max} for $[\text{Ru}(\text{bpy})_3](\text{PF}_6)_2$ in 19 solvents, showing the variation in E_{\max} with the solvent dielectric function in eq. 1, with a schematic illustration of the “dipole-in-a-sphere” model. Data obtained from ref. [84]. The straight line in the plot represents the linear least-squares best fit with a slope of 3670 cm^{-1} .

dielectric responding. As shown in the figure, following excitation, the solvent polarization reorients to the equilibrium distribution for the thermally relaxed excited state.

In eq. 1, D_{op} is the optical dielectric constant and $\vec{\mu}_{\text{e}}$ the vector dipole moment for the transition. Based on the slope of the solvent dependence in Fig. 6 and eq. 1, $\vec{\mu}_{\text{e}} = 14 \pm 6 \text{ D}$ and the transition length, the vector sum of all vector electronic displacements, is $2.4\text{--}3.0 \text{ \AA}$.

$$\Delta E_{\text{abs}} = \frac{\vec{\mu}_{\text{e}}^2}{a^3} \left(\frac{1 - D_{\text{op}}}{2D_{\text{op}} + 1} \right) \quad (1)$$

Stark (electric field) effect

The results of the Stark effect, electric field, measurements on $[\text{Ru}(\text{bpy})_3]^{2+}$ by Oh and Boxer [85] are also consistent with instantaneous localization and C_2 symmetry in initially excited $[\text{Ru}(\text{bpy})_3]^{2+*}$. Based on an analysis of their data, the charge-transfer distance in the excited state was estimated to be 1.6 \AA . With a center-to-center distance between Ru and the bpy ligand of 3.1 \AA , the extent of charge transfer in the excited state was estimated to be ~ 0.6 [85].

Transient resonance Raman (TR³) and transient infrared (TRIR)

There is direct spectroscopic evidence for localization in thermally equilibrated $^3[\text{Ru}(\text{bpy})_3]^{2+*}$ in H_2O and CH_3CN based on the results of transient resonance Raman measurements, initially by Woodruff et al. [86]. In these experiments, Raman scattering, with resonance enhancement from the $\pi \rightarrow \pi^*(\text{bpy}^{\bullet-})$ absorption of the excited state at 355 nm was observed for a series of mid-IR $\nu(\text{bpy})$ bands from 900 to

1700 cm⁻¹. Raman band shifts to lower energy were observed consistent with localization on a single bpy ligand in the excited state [87,88].

The results of a transient mid-infrared (TRIR) study on [Ru(phen)₃]^{2+*} from 1450 to 1800 cm⁻¹ on the nanosecond time in CD₃CN [89] are shown in Fig. 7. This figure shows ground-state (top) and transient absorption difference spectra (bottom). There is clear evidence for localization in the difference spectrum. For example, a band at 1413 cm⁻¹ splits into components at 1408 and 1421 cm⁻¹ in the excited state consistent with both phen and phen^{•-} and the localized description [Ru(phen^{•-})(phen)₂]^{2+*} rather than [Ru(phen^{1/3-})₃]^{2+*}.

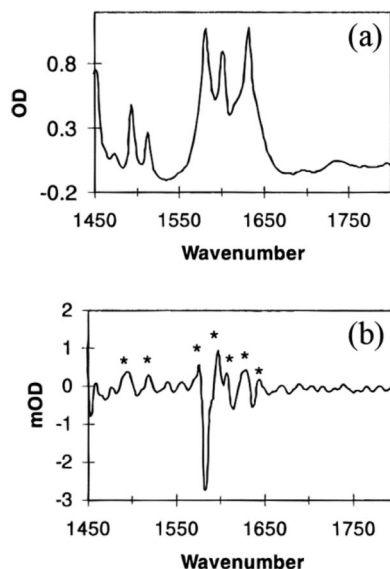


Fig. 7 Ground-state (a) and TRIR difference spectra (b) of [Ru(phen)₃](PF₆)₂ in CD₃CN at 298 K. Adapted from ref. [89].

CONTROLLING LIGHT ABSORPTION: BLACK MLCT ABSORBERS

With the synthetic chemistry in place and a detailed understanding of electronic structure, it is possible to control light absorption and excited-state properties of polypyridyl complexes with a high level of control. The impact of ligand variations on other excited-state properties will be a major theme in future sections. The impact that they can have on light absorption is illustrated in the UV–vis spectra in Fig. 8.

The key to manipulating light absorption lies in the influence of the ligands on the energy gap between donor $d\pi$ and ligand-based π^* acceptor levels, note Scheme 2. σ and π donating ligands—X⁻, OH⁻, ...—mix with metal-based $d\sigma$ and $d\pi$ orbitals increasing their energy which decreases the MLCT energy gap. Backbonding to ligands like CO, CN⁻, and PR₃ stabilizes the $d\pi$ levels increasing the energy gap. Electron-withdrawing substituents on the bpy acceptor ligand(s) (–COOR, –NO₂, ...) decrease the energy gap and electron donor substituents (–NR₂, –R, ...) increase the energy gap.

Given the charge-transfer nature of the absorptions, there is a direct relationship between the absorption energy and redox potentials for metal-based $d\pi^5/d\pi^6$ couples and ligand-based $\pi^*_1^0/\pi^*_1^1$ couples. This concept and the impact of the ligand set on MLCT light absorption and redox potentials have been developed in detail by Lever and co-workers who have provided a systematic basis for predicting spectra and redox potentials based on a series of ligand-defined “Lever parameters” [90–92].

The dramatic effect that ligands can have on spectra is illustrated in Fig. 8 which compares spectra for three complexes—[Ru(bpy)₃]²⁺, [Ru(4,4'-(COOEt)bpy)(dmb)(Et₂dtc)]⁺ (4,4'-(COOEt)bpy is

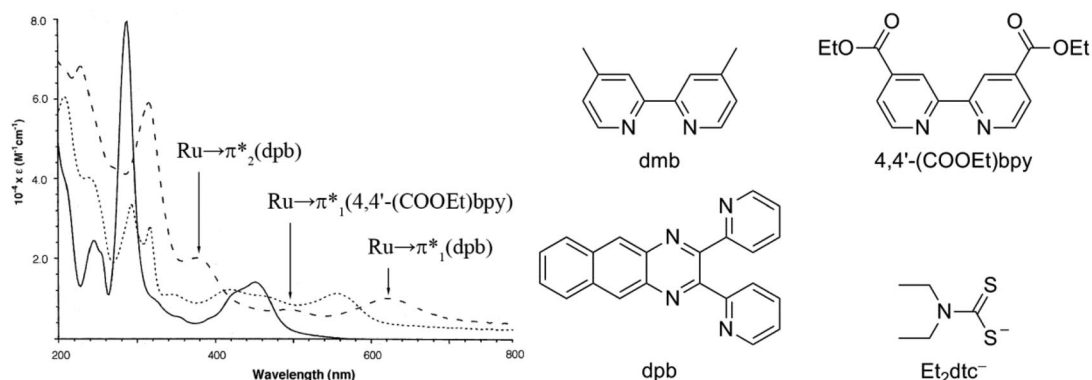
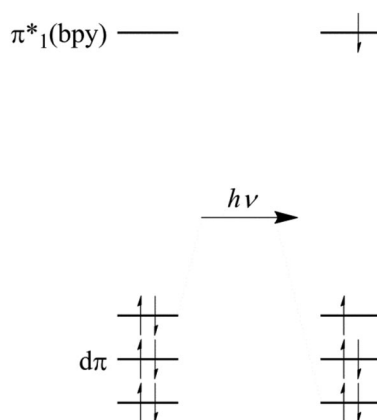


Fig. 8 Absorption spectra of $[\text{Ru}(\text{bpy})_3](\text{PF}_6)_2$ (solid curve), $[\text{Ru}(4,4'-(\text{COOEt})\text{bpy})(\text{dmb})(\text{Et}_2\text{dtc})]\text{PF}_6$ (dotted curve) and $[\text{Ru}(4,4'-(\text{COOEt})\text{bpy})(\text{dpb})(\text{Et}_2\text{dtc})]\text{PF}_6$ (broken curve) in CH_3CN at room temperature (adapted from ref. [94]). Ligand structures and transitions for the dpb complex are also shown.



Scheme 2 Orbital basis for MLCT $d\pi^6 \xrightarrow{h\nu} (d\pi^5\pi^*1)$ absorption.

2,2'-bipyridyl-4,4'-dicarboxylic acid diethyl ester; Et_2dtc^- is diethyldithiocarbamate anion), $[\text{Ru}(4,4'-(\text{COOEt})\text{bpy})(\text{dpb})(\text{Et}_2\text{dtc})]^+$ (dpb is 2,3-bis(2-pyridyl)benzoquinoxaline). Ligand structures are illustrated in the figure [93,94]. Introduction of the withdrawing ester substituents in 4,4'-(COOEt)bpy introduces a low-lying π^* acceptor orbital and the electron-donating dithiocarbamate (dtc^-) anion increases the $d\pi$ energy shifting the lowest-energy MLCT band into the low-energy visible. The dmb ligand introduces a second set of π^* acceptor levels further broadening MLCT absorption.

The dpb complex is a true “black absorber” with light absorption occurring with relatively high absorptivity throughout the visible into the near-IR. Assignment of the prominent visible absorption features is also indicated for this complex in Fig. 8 with absorption dominated by MLCT transitions to $\pi^*_1(\text{dpb})$, $\pi^*_1(4,4'-(\text{COOEt})\text{bpy})$, and $\pi^*_2(\text{dpb})$ at increasingly higher energies [93,94].

MLCT EXCITED STATES: MOLECULAR STRUCTURE

MLCT excitation to $d\pi^5\pi^*1$ $[\text{Ru}^{\text{III}}(\text{bpy}^{\bullet-})(\text{bpy})_2]^{2+*}$ causes partial oxidation at the metal decreasing Ru–N bond distances [95,96]. The results of recent studies using picosecond X-ray absorption spectroscopy on $[\text{Ru}(\text{bpy})_3]^{2+*}$ have revealed that the Ru–N bonds contract by 0.03 Å in the excited state [96]. Oxidation also results in loss of $d\pi-\pi^*(\text{bpy})$ backbonding which partly compensates for increased

σ -bonding in the excited state. Because of this effect, in [Os(bpy)₃](PF₆)₂, the average Os–N bond distance actually *decreases* by 0.010 Å compared to [Os(bpy)₃](PF₆)₃ due to loss of back bonding in Os^{II} [97].

Electron occupation of the antibonding π^*_{bpy} levels in [Ru(bpy)₃]^{2+*} leads to an increase in C–C/C–N bond distances as shown by spectroscopic measurements.

Time-resolved resonance Raman (TR³)

Time-resolved resonance Raman (TR³) measurements on [Os(bpy)₃]²⁺, [Os(bpy)₂(Ph₂PCH=CHPh₂)]²⁺, and [Os(bpy)(Ph₂PCH=CHPh₂)₂]²⁺ by Woodruff and co-workers revealed average excited-ground state shifts for 5 $\nu(\text{bpy})$ modes of –48, –55, and –59 cm^{–1}, respectively [87,88]. Analysis of the data based on Badger's rule, which relates force constants and bond lengths in related structures, gave average C–N/C–C bond distance increases from 0.013 to 0.020 Å in the series. The increase correlates with an increase in energy gap from 14 200 to 20 900 cm^{–1} and is due to an increase in the extent of charge transfer [86]. The phosphine ligands increase the energy gap by stabilizing the $d\pi_{\text{Os}}$ levels in the ground state by metal-to-ligand backbonding.

Emission spectral fitting

As shown in Fig. 9, vibrational structure is observed in the 77 K emission spectrum of [Ru(bpy)₃]^{2+*} in a 4/1 (v/v) EtOH/MeOH glass. The structure is lost in the room temperature spectrum due to thermal broadening. Also illustrated in the figure is the vibronic origin of the structure with transitions from level $\nu^* = 0$ in the excited state to level ν in the ground state.

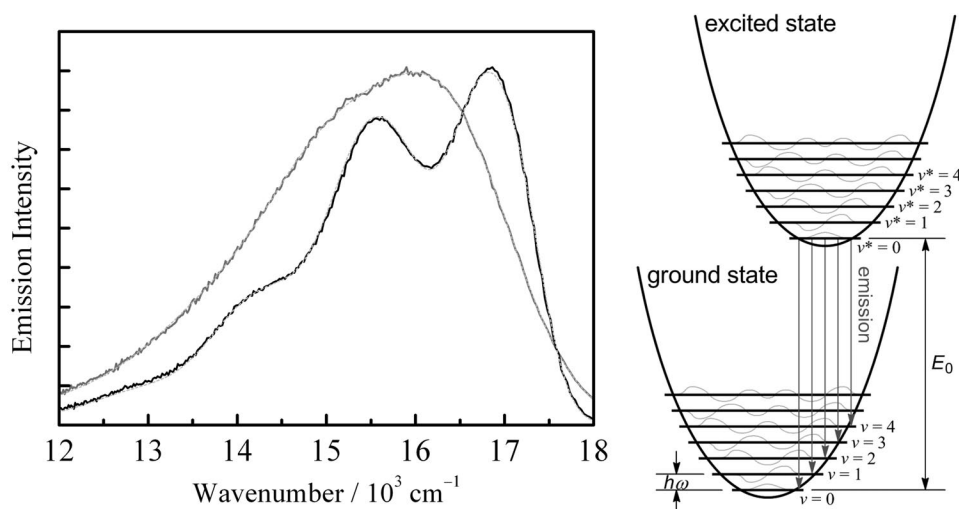


Fig. 9 Corrected emission spectra and spectral fits for [Ru(bpy)₃](PF₆)₂ in a 4/1 (v/v) ethanol/methanol glass at 77 K (black) and in CH₃CN at 298 K (gray). A schematic illustration of the vibronic contributions is also shown. Gray broken curves in the spectra are theoretical fits, see text. For the data at 77 K, a two-mode fit gave $E_0 = 17\,190$ cm^{–1}, $\Delta\bar{\nu}_{1/2} = 690$ cm^{–1}, $\hbar\omega_M = 1380$ cm^{–1} ($S_M = 1.08$), and $\hbar\omega_L = 400$ cm^{–1} ($S_L = 1.41$). For the 298 K spectrum, $E_0 = 16\,370$ cm^{–1}, $\Delta\bar{\nu}_{1/2} = 1740$ cm^{–1}, and $\hbar\omega = 1350$ cm^{–1} ($S = 1.03$).

Information about excited-state structural change is also available by Franck–Condon analysis of spectral profiles. In the limit of a single coupled medium- or high-frequency mode, the emission spectrum is given by eq. 2, which is constructed from a series of vibronic lines of quantum spacing, $\hbar\omega$,

originating from vibrational level $v^* = 0$ in the excited state to levels v in the ground state. The exponential distribution function broadens the lines by including solvent and low-frequency modes treated classically. $\lambda_{o,L}$ is the reorganization energy contributed by the solvent and low-frequency modes, ΔG_{ES} is the free energy of the excited state above the ground state, k_B is the Boltzmann constant, and $hc\tilde{\nu}$ is the energy of the emitted light at $\tilde{\nu}$. The additional constants in eq. 2 are Avogadro's number, N_A , the transition dipole moment, $\bar{\mu}$, and c the speed of light.

$$\int I(\tilde{\nu})d\tilde{\nu} = \frac{8\pi N_A}{3\hbar^3 c^3} \frac{|\bar{\mu}|^2}{(4\pi\lambda_{o,L}k_B T)^{1/2}} \sum_v (|\Delta G_{ES}| - v\hbar\omega - \lambda_{o,L})^3 \exp(-S) \frac{S^v}{v!} \exp\left[-\frac{\{h\tilde{\nu} - (|\Delta G_{ES}| - v\hbar\omega - \lambda_{o,L})\}^2}{4\lambda_{o,L}k_B T}\right] \quad (2)$$

Equation 3 provides a convenient way to analyze emission spectral profiles with $I(\tilde{\nu})$ the ratio of the intensity at $\tilde{\nu}$ to the intensity at the $v^* = 0 \rightarrow v = 0$ energy gap, E_0 . v and $\hbar\omega$ are the vibrational quantum number and quantum spacing and $\Delta\tilde{\nu}_{0,1/2}$ the band width at half-height for the individual vibronic components. S is the electron-vibrational coupling constant or Huang–Rhys factor, defined in eq. 4c [98,99].

$$I(\tilde{\nu}) = \sum_{v=0}^{\infty} \left(\frac{E_0 - v\hbar\omega}{E_0}\right)^3 \left(\frac{S^v}{v!}\right) \exp\left[-4 \ln 2 \left(\frac{\tilde{\nu} - E_0 + v\hbar\omega}{\Delta\tilde{\nu}_{0,1/2}}\right)^2\right] \quad (3)$$

For $[\text{Ru}(\text{bpy})_3]^{2+*}$, a series of 10–12 medium-frequency $\nu(\text{bpy})$ ring-stretching modes, a low-frequency ring-torsional mode, and lower-frequency Ru–N stretching modes are all coupled to the transition between states [100]. Coupled modes are those for which there is a change in equilibrium displacement, ΔQ_e , or quantum spacing between states. In the single, average mode approximation, contributions from the coupled medium-frequency modes are included as averages in S and $\hbar\omega$, eqs. 4, with the sum over vibrational levels v . The electron-vibrational coupling constants are related to the reduced mass, M , angular frequency, ω , and equilibrium displacement as shown in eq. 4c. The averaging procedure is reasonably accurate if the spread in frequencies in the coupled modes is small compared to the average.

$$S = \sum_j S_j \quad (4a)$$

$$\hbar\omega = \sum_j S_j \hbar\omega_j / \sum_j S_j \quad (4b)$$

$$S_j = \frac{1}{2} \left(\frac{M_j \omega_j}{\hbar}\right) (\Delta Q_{e,j})^2 \quad (4c)$$

$$(\Delta\tilde{\nu}_{0,1/2})^2 = 16\lambda_{o,L}k_B T \ln 2 \quad (5)$$

In the single-mode approximation, the band width at half-height is given by eq. 5. It includes contributions from the solvent reorganization energy, λ_o , and coupled low-frequency modes treated classically, λ_L . Application of emission spectral fitting to low-temperature data, such as the resolved vibronic structure for $[\text{Ru}(\text{bpy})_3]^{2+*}$ at 77 K in a EtOH/MeOH glass in Fig. 9 require inclusion of a second, low-frequency mode to account for low-frequency Ru–N stretching and ring torsional vibrations [86,101–106].

Emission spectral fitting was applied to a series of [Os(bpy)(L)₄]²⁺ and [Os(phen)(L)₄]²⁺ complexes with the energy gap varied by changing the ancillary ligands. Over the series, *S* increased linearly from 0.65 to 1.2 as *E*₀ increased from 13 000 to 20 000 cm⁻¹ due to the increasing extent of charge transfer [107].

A similar relationship has been found for a series of Re^I complexes, [Re(bpy)(CO)₃(L)]⁺ (L = py, ...) with *S* increasing from 0.95 at *E*₀ = 14 300 cm⁻¹ to 1.33 at *E*₀ = 18 040 cm⁻¹ [108].

Resonance Raman

The most complete analysis of excited-state structure has come from application of a treatment by Heller to the excitation dependence of resonance Raman band profiles [109–112]. Raman measurements give the frequency of the coupled modes, *v*_{*j*}, and analysis of Raman band profiles *S*_{*j*} allowing for a complete evaluation of the role of individual vibrations on a mode-by-mode basis.

The Heller analysis was applied to the series [Os(bpy)₃]²⁺, [Os(bpy)₂(py)₂]²⁺, and [Os(bpy)(py)₄]²⁺ with 13 coupled *v*(bpy) modes from 1306 to 1006 cm⁻¹, a ring-torsional mode at 662 cm⁻¹, and low-frequency M–L stretching modes at 375 and 280 cm⁻¹ [113]. As shown by the comparisons in Table 1, agreement between *S* and *ħω* values calculated from the mode-by-mode analysis and by spectral fitting is remarkably good. From the data in Table 1, *S* values, and contributions to the structural difference between ground and excited states for [Os(bpy)₃]²⁺, are dominated by *v*(bpy) ring stretching modes at 1558 and 1485 cm⁻¹.

Table 1 Comparison of single mode emission spectral fitting parameters in water at 23 °C obtained by emission spectral fitting and by a mode-by-mode analysis with averaging, see text [112].

| (a) Simplex fitting routine | | | |
|---|---------------------------------------|---|---|
| | [Os(bpy) ₃] ²⁺ | [Os(bpy) ₂ (py) ₂] ²⁺ | [Os(bpy)(py) ₄] ²⁺ |
| <i>E</i> ₀ /cm ⁻¹ | 13 700 | 13 147 | 12 669 |
| <i>ħω</i> _{ave} /cm ⁻¹ | 1300 | 1300 | 1300 |
| <i>S</i> _{ave} | 0.90 | 0.67 | 0.70 |
| Δ <i>V</i> _{0,1/2} /cm ⁻¹ | 1526 | 2017 | 1703 |
| λ ₀ /cm ⁻¹ | 1021 | 1783 | 1271 |
| (b) Average calculated from multi-mode Raman parameters | | | |
| | [Os(bpy) ₃] ²⁺ | [Os(bpy) ₂ (py) ₂] ²⁺ | [Os(bpy)(py) ₄] ²⁺ |
| <i>E</i> ₀ /cm ⁻¹ | 13 650 | 13 200.00 | 12 700.00 |
| <i>ħω</i> /cm ⁻¹ | 1369 | 1370 | 1357 |
| <i>S</i> | 0.87 | 0.83 | 0.70 |
| Δ <i>V</i> _{0,1/2} /cm ⁻¹ | 1799 | 1799 | 1799 |
| λ ₀ /cm ⁻¹ | 1419 | 1419 | 1419 |

Transient Infrared: TRIR [114]

Application of TRIR to localization vs. delocalization in [Ru(phen)₃]^{2+*} was described in the “Localized or delocalized?” section. A TRIR difference spectrum for ³[Re(bpy)(CO)₃(4-Etpy)]⁺ (4-Etpy = 4-ethylpyridine) in CH₃CN from 1850 to 2150 cm⁻¹ on the ns timescale is shown in Fig. 10. A notable feature is the positive shifts in the *v*(CO) bands of 40–80 cm⁻¹ and the change in *v*(CO) band pattern. Both are consistent with the MLCT excited state, [Re^{II}(bpy^{*})(CO)₃(4-Etpy)]⁺. The increase in

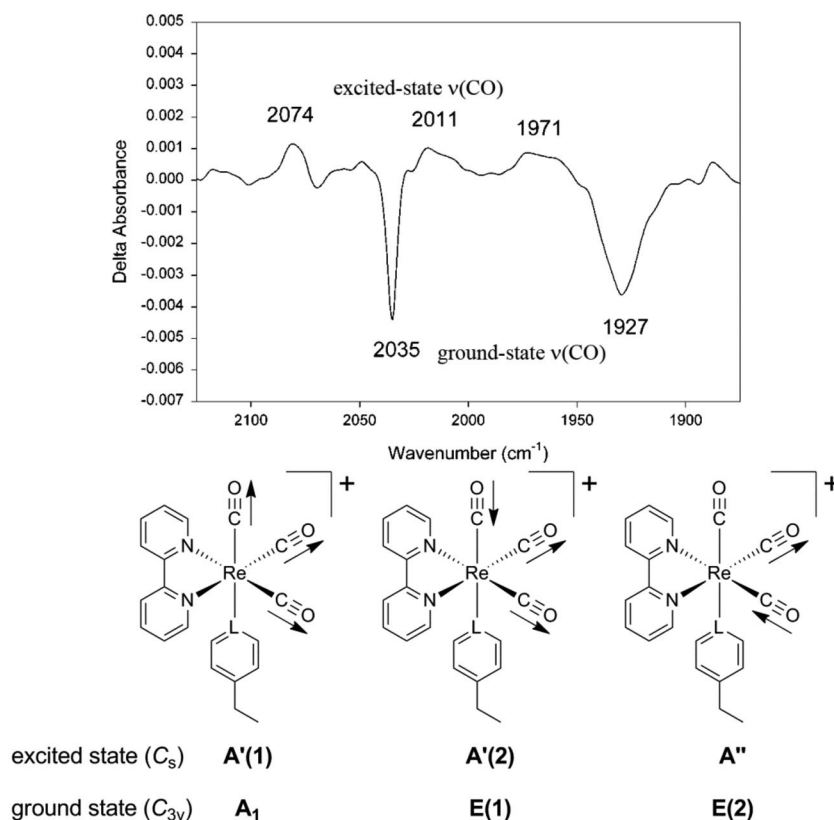


Fig. 10 TRIR difference spectrum, $[\text{Re}^{\text{II}}(\text{bpy}^*)(\text{CO})_3(4\text{-EtPy})]^{+*} - [\text{Re}^{\text{I}}(\text{bpy})(\text{CO})_3(4\text{-EtPy})]^+$, in CD_3CN at room temperature, also illustrating the normal mode compositions of the CO stretching modes. Spectrum adapted from ref. [116].

$\nu(\text{CO})$ band energies is consistent with partial oxidation of Re^{I} to Re^{II} in the excited state with decreased $d\pi_{\text{Re}}-\pi^*_{\text{CO}}$ backbonding. The local mode compositions of the $\nu(\text{CO})$ stretching normal modes are also shown in the figure. The three $\nu(\text{CO})$ band pattern in the excited state from the two-band pattern for the ground state is due to the decrease in local electronic symmetry from $\sim C_{3v}$, with three facial pyridyl ligands, to C_s in the bpy-reduced excited state [115–119].

Density functional theory (DFT) calculations on both ground and excited states for the series *fac*- $[\text{Re}(4,4'\text{-X}_2\text{bpy})(\text{CO})_3(4\text{-EtPy})]^+$ (*fac* is facial; $\text{X} = \text{CH}_3, \text{H}, \text{and } \text{CO}_2\text{Et}$) have been used to show how energy gap variations across the series, influence excited-state geometries and electronic structures. Predicted bond length and angle changes in the excited states point to the importance of $\text{Re}-\text{CO}$ σ -bond polarization and $\pi^*(4,4'\text{-X}_2\text{bpy})-\pi^*(\text{CO})$ mixing [120,121].

Solvent

The effect of solvent on MLCT absorption, emission, and excited-state dynamics has been discussed in a critical review [122]. As noted in the “Localized or delocalized?” section, excitation of $[\text{Ru}(\text{bpy})_3]^{2+}$ and the change from D_3 symmetry in the ground state to C_2 symmetry in the excited state, $[\text{Ru}(\text{bpy})_3]^{2+} \xrightarrow{h\nu} [\text{Ru}(\text{bpy}^*)(\text{bpy})_2]^{2+*}$, creates an excited-state dipole with a significant change in charge distribution in the local environment. The solvent responds through a combination of rotations

of individual solvent molecules (inertial polarization) and collective solvent reorientations (longitudinal polarization).

The quantum spacings for the solvent modes are small for common organic solvents (<50 cm⁻¹), and the solvent contribution can be treated classically at or near room temperature [123,124]. Theoretical treatments of the solvent typically treat the medium as a dielectric continuum characterized by static, D_s , and optical dielectric constants, D_{op} . D_s is measured from the change in capacitance in the presence and absence of the dielectric, and D_{op} is the square of the refractive index, $D_{op} = n^2$.

Absorption

The influence of solvent on MLCT absorption was discussed in the “Localized or delocalized?” section in the context of “localization or delocalization” in [Ru(bpy)₃]^{2+*}. From dielectric continuum theory, with application of the dipole-in-a-sphere model in Fig. 6, the difference in absorption energy between solvents, ΔE_{abs} , is given by eq. 6. In this equation, $\vec{\mu}_g$ and $\vec{\mu}_e$ are the point dipole vectors of the ground and excited states, a , is the radius of a spherical cavity enclosing the complex, λ_0 is the solvent reorganization energy difference between excited and ground states, and $\Delta w(D_s)$ is the difference in solvation energies. As noted in the “Localized or delocalized?” section, the [Ru(bpy)₃]²⁺ ground state has D_3 symmetry with $\vec{\mu}_g = 0$, and eq. 6 simplifies to eq. 1.

$$\Delta E_{abs} = \lambda_0 + \Delta w(D_s) = \frac{1}{a^3} \left[2\vec{\mu}_g(\vec{\mu}_g - \vec{\mu}_e) \frac{D_s - 1}{2D_s + 1} - (\vec{\mu}_g - \vec{\mu}_e)^2 \frac{D_{op} - 1}{2D_{op} + 1} \right] \quad (6)$$

Application of dielectric continuum theory breaks down in the presence of specific solvent effects. They can arise, for example, from H-bonding between ammine ligands and the solvent in complexes such as [Ru(NH₃)₅(py)]²⁺ [125] and [Ru(bpy)₂(NH₃)₂]²⁺ [126], and by electron pair donation from the cyano ligands in complexes such as [Ru(bpy)₂(CN)₂] to the solvent [122,127]. Specific effects have been included through explicit first-shell solvent interactions with the ligands and a continuum treatment for the remainder of the solvent [125,128–134].

Emission

For the thermally equilibrated excited state in Fig. 6, emission is the inverse of absorption returning the complex to the D_3 electronic symmetry of the ground state but with the solvent instantaneously in the C_2 symmetry of the excited state. Application of the dipole-in-a-sphere model to changes in emission energy with solvent, ΔE_{em} , gives eq. 7b. Experimentally, emission from [Ru(bpy)₃]^{2+*} is less solvent-dependent than E_{abs} . In a study of 12 solvents, application of eq. 7b gave a marginal correlation with $R^2 = 0.59$ and slope 3340 ($= \vec{\mu}_e^2/a^3$) compared to $R^2 = 0.75$ for absorption. A better correlation was obtained by a combined fit to the dielectric function and donor number (DN) defined by Guttmann. The DN includes electron pair interactions [135].

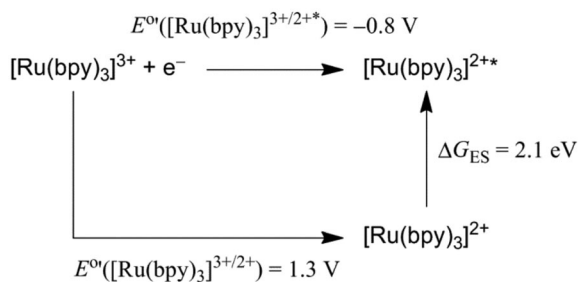
$$E_{em} = \Delta G^0(\text{vac}) - \lambda_i - \lambda_0 + \Delta w(D_s) \quad (7a)$$

$$\Delta E_{em} = \Delta w(D_s) - \lambda_0 = \frac{1}{a^3} \left[2\vec{\mu}_e(\vec{\mu}_g - \vec{\mu}_e) \frac{D_s - 1}{2D_s + 1} + (\vec{\mu}_e - \vec{\mu}_g)^2 \frac{D_{op} - 1}{2D_{op} + 1} \right] \quad (7b)$$

It has been suggested that specific solvent effects arise for emission from [Ru(bpy)₃]^{2+*} due to specific solvent interactions with the partly formed radical anion in the equilibrated excited state, [Ru(bpy^{•-})(bpy)₂]^{2+*} [122]. Dielectric continuum theory works well for absorption in [Ru(bpy)₃]²⁺ because there is no particular orbital basis for specific interactions in the D_3 ground state and the excited state is formed instantaneously in the solvent environment of the ground state.

MLCT EXCITED STATES: REDOX POTENTIALS

Excitation of $[\text{Ru}(\text{bpy})_3]^{2+}$ gives $(d\pi^5\pi^{*1}) [\text{Ru}(\text{bpy})_3]^{2+*}$ with both oxidizing ($d\pi_{\text{Ru}}^5$) and reducing, (π_{bpy}^{*1}), sites in the same molecule. Compared to its ground state, every excited state has enhanced abilities as an oxidant and reductant. A thermodynamic cycle for calculating the reduction potential for $[\text{Ru}(\text{bpy})_3]^{2+*}$ is shown in Scheme 3.



Scheme 3 Thermodynamic cycle for calculating E° for the $[\text{Ru}(\text{bpy})_3]^{3+}/[\text{Ru}(\text{bpy})_3]^{2+*}$ couple.

In redox potential calculations the free energy content of the excited state above the ground state, ΔG_{ES} , is available by analysis of emission spectral profiles as described in the “Emission spectral fitting” section, by using eq. 8. In eq. 8, E_0 is the $\nu = 0 \rightarrow \nu^* = 0$ energy gap, $\Delta\tilde{\nu}_{0,1/2}$ is the vibronic band width at half-height, and $\lambda_{0,L}$ is given by eq. 9. Application of emission spectral fitting to $[\text{Ru}(\text{bpy})_3]^{2+*}$ gives $\Delta G_{\text{ES}} = 2.19$ eV in CH_3CN and 2.19 eV in water, both at room temperature [58].

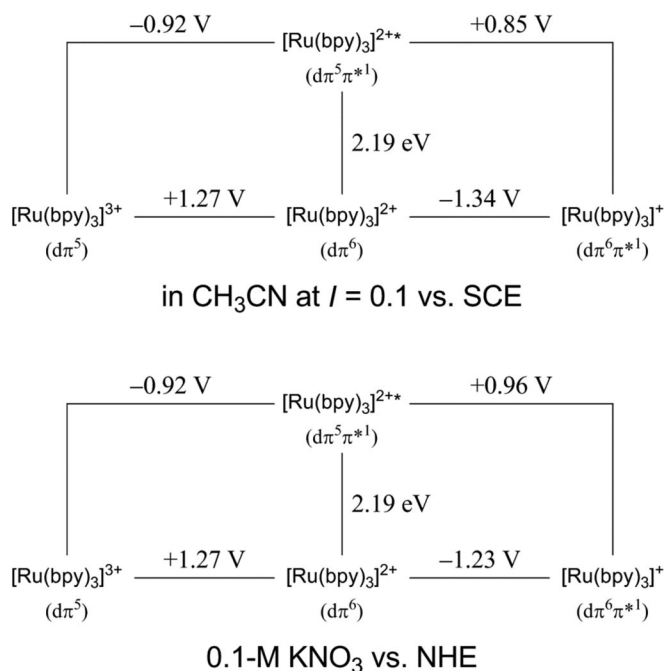
$$\Delta G_{\text{ES}} = E_0 + \lambda_{0,L} = E_0 + \frac{(\Delta\tilde{\nu}_{0,1/2})^2}{16k_{\text{B}}T \ln 2} \quad (8)$$

$$\lambda_{0,L} = \lambda_0 + \lambda_{i,L} \quad (9)$$

E° values for $[\text{Ru}(\text{bpy})_3]^{2+*}$ in both CH_3CN vs. SCE and water vs. NHE ($I = 0.1$) are summarized in the redox potential diagrams in Scheme 4. They are written as reduction potentials and were calculated by using eqs. 10 and 11. Signs are reversed for the half-reactions written as oxidation potentials, e.g., for $[\text{Ru}(\text{bpy})_3]^{2+*} \rightarrow [\text{Ru}(\text{bpy})_3]^{3+} + e^-$, $E^\circ = +0.85$ V. The potentials in Scheme 4 and eqs. 10, 11 are “formal” potentials, the potential of the half-reaction with the oxidized and reduced forms at equal concentrations in the prevailing medium [136].

$$E^\circ([\text{Ru}(\text{bpy})_3]^{2+*/+}) = E^\circ([\text{Ru}(\text{bpy})_3]^{2+/+}) + \Delta G_{\text{ES}}/nF = +0.85 \text{ V} \quad (10)$$

$$E^\circ([\text{Ru}(\text{bpy})_3]^{3+/2+*}) = E^\circ([\text{Ru}(\text{bpy})_3]^{3+/2+}) - \Delta G_{\text{ES}}/nF = -0.92 \text{ V} \quad (11)$$



Scheme 4 Redox potential diagrams and formal potentials, E° , for $[Ru(bpy)_3]^{2+*}$ in CH₃CN at $I = 0.1$ vs. SCE and in water at 0.1 M KNO₃ vs. NHE at room temperature.

ELECTRONIC STRUCTURE: OTHER LOW-LYING EXCITED STATES

MLCT bands dominate the visible spectrum of $[Ru(bpy)_3]^{2+}$ and related polypyridyl complexes but, depending on ligand composition, metal, and molecular structure, a variety of excited states having different electronic origins can appear and play a role.

Upper MLCT excited states

As noted above, light absorption by $[Ru(bpy)_3]^{2+}$ in the UV is dominated by ligand-based $\pi \rightarrow \pi^*$ absorptions. Wavelength-dependent quantum yield measurements show that these states undergo rapid interconversion to the lowest-lying MLCT state(s) but, for $[Ru(bpy)_3]^{2+*}$, with less than unit efficiency [137]. In the visible, absorptivity is dominated by MLCT transitions to $\pi^*_{1,bpy}$ (MLCT(1,1',1'')) and $\pi^*_{2,bpy}$ (MLCT(2)), "Electronic Structure" section. $^3MLCT(1')$ and $^3MLCT(1'')$ are also thermally accessible at room temperature and contribute to excited-state decay, "Excited-State Dynamics" section [138]. Emission at $E_0 = 17230\text{ cm}^{-1}$ from $^3MLCT(2)$ has been reported in KBr disks [139].

In $[Ru(bpy)_2(dppz)]^{2+*}$, competing π^* levels exist in the same dppz acceptor ligand, localized either on the bpy or phenazine fragments (Fig. 11). The bpy-based MLCT state emits while the phenazine-based state is dark. The latter is favored in hydroxylic environments and disfavored in hydrophobic environments, which was exploited by Barton and co-workers in their studies on DNA intercalation [140–143]. The states undergo rapid, $<1\text{ ns}$, interconversion and are at equilibrium on the timescale for ES decay [144,145].

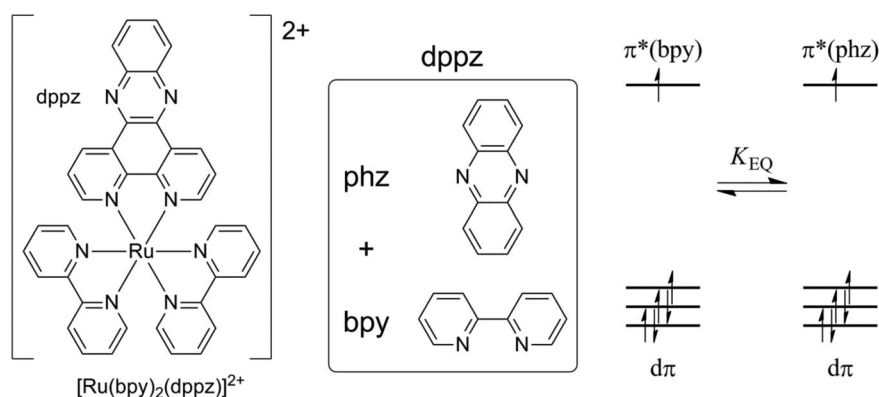


Fig. 11 Structure of $[\text{Ru}(\text{bpy})_2(\text{dppz})]^{2+}$ showing the bpy and phenazine (phz) fragments and the equilibrium between bpy- and phenazine-based MLCT states.

dd (Metal-centered) excited states

For $d\pi^6$ transition-metal complexes additional, low-lying “*dd*” or “metal-centered excited” states of configuration $d\pi^5d\sigma^*1$ or even $d\pi^4d\sigma^*2$ exist in the excited-state manifolds. Optical transitions to these states, $d\pi^6 \xrightarrow{h\nu} d\pi^5d\sigma^*1$, are formally Laporte forbidden ($\Delta l = 0$). Their molar absorptivities, which are in the 100s of $\text{M}^{-1} \text{cm}^{-1}$, are masked by the far more intense MLCT absorptions in the visible. *dd* absorptions do appear in complexes like $[\text{Ru}(\text{NH}_3)_3]^{2+}$, which are free of competitive MLCT transitions [146,147]. They gain intensity by spin-orbit coupling and low-symmetry mixing of the $d\pi/d\sigma^*$ orbitals. They also play a deleterious role in excited-state dynamics by contributing to nonradiative decay and causing ligand-loss photochemistry, “Photochemical ligand loss” section [148–152].

In the MLCT $d\pi^5\pi^*1$ core, interconfigurational transitions, e.g., ${}^3\text{MLCT}(1) \xrightarrow{h\nu} {}^3\text{MLCT}(1')$ $\{{}^3(d\pi_1^2d\pi_2^2d\pi_3^1\pi^*_{1,a}1) \xrightarrow{h\nu} {}^3(d\pi_1^2d\pi_2^1d\pi_3^2\pi^*_{1,a}1)\}$, are predicted to occur, but with low absorptivities in the near-IR [64].

The relative energetics of *dd* ($d\pi^5d\sigma^*1$) and MLCT ($d\pi^5\pi^*1$) excited states vary in a systematic way with molecular properties. Oxidation state, ligands, and structure all affect *dd*/ground-state and MLCT/ground-state “energy gaps” [153]. The splitting between $d\pi$ and $d\sigma^*$, $10Dq$, increases $\sim 30\%$ from Fe to Ru and 30% again from Ru to Os. $10Dq$ also increases with oxidation state in the same coordination environment, e.g., $\text{Rh}^{\text{III}} > \text{Ru}^{\text{II}} > \text{Tc}^{\text{I}}$, and with added π -backbonding ligands such as CO, PR_3 , and CN^- [154].

For $[\text{Fe}(\text{bpy})_3]^{2+}$, intense MLCT absorptions dominate the visible absorption spectrum but *dd* states are lowest-lying, short-lived and dominate excited-state properties [155,156]. For $[\text{Ru}(\text{bpy})_3]^{2+}$, ${}^3\text{MLCT}$ states are lowest-lying but *dd* states are thermally populated at or near room temperature and influence excited-state properties. For example, at room temperature, 37% of $[\text{Ru}(\text{bpy})_3]^{2+}$ decay occurs through *dd* excited states, 80% in CH_2Cl_2 .

Os^{II} is in the third transition series, and *dd* states in $[\text{Os}(\text{bpy})_3]^{2+}$ and related complexes are thermally inaccessible at room temperature except in highly asymmetric ligand environments where there is extensive $d\pi$ - $d\sigma^*$ mixing [82,157]. Because of their photochemical stability, and the absence of complications from *dd* states, Os^{II} polypyridyl complexes have been used extensively in the investigation of excited-state properties, “*dd* Excited states” section.

Ligand-based excited states

In an extended series of complexes based on *fac*- $[\text{Re}(\text{bpy})(\text{CO})_3(\text{L})]^+$ ($\text{L} = \text{CO}, \text{py}, \dots$), stabilization of the $d\pi$ levels by backbonding to CO leads to large MLCT energy gaps. In this electronic environment,

the energies of the lowest MLCT state(s) are comparable to ligand-based $^3(\pi^1\pi^*1)$ states. In [Re(phen)(CO)₃(4-Mepy)]⁺ (4-Mepy = 4-methylpyridine), a 3 MLCT state is lowest-lying as shown by the positive shifts in the $\nu(\text{CO})$ bands in the TRIR spectrum in Fig. 12 [158]. In [Re(dppz)(CO)₃PPh₃]⁺, a $^3(\pi^1\pi^*1)$, dppz-based excited state is lowest-lying (note the structure of dppz in Fig. 11) and the shifts in $\nu(\text{CO})$ are small, $\sim 8 \text{ cm}^{-1}$, and to lower energy.

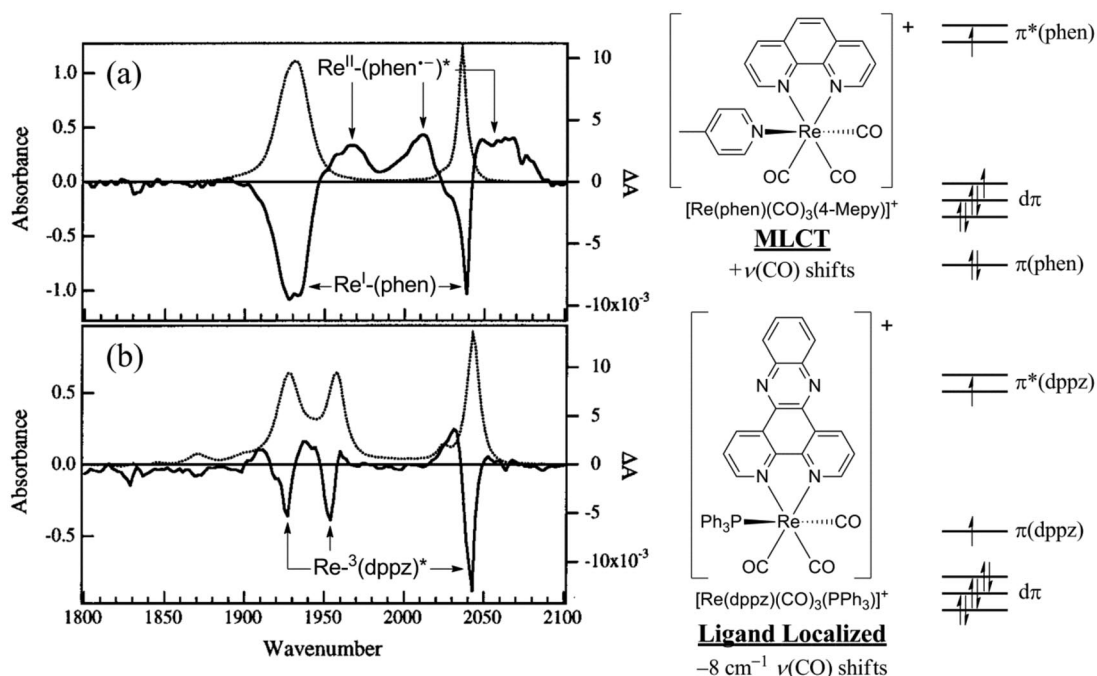


Fig. 12 Ground-state (dotted trace) and TRIR difference spectra (solid trace) obtained 600 ns after laser flash excitation of [Re(phen)(CO)₃(4-Mepy)]⁺ (a) and [Re(dppz)(CO)₃PPh₃]⁺ (b) both in CD₃CN at room temperature. An orbital diagram is also shown. Spectra adapted from ref. [158].

Other excited states

In complexes with oxidizable ligands such as [Re(bpy)(CO)₃R] (R = Et, *i*Pr, CH₂Ph), the lowest-lying excited state is $\sigma\text{-}\pi^*$ with the electronic configuration, $d\pi_{\text{Re}}^6\sigma_{\text{Re-C}}^1\pi_{\text{bpy}}^*1$. For [Re(bpy)(CO)₃I], the lowest excited state is best described as a ReI(CO)₃ \rightarrow bpy CT state with extensive $d\pi_{\text{Re}}\text{-}p\pi_{\text{I}}$ mixing [6,7]. The visible–near-UV spectra of these complexes are dominated by MLCT bands in the high energy visible with MLCT excitation for the iodo complex sensitizing the mixed CT excited state. The latter can emit and has an appreciable lifetime [7,29]. MLCT excitation of alkyl complexes of the type [Re(bpy)(CO)₃-R] leads to Re–R bond cleavage, [Re(bpy)(CO)₃-R] $\xrightarrow{h\nu}$ [Re(bpy)(CO)₃][•] + R[•] [29]. Metal–metal bond cleavage occurs following MLCT excitation of the analogous dimer, [(bpy)(CO)₃Re–Re(CO)₃(bpy)], by internal sensitization of a dissociative $\sigma\sigma^*(\text{Re–Re})$ excited state [159].

EXCITED-STATE DYNAMICS

At room temperature in water, [Ru(bpy)₃]^{2+*} emits at $\lambda_{\text{max}} = 625 \text{ nm}$ with an efficiency of 0.063 [160,161] and lifetime of 580 ns [162,163]. Excitation of [Ru(bpy)₃]²⁺ throughout the visible and near-

UV gives $[\text{Ru}(\text{bpy})_3]^{2+*}$ with near unit efficiency but with complex early time behavior and roles for low-lying $^3\text{MLCT}$ and dd states.

What happens after excitation?

Early time events following initial $\text{GS} \xrightarrow{h\nu} ^1\text{MLCT}(1)$ excitation, as probed by ultrafast spectroscopy, are summarized in Fig. 13. A fluorescence from $^1\text{MLCT}(2)$ in water was observed at 500 nm by Chergui et al., following 400 nm excitation. It is short-lived, converting to triplet $^3\text{MLCT}(1)$ with $\tau \sim 15$ fs [164]. The energy gap between $^1\text{MLCT}(1)$ and $^3\text{MLCT}(1)$, the singlet–triplet splitting is $\sim 1700 \text{ cm}^{-1}$ with $E(\text{S}) - E(\text{T}) = 2K$ and $K = 850 \text{ cm}^{-1}$ [60]. K is the spin exchange integral, defined in eq. 12 where \hat{H}_{SO} is the spin-orbit coupling operator and the Ψ are unmixed spin wave functions for $^3\text{MLCT}(1)$ and a low-lying singlet excited state or states.

$$K = \langle ^1\Psi_{\text{ES}} | \hat{H}_{\text{SO}} | ^3\Psi_{\text{ES}} \rangle \quad (12)$$

Based on a Franck–Condon analysis of the $\text{GS} \xrightarrow{h\nu} ^1\text{MLCT}(1)$ absorption in the visible with application of the single-mode approximation, $E_0 = 21\,900 \text{ cm}^{-1}$ and $\langle \hbar\omega \rangle = 1600 \text{ cm}^{-1}$ in the initially formed singlet state [164]. As noted above, $^3\text{MLCT}(1)$ appears from the singlet in 15 fs, initially to give the vibrationally excited triplet, $(^3\text{MLCT}(1))^*$, at 3.1 eV (25 000 cm^{-1}). The triplet relaxes to thermally equilibrated $[\text{Ru}(\text{bpy})_3]^{2+*}$ at 2.1 eV with $\tau = 20$ ps.

As shown by time-dependent resonance Raman measurements by McGarvey and co-workers [165] and earlier by Mathies and co-workers [166], vibrational relaxation within the hot triplet is accompanied by a time-dependent change in population and distribution in 7 coupled $\nu(\text{bpy})$ modes with the average $\nu(\text{bpy})$ quantum spacing decreasing from $\langle \hbar\omega \rangle \sim 1600$ to 1300 cm^{-1} in the equilibrated excited state with $\langle \hbar\omega \rangle = \sum_j S_j \hbar\omega_j / \sum_j S_j$ from eq. 4c [165].

Based on these observations, the 1.0 eV of excess energy in the $^1\text{MLCT}(1) \rightarrow ^3\text{MLCT}(1)$ transition, initially as electronic energy in $^1\text{MLCT}(1)$, ends up largely in excited $\nu(\text{bpy})$ modes in $(^3\text{MLCT}(1))^*$. Subsequent vibrational relaxation occurs through internal energy redistribution to low-frequency modes and then to the solvent [167,168]. Based on ultrafast spectroscopic measurements fol-

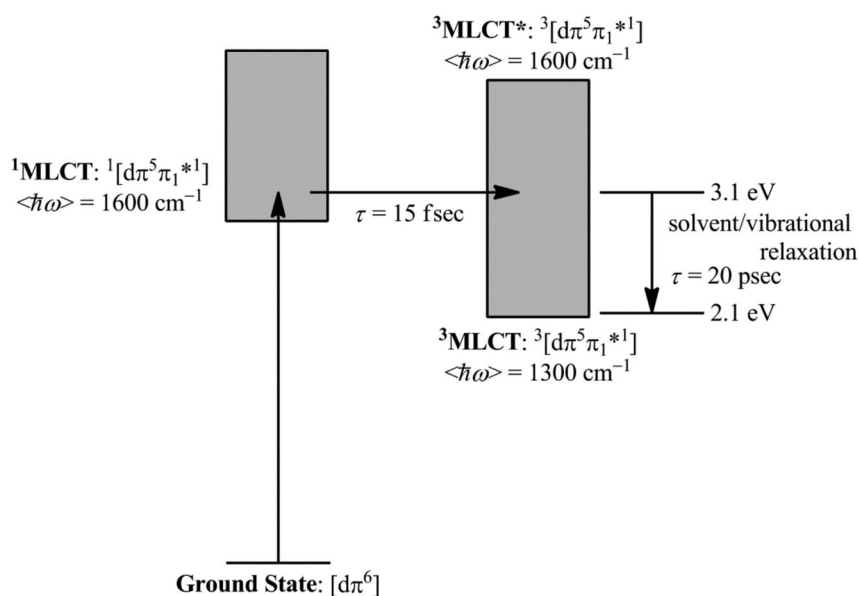


Fig. 13 Light absorption and equilibration following MLCT excitation of $[\text{Ru}(\text{bpy})_3]^{2+}$ in H_2O at 400 nm.

lowing charge-transfer excitation of organic dyes [169], typical solvent relaxation times are 0.5 ps for CH₃CN, 5 and 6 ps for methanol, and 13 and 27 ps for ethyleneglycol.

Excited-state dynamics: Dipole reorientation and ILET

A dynamic role for the degenerate ³MLCT(1) states, “Electronic Structure” section, appears in excited-state polarization measurements on [Ru(bpy)₃]^{2+*}. Polarized excitation selectively excites molecules lying in the plane of the incident polarized radiation, and Kelly et al. observed dynamic polarization anisotropy changes following MLCT excitation [170]. The initial polarization was retained at their earliest observation times consistent with C₂ symmetry and localization in the initial excited state. Subsequent time-dependent polarization de-phasing occurred and was fit to two components with τ₁ = 5 ps and τ₂ = 125 ps in water. The rapid component was attributed to “exciton hopping” and the slow to rotational diffusion of the molecule [69,170].

An energy-coordinate curve illustrating the barrier crossing between two of the three substates in ³MLCT(1) is shown in Fig. 14. The figure also illustrates energy-coordinate curves for ³MLCT(1') and ³MLCT(1''). ³MLCT(1') is also the ligand-to-ligand charge transfer state (³LLCT). The inter-MLCT transitions proposed as the origin of the near-IR absorption band for [Os(phen)₃]^{2+*} in Fig. 4 are also illustrated in Fig. 14. Thermally activated barrier crossings among the three substates of ³MLCT(1) with rotation of the excited-state dipole can account for the observed transient polarization changes. Thermally activated interligand electron transfer (ILET)—³MLCT(1) → ³LLCT{³MLCT(1')} → ³MLCT(1)—also leads to depolarization but with an increase in the activation barrier.

McCusker et al. extended the time-resolved polarization measurements to shorter times by using 25-fs pulsed, magic angle excitation at 475 nm in nitrile solvents [79,171,172]. The magic angle is the angle between the excitation and probe pulses and, in the transient experiment, allows changes arising from dipole rotation to be observed without complications from molecular rotation. The time-depend-

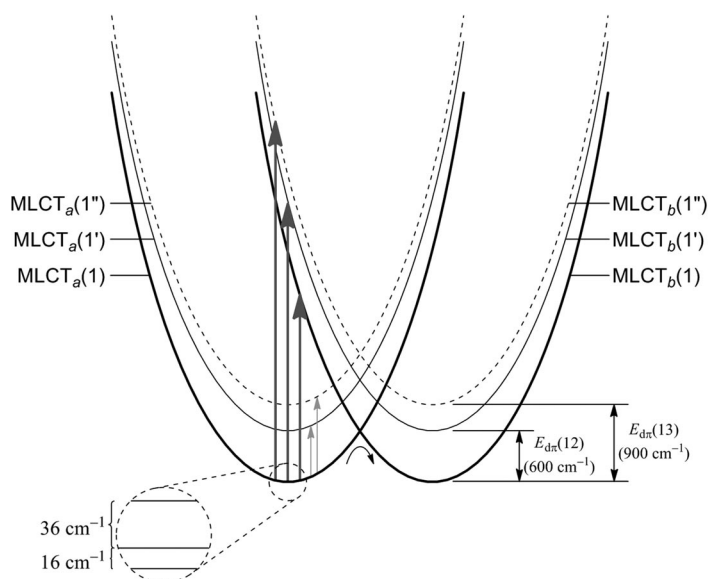


Fig. 14 Energy-coordinate curves illustrating thermal barrier crossing between two of the three substates of ³MLCT(1) in [Os(phen)₃]^{2+*} in CD₃CN, which leads to dipole–dipole reorientation and depolarization. Also shown are optical transitions interconverting ³MLCT(1), ³MLCT(1'){³LLCT(1)}, and ³MLCT(1''), Fig. 4. ³MLCT(1') is also the ligand–ligand charge–transfer state, ³LLCT(1). The transition, ³MLCT(1) $\xrightarrow{h\nu}$ ³LLCT(1), dominates the intensity of the near IR band shown in Fig. 4.

ent changes were interpreted at the earliest times as arising from a two-fold degenerate transition dipole. A relaxation time of ~60 fs was observed, near the inertial relaxation time for CH₃CN, with continued dynamics to 300 fs. Based on these results, McCusker et al. concluded that inertial solvent dynamics likely play a key role in a process of charge localization in initially delocalized [Ru^{III}(bpy^{1/3-})₃]^{2+*}. It should be noted that on the timescale of McCusker's experiment, intersystem crossing had already occurred ("What happens after excitation" section) to give (³MLCT(1))^{*}. Rapid de-phasing may occur in the unrelaxed excited state by dipole–dipole rotation.

A number of related observations have been made. Papanikolas et al. observed wavelength-dependent depolarization dynamics following ultrafast excitation of [Os(bpy)₃]²⁺ in CH₃CN [173,174]. Hammarström et al. conducted transient pump–probe anisotropy measurements on [Ru(bpy)₃]²⁺ and [Ru(bpy)(py)₄]²⁺ in CH₃CN with femtosecond time resolution following 480-nm excitation [69]. Monitoring at 340 and 650 nm revealed no correlation between excited-state polarization and the initial bpy ligand photoselected even after a few hundred femtoseconds [69]. This observation points to rapid depolarization before relaxation and dynamics more complex than the hopping and decoherence models proposed by McCusker et al.

In time-resolved depolarization measurements on [Os(bpy)₃]²⁺, the appearance of an excitation dependence in the transient dynamics led Papanikolas and co-workers to conclude that depolarization by dipole–dipole reorientation is more rapid in the initial singlet and vibrationally hot ³MLCT(1) states than in the equilibrated triplet. Depolarization was found to be more rapid by ~5 in [Os(bpy)₃]^{2+*} compared to [Ru(bpy)₃]^{2+*}.

The final tale on interconversion among the low-lying MLCT states remains to be told, but depolarization by dipole reorientation is consistent with most of the available data. An accounting still remains for possible laser pulse excitation effects and the origin of rapid depolarization following excitation to give ¹MLCT(1).

Excited-state decay

The synthetic chemistry for Os(II) polypyridyl complexes has yielded 20–30 complexes of the type [Os(bpy)(L)₄]²⁺ and [Os(phen)(L)₄]²⁺. Variations in the non-chromophoric ligands, L—from strongly π backbonding CO, PR₃, ... to strongly electron donating H⁻, R⁻, ...—provide a basis for systematically varying key excited- and ground-state properties—energy gaps, redox potentials, Stability in both ground and excited states and relatively uncluttered excited-state manifolds have Os^{II} polypyridyl complexes the molecules of choice for many studies. The synthetic chemistry of analogous Ru^{II} complexes is even further advanced, but the intervention of low-lying *dd* excited states introduces complications by introducing a temperature dependence and ligand-loss photochemistry, "*dd* Excited states" and "Photochemical ligand loss" sections, respectively.

Radiative and nonradiative decay rate constants, k_r and k_{nr} , are obtainable by a combination of emission quantum yield (η_{em}) and lifetime (τ) measurements, eqs. 13. With the implicit assumption that the emissive state is populated with unit efficiency, which may or may not be true. Polypyridyl complexes of Ru^{II} and Os^{II} are typically weak emitters with nonradiative decay dominating and $k_{nr} \gg k_r$.

$$\tau = (k_r + k_{nr})^{-1} \quad (13a)$$

$$\eta_{em} = k_r / (k_r + k_{nr}) \quad (13b)$$

Radiative decay

As shown in eqs. 14, k_r is predicted to increase with the square of the transition dipole moment, $\bar{\mu}$, and decrease with the inverse cube of the energy gap between ground and excited states, $\langle \bar{\nu}^{-3} \rangle \sim E_{em}^{-3}$. The magnitude of the transition dipole depends on the extent of spin-orbit coupling induced mixing of excited singlet states (¹Ψ_{ES}) into the lowest "triplet" (³Ψ_{ES}), eq. 15. The mixing coefficient, α , and the

extent of singlet character in the triplet, eq. 16, increase with the spin-orbit coupling constant with $\zeta_{\text{Ru}} = 1100 \text{ cm}^{-1}$ and $\zeta_{\text{Os}} = 3000 \text{ cm}^{-1}$.

$$k_{\text{r}} \propto |\bar{\mu}|^2 E_{\text{em}}^3 \quad (14a)$$

$$E_{\text{em}}^3 \sim \langle \bar{\nu}^{-3} \rangle^{-1} \quad (14b)$$

$$\bar{\mu} = \left\langle \left({}^3\Psi_{\text{ES}} + \alpha {}^1\Psi_{\text{ES}} \right) \left| e \sum_n \vec{r}_n \right| {}^1\Psi_{\text{GS}} \right\rangle = \alpha \left\langle {}^1\Psi_{\text{ES}} \left| e \sum_n \vec{r}_n \right| {}^1\Psi_{\text{GS}} \right\rangle \quad (15)$$

$$\alpha = \left\langle {}^1\Psi_{\text{ES}} \left| \hat{H}_{\text{SO}} \right| {}^3\Psi_{\text{ES}} \right\rangle / (E_{\text{S}} - E_{\text{T}}) \quad (16a)$$

$$\left\langle {}^1\Psi_{\text{ES}} \left| e \sum_n \vec{r}_n \right| {}^3\Psi_{\text{GS}} \right\rangle = 0 \quad (16b)$$

Attempted correlations between k_{r} and E_{em}^3 according to eq. 14a typically result in scatter and weak correlations at best [107]. This is due, in part, to variations in dπ orbital composition as structures change and to the inherent errors in measuring quantum yields of a few percent.

Nonradiative decay

Nonradiative decay occurs with energy conservation with the initial electronic energy of the excited state appearing in excited vibrational levels in the ground state and in the solvent. To zero order, excited and ground states cannot mix because they are orthonormal solutions of the same Hamiltonian. The transition between states is induced by “promoting modes”, typically low-frequency modes that mix the initial and final electronic wave functions. Activation of these modes induces the transition between states which is a breakdown of the Born–Oppenheimer approximation. For MLCT excited states like [Ru(bpy)₃]^{2+*} the promoting modes are low-frequency (300–400 cm⁻¹) M–N skeletal vibrations which, when excited, enhance electronic wave function overlap.

Based on time-dependent perturbation theory, with application of Fermi’s Golden Rule, the rate constant for nonradiative decay is given by eq. 17. V_{k} is the vibrationally induced electronic coupling matrix element. It is defined in eq. 18 with $\psi_{\text{el},f}$ and $\psi_{\text{el},i}$ the final and initial electronic wave functions, $\chi_{V_{\text{k},f}}$ and $\chi_{V_{\text{k},i}}$ the final and initial vibrational wave functions for promoting mode k with quantum spacing $\hbar\omega_{\text{k}}$ and normal coordinate Q_{k} . FC is the Franck–Condon density of states or “Franck–Condon factor”. It provides a quantitative accounting of the changes in molecular and solvent structure between initial and final states.

$$k_{\text{nr}} = \frac{2\pi}{\hbar} |V_{\text{k}}|^2 (\text{FC}) \quad (17)$$

$$V_{\text{k}} = \frac{\hbar^2}{M_{\text{k}}} \left\langle \psi_{\text{el},f} \left| \frac{\partial}{\partial Q_{\text{k}}} \right| \psi_{\text{el},i} \right\rangle \left\langle \chi_{V_{\text{k},f}} \left| \frac{\partial}{\partial Q_{\text{k}}} \right| \chi_{V_{\text{k},i}} \right\rangle = \frac{\hbar}{M_{\text{k}}^{1/2}} \left\langle \psi_{\text{el},f} \left| \frac{\partial}{\partial Q_{\text{k}}} \right| \psi_{\text{el},i} \right\rangle \left(\frac{\hbar\omega_{\text{k}}}{2} \right)^{1/2} = C_{\text{k}} \left(\frac{\hbar\omega_{\text{k}}}{2} \right)^{1/2} \quad (18)$$

For [Ru(bpy)₃]^{2+*}, ³MLCT → ¹GS nonradiative decay is nominally spin forbidden with the spin prohibition lifted by spin-orbit coupling, eqs. 19. The mixing coefficient, α , was defined in eq. 16.

$$\frac{\hbar}{M_{\text{k}}^{1/2}} \left\langle \psi_{\text{el},f} \left| \frac{\partial}{\partial Q_{\text{k}}} \right| \psi_{\text{el},i} \right\rangle \left(\frac{\hbar\omega_{\text{k}}}{2} \right)^{1/2} = \left\langle \psi_{\text{el},f} \left| \frac{\partial}{\partial Q_{\text{k}}} \right| \psi_{\text{el},i} \right\rangle = \alpha \left\langle {}^1\Psi_{\text{el},f} \left| \frac{\partial}{\partial Q_{\text{k}}} \right| {}^1\Psi_{\text{el},i} \right\rangle \quad (19a)$$

$$C_k = \frac{\alpha \hbar}{M_k^{1/2}} \left\langle \psi_{el,f} \left| \frac{\partial}{\partial Q_k} \right| \psi_{el,i} \right\rangle \quad (19b)$$

In the limit of applicability of the energy gap law— $\hbar\omega \gg k_B T$ and $|\Delta E|/S\hbar\omega \gg 1$ —for a single high- or medium-frequency coupled mode, k_{nr} , is given by eqs. 20 [175,176].

$$k_{nr} \approx \frac{\sqrt{\pi}\omega_k C_k^2}{(2\hbar\omega|\Delta E|)^{1/2}} \exp(-S) \exp\left(-\frac{\gamma|\Delta E|}{\hbar\omega}\right) \exp(S_0 + Z_1 + Z_2) \quad (20a)$$

$$Z_1 = S_0 \left(\frac{\langle \omega_o \rangle}{\omega} \right) (\gamma + 1) \quad (20b)$$

$$Z_2 = S_0 \left[\left(\frac{\langle \omega_o \rangle}{\omega} \right) (\gamma + 1) \right]^2 \left[\exp\left(\frac{\hbar\omega_o}{k_B T}\right) - 1 \right]^{-1} \quad (20c)$$

$$\gamma = \ln\left(\frac{|\Delta E|}{S\hbar\omega}\right) - 1 \quad (20d)$$

In eqs. 20, ΔE is the internal energy change in the transition and, as defined in eqs. 4–5, ω ($= 2\pi\nu$) is the angular frequency of the average acceptor mode in the ground state. S ($= (1/2)\Delta Q_e^2$) is the electron-vibrational coupling constant or Huang–Rhys factor. $\langle \omega_o \rangle$ is the mean frequency for the solvent and coupled low-frequency modes treated classically.

In the single-mode approximation, k_{nr} is given by eqs. 21 with all of the parameters except C_k available by emission spectral fitting. The energy gap, E_0 , is related to the experimentally observed emission energy (E_{em}) by $|\Delta E| = E_0 + \lambda_{o,L} \approx E_{em} + \lambda_{o,L}$.

$$k_{nr} = \frac{\sqrt{\pi}\omega_k C_k^2}{(2\hbar\omega E_0)^{1/2}} \exp\left[-S - \frac{\gamma E_{em}}{\hbar\omega} + \left(\frac{\gamma + 1}{\hbar\omega}\right)^2 \lambda_{o,L} k_B T\right] \quad (21a)$$

$$\gamma = \ln\left(\frac{E_0}{S\hbar\omega}\right) - 1 \quad (21b)$$

$$\frac{(\Delta \tilde{V}_{0,1/2})^2}{16 \ln 2} = \lambda_{o,L} k_B T \quad (21c)$$

$$\lambda_{o,L} = S_0 \hbar \langle \omega_o \rangle \quad (22)$$

In logarithmic form, k_{nr} is given by eq. 23 and, in the single-mode approximation, by eq. 24.

$$\ln k_{nr} = \ln \beta_0 + \ln[\text{FC}(\text{calc})] \quad (23)$$

$$\ln k_{nr} = \ln \beta_0 - S - \frac{\gamma E_0}{\hbar\omega} + \left(\frac{\gamma + 1}{\hbar\omega}\right)^2 \lambda_{o,L} k_B T \quad (24)$$

β_0 and $\ln[\text{FC}(\text{calc})]$ are given in eqs. 25 and 26.

$$\beta_0 = \left(\frac{\pi}{2}\right)^{1/2} \omega_k C_k^2 - \frac{\sqrt{2\pi} V_k^2}{\hbar} \quad (25)$$

$$\ln[\text{FC}(\text{calc})] = -\frac{1}{2}\ln(\hbar\omega E_0) - S - \frac{\gamma E_{\text{cm}}}{\hbar\omega} + \left(\frac{\gamma+1}{\hbar\omega}\right)^2 \lambda_{\text{o,L}} k_{\text{B}}T \quad (26)$$

In this form, eq. 24 is the famous “energy gap law” for nonradiative decay. It relates nonradiative decay dynamics to the energy gap between excited and ground states [107,177–181]. In the absence of competing photochemical reactions, it is also a good predictor of excited-state lifetimes at or near room temperature where decay of MLCT excited states is dominated by nonradiative decay.

In excited-state decay, the key is not thermal activation and barrier crossing, as in a normal chemical reaction. The key is *energy disposal* either by emission or conversion into excited vibrational and solvent levels in the ground state.

The energy gap law has been successfully tested for nonradiative decay in a variety of excited states [175,176,182–184] including MLCT excited states of Ru^{II} [101,103,105,185–187], Os^{II} [102,107,177,178,180,181], and Re^I [108,179,188]. In studies based on MLCT excited states, the energy gap was varied by varying solvent [178,186], ion-pairing [180], and the fluid-to-glass transitions [102].

The most comprehensive test of the energy gap law has come from photophysical measurements on 32 polypyridyl Os^{II} complexes varying from [Os(phen)(py)₄]²⁺ to [Os(bpy)₂(DMSO)₂]²⁺ with energy gaps ranging from 13 100 to 19 800 cm⁻¹ (764 to 505 nm) in CH₃CN [107]. In the series, ln[FC(calc)] was evaluated by application of the single-mode Franck–Condon analysis of emission spectral profiles to give S_M, E₀, ħω_M, and λ_{o,L}.

Figure 15 shows a plot of ln k_{nr} vs. ln[FC(calc)] according to eq. 23. Although there is scatter in the data, the predicted linear relationship between ln k_{nr} and ln[FC(calc)] is observed over the extended range of energy gaps from 13 100 to 19 800 cm⁻¹. Based on eq. 23, the slope of the plot of ln k_{nr} vs. ln[FC(calc)] in Fig. 15 is 1. With an assumed quantum spacing of 300 cm⁻¹ for the promoting mode, a value of V_k ~ 1300 cm⁻¹ was calculated for the vibrationally induced electronic coupling matrix element.

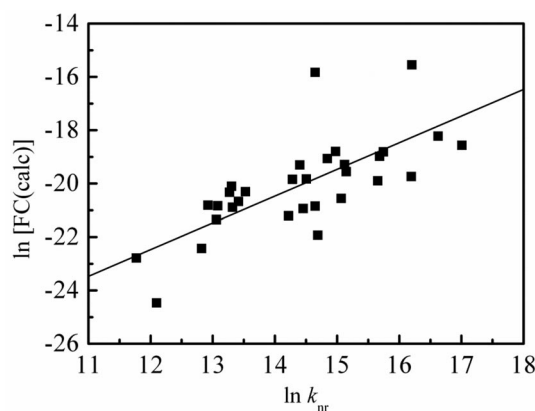
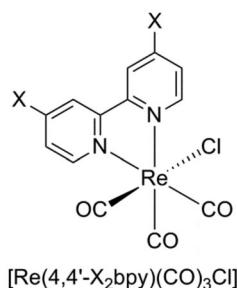


Fig. 15 Plot of ln k_{nr} vs. ln[FC(calc)] for a series of polypyridyl Os^{II} complexes in CH₃CN. Data obtained from ref. [107]. Solid line is a fit of the data to eq. 23.

The origin of the linear decrease in ln k_{nr} with E₀ comes from the influence of the energy gap on vibrational overlaps in the ν(bpy) acceptor modes between initial and final states. In the quantum limit, these overlaps dictate rates and their magnitudes reflect the degree to which the initial and final states co-exist along the same normal coordinate. At or near room temperature, low-frequency modes behave classically. The solvent helps dictate the magnitude of the energy gap, the use of the near continuum of solvent modes ensures energy conservation for transitions by individual molecules.

In a study related to the Os^{II} polypyridyl complexes, a linear relationship was found between $\ln k_{\text{nr}}$ and $\ln[\text{FC}(\text{calc})]$ for a series of nine complexes of the type $[\text{Re}(4,4'\text{-X}_2\text{bpy})(\text{CO})_3\text{Cl}]$ in 2-methyltetrahydrofuran. In this series, the substituent X was varied from electron-withdrawing, $-\text{COOEt}$, to electron-donating, $-\text{NEt}_2$. E_0 increased from 14 300 to 18 040 cm^{-1} and k_{nr} decreased from 1.1×10^8 to $2.4 \times 10^6 \text{ s}^{-1}$. From the slope of a plot of $\ln k_{\text{nr}}$ vs. $\ln[\text{FC}(\text{calc})]$, $V_k = 600 \text{ cm}^{-1}$ assuming $\hbar\omega_k = 300 \text{ cm}^{-1}$ [108].



As mentioned in the “MLCT Excited States: Molecular Structure” section, other systematic relationships have emerged from the energy gap studies. One was a linear increase in S ($=\Delta Q_e^2/2$) as the energy gap was increased [107,108]. This result is consistent with increasing charge-transfer character as the energy gap increases.

As noted in the “Resonance Raman” section, a more detailed, mode-by-mode analysis is possible based on application of the Heller analysis to ground-state resonance Raman excitation profiles. This analysis gives both $\hbar\omega_j$ and S_j on a mode-by-mode basis. When applied to nonradiative decay in $[\text{Os}(\text{bpy})_3]^{2+*}$, $[\text{Os}(\text{bpy})_2(\text{py})_2]^{2+*}$, and $[\text{Os}(\text{bpy})(\text{py})_4]^{2+*}$, the “Resonance Raman” section, the major contributors to nonradiative decay as energy acceptors were $\nu(\text{bpy})$ modes at 1575 and 1485 cm^{-1} with S values of 0.22 [113]. This study also substantiated the validity of the average mode approximation and use of emission spectral fitting to obtain the key parameters needed for a quantitative description of non-radiative decay.

Nonradiative decay from upper MLCT states

Based on the analysis in the “Electronic Structure” section, the states $^3\text{MLCT}(1')$ and $^3\text{MLCT}(1'')$ in $[\text{Os}(\text{phen})_3]^{2+*}$ lie ~ 600 and 900 cm^{-1} higher in energy than $^3\text{MLCT}(1)$. Evidence for participation by one or both appears in excited-state dynamics and temperature-dependent lifetimes. From the temperature dependence of k_{nr} , eq. 27, $k_1 \sim 10^8 \text{ s}^{-1}$ and $\Delta E_1 \sim 600 \text{ cm}^{-1}$ in 4/1 (v/v) ethanol/methanol.

$$\frac{1}{\tau} = \frac{k_0 + k_1 \exp(-\Delta E_1/k_{\text{B}}T)}{1 + \exp(-\Delta E_1/k_{\text{B}}T)} \quad (27)$$

dd Excited states

For $[\text{Ru}(\text{bpy})_3]^{2+*}$ and related complexes of Ru^{II}, *dd* states are sufficiently low-lying to be thermally accessible from $^3\text{MLCT}(1)$. This creates an additional temperature-dependent, nonradiative channel for $[\text{Ru}(\text{bpy})_3]^{2+*}$ decay, eq. 28. For $[\text{Ru}(\text{bpy})_3]^{2+*}$, k_2 and ΔE_2 in eq. 28 are medium-dependent with, $k_2 \sim 1 \times 10^{13} \text{ s}^{-1}$ and $\Delta E_2 \sim 3000\text{--}4000 \text{ cm}^{-1}$. As noted in the “*dd* (Metal-centered) excited states” section, at room temperature in dimethyl formamide (DMF), 37 % of excited-state decay occurs through this channel and 80 % in CH_2Cl_2 . Energy-coordinate curves illustrating thermal activation and *dd* excited-state decay are shown in Fig. 16.

$$\frac{1}{\tau} = k_0 + k_1 \exp(-\Delta E_1/k_B T) + k_2 \exp(-\Delta E_2/k_B T) \quad (28)$$

The quantity ΔE_2 in eq. 28 is the free energy of activation, ΔG^* , for internal conversion between ³MLCT(1) and a *dd* excited state or states, eq. 29. In eq. 29, ΔG_{dd} is the free energy difference between ³MLCT(1) and *dd* and λ_{dd} is the classical reorganization energy for barrier crossing. As in any non-radiative conversion between internal electronic states, the transition is induced by a “promoting mode” that mixes the electronic states.

$$\Delta E_2 = \Delta G^* = \frac{(\Delta G_{dd} + \lambda_{dd})^2}{4\lambda_{dd}} \quad (29)$$

Although not much is known about these quantities, it is possible to surmise important details. A significant reorganization energy is anticipated given the significant increase in *r*(Ru–N) bond lengths in the *dd*(*dπ*⁵*dσ*^{*1}) excited state because of electron occupation of *dσ*^{*}. A solvent reorganization energy is also expected given the loss of excited-state dipole in the *dd* state [187].

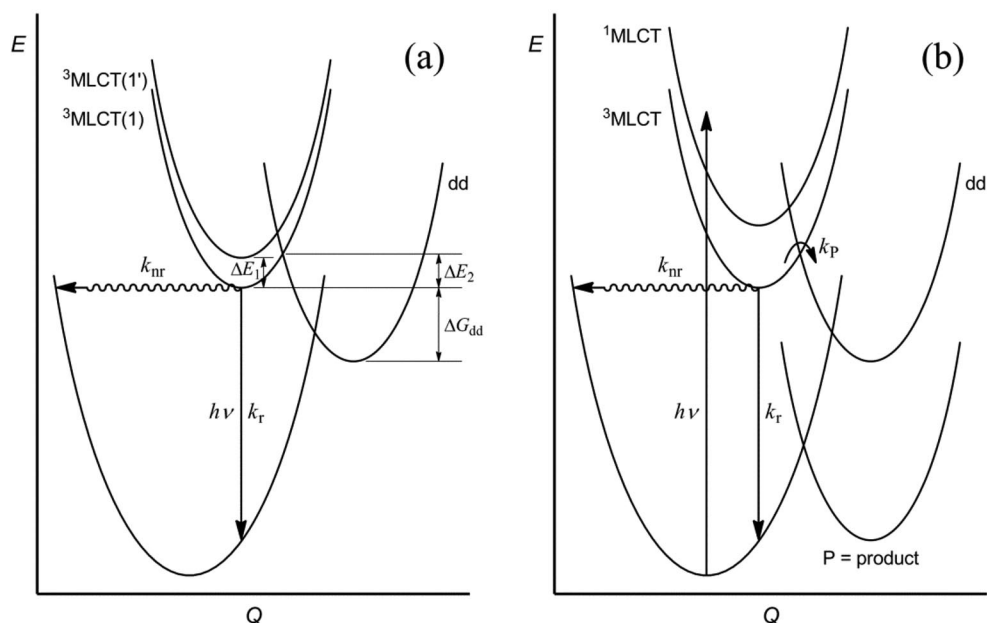


Fig. 16 Energy-coordinate curves illustrating thermal activation and decay from low-lying MLCT and *dd* states in [Ru(bpy)₃]^{2+*} (a) and photochemical ligand loss by MLCT → *dd* barrier crossing and metal–ligand bond breaking (b).

EXCITED-STATE REACTIONS

The real interest in excited states is reactivity and the influence of light on both electronic structure and reactivity. Utilization is a balancing act given the competition between reactivity and excited-state decay.

Photochemical ligand loss

Occupation of *dd* states contributes to nonradiative decay and can lead to metal–ligand bond cleavage and photodecomposition. An energy coordinate–reaction diagram is shown in Fig. 16b illustrating the sequence: (1) MLCT excitation, (2) thermal activation and MLCT → *dd* surface crossing, and (3) ligand loss photochemistry. The mechanism for substitutional ligand loss appears to be dissociative with evidence for transient lower coordinate intermediates by ultrafast spectroscopic measurements, the “*dd* (Metal-centered) excited states section” [189].

The quantum yield for py loss in *cis*-[Ru(bpy)₂(py)₂]²⁺ at room temperature in CH₂Cl₂ is 18 (±2) %. [Ru(bpy)₃]^{2+*} is also photolabile with the NCS[−] salt in CH₂Cl₂ undergoing NCS[−] substitution and chelate ring opening with $\Phi_{\text{NCS}^-} = 0.07$ in CH₂Cl₂ at 25 °C, eqs. 30. In coordinating solvents—H₂O, CH₃CN, ...—bpy ligand loss is inefficient, not necessarily due to inhibition toward ligand loss, but due to efficient chelate re-closure— $\xrightarrow{h\nu}$ [Ru(bpy)₃]^{2+*} → [(bpy)₂Ru(py-py)]²⁺ → [Ru(bpy)₃]²⁺ [148,149]. A relatively long-lived transient has been identified following flash photolysis of [Ru(bpy)₃]^{2+*} with the py-py intermediate proposed to be a π -bonded adduct, or three-centered agnostic intermediate. Ring closure occurs with $k = 1.3 \times 10^4 \text{ s}^{-1}$ with unit efficiency [190].



Stabilization toward ligand loss has been demonstrated in rigid media—glasses, films, sol-gels, ... [187,191–196]. Stabilization appears to arise from a restriction of large amplitude M–L motions required to break the M–L bond and retention of the ejected ligand near the open coordination site where it is available for re-coordination. In films of polymethylmethacrylate (PMMA), the *dd* state of *cis*-[Ru(bpy)₂(py)₂]²⁺ continues to contribute to nonradiative decay even though ligand-loss photochemistry is inhibited [187].

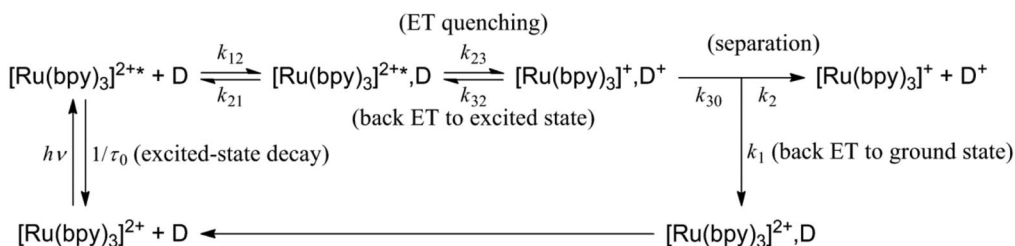
Interference by *dd* states can be ameliorated by ligand tuning. Strong σ -donor ligands decrease 10Dq decreasing the MLCT–*dd* barrier. Low-lying π^* MLCT acceptor ligands stabilize the lowest MLCT state increasing the MLCT–*dd* energy gap. In [Ru(bpy)₃]^{2+*}, ΔH^* for MLCT → *dd* thermally activated crossing is 3100–3500 cm^{−1} depending on solvent. In the mixed chelate, [Ru(bpy)₂(bpm)]²⁺ (bpm is 2,2'-bipyrimidine), $\pi^*(\text{bpm})$ is lower than $\pi^*(\text{bpy})$ by 0.3 eV, $\Delta H^* > 4500 \text{ cm}^{-1}$, and the complex is photochemically stable [101,197].

Low symmetry at the metal mixes $d\pi$ and $d\sigma^*$ orbitals decreasing the MLCT/*dd* energy gap. This effect is seen in [Ru(tpy)₂]^{2+*}, which has a lifetime of 250 ps at room temperature but behaves much like [Ru(bpy)₃]^{2+*} at low temperatures [147,198].

Electron transfer

The first experimental demonstration of excited-state electron transfer by [Ru(bpy)₃]^{2+*} was illustrated in Scheme 1. This initial observation was followed by a plethora of experiments exploring both the extent of the reactivity and the fundamental details of excited-state electron transfer [5,34,35,37,56,199]. In one study, the free energy dependence of electron-transfer quenching was investigated by two functionally related families of oxidants—nitroaromatics, X-C₆H₄-NO₂, ...—bipyridinium dications—MV²⁺, ...—with varying redox potentials [56,200,201] and reductive quenching by a family of aromatic amines.

A generalized scheme for reductive quenching of [Ru(bpy)₃]^{2+*} by NAr₃, Me₂Ar, ... is shown in Scheme 5. The scheme is adapted from an early kinetic analysis by Rehn and Weller [35]. Labels and annotations for the various dynamic events are shown and include: (i) diffusion of the donor (D) to the excited state to form an association complex with $K_{12} = k_{12}/k_{21}$, (ii) electron-transfer quenching, k_{23} , which can be reversible, k_{32} ; (iii) back electron transfer—[Ru(bpy)₃]³⁺, D⁺ → [Ru(bpy)₃]²⁺, D (k_{32})—



Scheme 5 Kinetic scheme for reductive quenching of [Ru(bpy)₃]^{2+*} by an electron-transfer donor, D.

which is in competition with separation to give [Ru(bpy)₃]⁺ + D⁺ (*k*₃₀). The fraction of electron-transfer events resulting in separated redox products is $F_{\text{sep}} = k_{30}/(k_{30} + k_{32})$.

Kinetic analysis of the scheme gives the expression in eq. 31 for the diffusion-corrected (eq. 32) experimental quenching rate constant, k'_{q} . In this equation, $k'_{\text{q}} = k_{23}K_{12}$ with *k*₁₂ the diffusion-limited rate constant, $2 \times 10^{10} \text{ s}^{-1}$ in CH₃CN at 25 °C. *k*_{obs} is the experimentally determined rate constant and is related to k'_{q} as shown in eq. 32.

From eq. 31, k'_{q} is predicted to vary with *K*₁₂, *F*_{sep}, *v*₂₃, and ΔG_{23}^* . The latter are the frequency factor and free energy of activation for the electron-transfer step. From classical Marcus–Hush theory for electron transfer, ΔG_{23}^* is predicted to vary with the free energy change, ΔG_{23} , and reorganization energy, λ , as shown in eqs. 33. $k'_{\text{q},0}$ is the hypothetical rate constant for electron transfer with $\Delta G_{\text{ET}} = 0$.

The free energy change is related to *E*^o values for the D^{+/0} and [Ru(bpy)₃]^{2+*/+} couples by, $\Delta G_{23} \sim -F\{E^{\circ}(\text{D}^{+/0}) - E^{\circ}([\text{Ru}(\text{bpy})_3]^{2+*/+})\}$, with *F* the Faraday constant. Application of electron-transfer theory provides a link between experimental quenching rate constants and ΔG_{23} and, through them, the excited-state redox potential $E^{\circ}([\text{Ru}(\text{bpy})_3]^{2+*/+})$.

$$k'_{\text{q}} = k_{23}K_{12}F_{\text{sep}} = k_{23}K_{12}\{k_{30}/(k_{30} + k_{32})\} = K_{12}F_{\text{sep}}v_{23}\exp(-G_{23}^*/k_{\text{B}}T) \quad (31)$$

$$\frac{1}{k_{\text{obs}}} = \frac{1}{k_{\text{D}}} + \frac{1}{k_{\text{ET}}K_{\text{A}}} \quad (32)$$

$$RT \ln k'_{\text{q}} = RT \ln k'_{\text{q},0} - \frac{\Delta G_{23}}{2} \left(1 + \frac{\Delta G_{23}}{2\lambda} \right) \quad (33a)$$

$$k'_{\text{q},0} = v_{\text{ET}}K_{\text{A}}(4\pi\lambda k_{\text{B}}T)^{-1/2} \exp\left(-\frac{\lambda}{4k_{\text{B}}T}\right) \quad (33b)$$

The result in eq. 33a predicts that $RT \ln k'_{\text{q}}$ should vary quadratically with ΔG_{23} . As shown in Fig. 17, a quadratic dependence is observed consistent with electron-transfer theory. Equation 33a is an approximation in that it assumes common values for *v*₂₃ and λ but the variation of $RT \ln k'_{\text{q}}$ with ΔG_{23} is consistent with an important Marcus–Hush prediction. The correlation through the data in Fig. 17 was calculated with $E^{\circ}([\text{Ru}(\text{bpy})_3]^{2+*/+}) = 0.77 \text{ V vs. SCE}$, $\lambda = 11 \text{ kcal/mol}$ (0.48 eV) and $k'_{\text{q},0} = 8.8 \times 10^8 \text{ M}^{-1} \text{ s}^{-1}$ in CH₃CN, *I* = 0.1 at 22 (±2) °C.

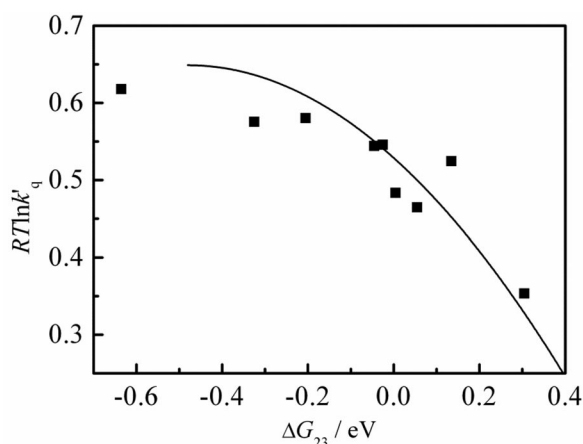
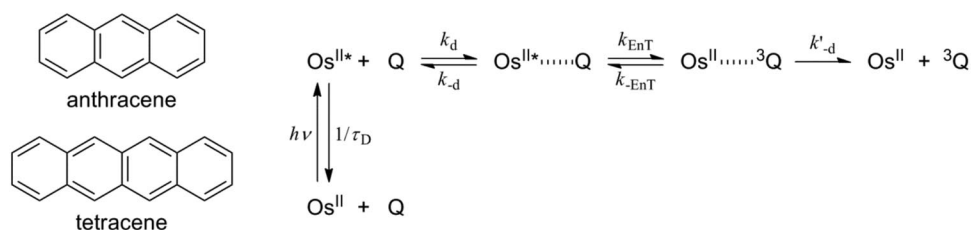


Fig. 17 Plot of $RT \ln k'_q$ vs. ΔG_{23} in CH_3CN , $I = 0.1$ at $22 (\pm 2)^\circ\text{C}$ for the quenching of $[\text{Ru}(\text{bpy})_3]^{2+*}$ by a series of aromatic amines. Data obtained from ref. [56]. The correlation was drawn by using eq. 33a with $k'_{q,0} = 8.8 \times 10^8 \text{ M}^{-1} \text{ s}^{-1}$, and $\lambda = 11 \text{ kcal/mol}$ (0.48 eV).

Energy transfer

Scheme 6 shows a generalized energy-transfer quenching scheme with Q the energy-transfer acceptor. This scheme was applied to energy-transfer quenching of a series of MLCT excited states, $[\text{Os}(\text{bpy})(\text{L})_4]^{2+*}$, by anthracene and tetracene in 3/1 (v/v) $\text{CH}_3\text{CN}/\text{benzene}$ at room temperature [202,203]. The labels for the kinetic steps in Scheme 6 are changed from Scheme 5 with k_d and k_{-d} the rate constants for diffusional formation and dissociation of the association complex— $\text{Os}^{\text{II}*}, Q$ —and k_{EnT} and $k_{-\text{EnT}}$ the forward and reverse energy-transfer rate constants. ΔG_{EnT} is the associated free energy change with $K_{\text{EnT}} = k_{\text{EnT}}/k_{-\text{EnT}} = \exp(-\Delta G_{\text{EnT}}/k_{\text{B}}T)$ [202,203].



Scheme 6 Quencher structures and kinetic scheme for energy-transfer quenching of $[\text{Os}(\text{bpy})_3]^{2+*}$ and related $\text{Os}^{\text{II}*}$ excited states by acceptor $Q = \text{anthracene or tetracene}$.

Kinetic analysis of Scheme 6 gives the expression for the quenching rate constant k'_q , corrected for diffusional effects, in eq. 34. A value for k_{-d} was estimated from the known value for the diffusion-limited rate constant, $k_d = 9.1 \times 10^9 \text{ M}^{-1} \text{ s}^{-1}$ and $K_A (= k_d/k_{-d})$. K_A was evaluated from the Fuoss–Eigen equation [204,205], with $K_A = 4\pi N_A (r_A + r_D)^3/3000 \sim 2.3 \text{ M}^{-1}$ (N_A is Avogadro's number).

$$k'_q = \frac{k_d}{\left(1 + \frac{k_{-d}}{k_{\text{EnT}}} + \frac{1}{k_{\text{EnT}}}\right)} \quad (34)$$

In the quenching experiments, nine complexes were investigated with E_0 varying from 13 600 cm⁻¹ in [Os(bpy)₃]^{2+*} to 19 000 cm⁻¹ in [Os(bpy)₂(dppy)]^{2+*} [dppy is *cis*-1,2-bis(diphenylphosphino)ethylene]. With anthracene as quencher, ΔG_{EnT} varied from +0.05 to -0.72 eV. These reactions occur by triplet-triplet transfer and the Dexter mechanism in Scheme 6. From time-dependent perturbation theory with application of the Condon approximation, k_{EnT} is given by eq. 35, or in logarithmic form, by eq. 36. The frequency factor for energy transfer, ν_{EnT} , is given by eq. 37 with V_{DA} the electron exchange matrix element. In the classical limit, k_{EnT} is given by eq. 38.

$$k_{\text{EnT}} = \left(\frac{2\pi V_{\text{DA}}^2}{\hbar} \right) \text{FC}(\text{calc}) \quad (35)$$

$$\ln k_{\text{EnT}} = \ln \nu_{\text{EnT}} + \ln [\text{FC}(\text{calc})] \quad (36)$$

$$\ln \nu_{\text{EnT}} = \ln \left(\frac{2\pi V_{\text{DA}}^2}{\hbar} \right) \quad (37)$$

$$k_{\text{EnT}} = \nu_{\text{EnT}} \exp \left[- \frac{(\Delta G_{\text{EnT}} + \lambda_{\text{DA}})^2}{4\lambda_{\text{DA}} k_{\text{B}} T} \right] \quad (38)$$

Emission spectral fitting was used to evaluate the parameters defining the Franck-Condon density of states $\text{FC}(\text{calc}) - E_0$, $\hbar\omega$, S and $\Delta\tilde{\nu}_{0,1/2}$ and ΔG_{EnT} . With values available for k_{d} , $k_{-\text{d}}$, K_{EnT} , and $\text{FC}(\text{calc})$, variations in k'_{q} with ΔG_{EnT} were fit to eq. 34 to obtain ν_{EnT} ($= 2\pi V_{\text{DA}}^2/\hbar$). A fit of the experimental data to eq. 34 with $V_{\text{DA}} = 2.5 \text{ cm}^{-1}$ is shown in Fig. 18.

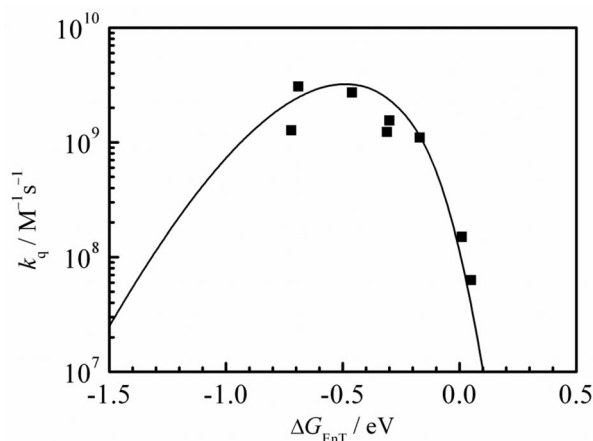


Fig. 18 Dependence of k'_{q} on ΔG_{EnT} for anthracene quenching of Os^{II*} in 3/1 (v/v) CH₃CN/benzene at room temperature. Data obtained from ref. [203]. Solid curve shows a fit to eq. 34 with $V_{\text{DA}} = 2.5 \text{ cm}^{-1}$.

As for nonradiative decay, the results of the analysis were impressive in demonstrating the successful application of theory and spectroscopically derived kinetic parameters in providing a quantitative account of a dynamic event, in this case, energy transfer. The data also provided the first experimental observation of energy transfer in the “inverted region” with a decrease in k'_{q} occurring past the maximum value at $\Delta G_{\text{EnT}} = -0.69 \text{ eV}$ in Fig. 18. The inverted effect is even more dramatic for tetracene as quencher where k'_{q} values as low as $3 \times 10^8 \text{ M}^{-1}\text{s}^{-1}$ were observed. In the inverted region, $-\Delta G_{\text{EnT}} > \lambda$, and further increases in $-\Delta G_{\text{EnT}}$ result in slower energy transfer and a decrease in k'_{q} .

As can be seen in Fig. 18, in the normal region, the observed dependence on ΔG_{EnT} has the classical parabolic shape predicted by eq. 38. In the inverted region, an onset of the linear dependence predicted by the energy gap law begins to appear [206,207]. For tetracene as quencher, decreases in ΔG_{EnT} past -0.8 eV results in an increase in k'_q as quenching by the second triplet excited state of tetracene, T_2 , intervenes [203]. For tetracene, the complete data set could be fit to a two-state quencher model with $E_0 = 10\,200\text{ cm}^{-1}$ and $V_{\text{DA}} = 2.5\text{ cm}^{-1}$ for T_1 and $E_0 = 18\,500\text{ cm}^{-1}$ and $V_{\text{DA}} = 8\text{ cm}^{-1}$ for T_2 .

ASSEMBLIES, CHROMOPHORE–QUENCHER COMPLEXES, POLYMERS, OLIGOPROLINES

If the initial observation of electron-transfer quenching of $[\text{Ru}(\text{bpy})_3]^{2+*}$ opened a new door to possible solar energy conversion schemes, it also revealed formidable challenges. Diffusional excitation and quenching as in Scheme 1 are unproductive because the transiently stored redox equivalents are lost as heat when back electron transfer occurs. Useful application requires architectures where the separate half-reactions for water oxidation and reduction or water oxidation and CO_2 reduction are spatially separated while minimizing competition from back electron transfer. The underlying elements to be included are clear: (1) light absorption; (2) excited-state electron transfer and/or energy transfer; (3) separation of oxidative and reductive equivalents by intramolecular electron transfer driven by free energy gradients; (4) electron transfer activation of catalysts for carrying out the multi-electron, multi-proton half-reactions for water oxidation and water/ CO_2 reduction; (5) integration into device configurations.

In response to these challenges, a systematic “modular approach” was initiated in which separate components for light absorption, etc. were investigated separately and integrated in assembly architectures. Although not a major theme of this account, the evolution of these strategies and the molecular systems that evolved are a notable outcome.

Chromophore–quencher complexes

A series of “chromophore–quencher” complexes with chromophore and quencher linked by chemical bonds were designed with the goal of converting diffusional electron and energy-transfer quenching into intramolecular equivalents [208,209]. In the resulting assemblies, rates of intramolecular excitation and quenching are greatly accelerated with the bonus of spatial control of redox equivalents after they are produced.

Electron transfer

The first chromophore–quencher complex for investigating intramolecular electron transfer was $[\text{Ru}(\text{bpy})_2(\text{MQ}^+)]^{4+}$ (MQ^+ is *N*-methyl-4,4'-bipyridine cation, Fig. 19). Following initial $\text{Ru}^{\text{II}} \rightarrow \text{bpy}$ excitation, intramolecular electron transfer occurs to coordinated MQ^+ , $[(\text{bpy}^{\bullet-})\text{Ru}^{\text{III}}(\text{MQ}^+)]^{4+*} \rightarrow [(\text{bpy})\text{Ru}^{\text{III}}(\text{MQ}^0)]^{4+}$ giving a MQ^+ -based excited state that emits [210]. In $[\text{Re}(\text{bpy})(\text{CO})_3(\text{py-PTZ})]^+$ initial $\text{Re}^{\text{I}} \xrightarrow{h\nu} \text{bpy}$ excitation is followed by transfer of the oxidative equivalent at Re^{II} in the $\text{Re}^{\text{II}}(\text{bpy}^{\bullet-})$ excited state to $-\text{PTZ}$, $[\text{Re}^{\text{II}}(\text{bpy}^{\bullet-})(\text{CO})_3(\text{py-PTZ})]^+ \rightarrow [\text{Re}^{\text{I}}(\text{bpy}^{\bullet-})(\text{CO})_3(\text{py-PTZ}^{\bullet+})]^+$ [211,212]. In $[\text{Ru}(\text{dmb})(\text{bpyCH}_2\text{PTZ})(\text{bpyCH}_2\text{-MV}^{2+})]^{4+}$, $\text{Ru}^{\text{II}} \rightarrow \text{bpy}$ excitation is followed by a series of electron-transfer events leading to the redox separated state $[\text{Ru}(\text{dmb})(\text{bpyCH}_2\text{PTZ}^{\bullet+})(\text{bpyCH}_2\text{-MV}^{\bullet+})]^{4+}$ with oxidative and reductive equivalents oriented spatially on different bpy ligands [213].

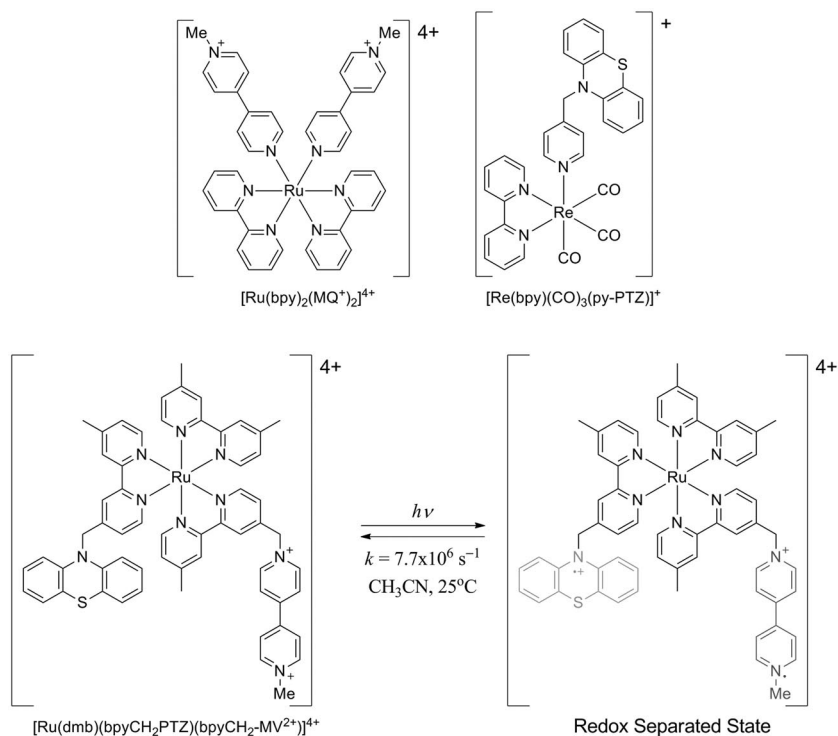


Fig. 19 Structures of $[\text{Ru}(\text{bpy})_2(\text{MQ}^+)_2]^{4+}$, $[\text{Re}(\text{bpy})(\text{CO})_3(\text{py-PTZ})]^+$, $[\text{Ru}(\text{dmb})(\text{bpyCH}_2\text{PTZ})(\text{bpyCH}_2\text{-MV}^{2+})]^{4+}$, and its redox separated state, $[\text{Ru}(\text{dmb})(\text{bpyCH}_2\text{PTZ}^+)(\text{bpyCH}_2\text{-MV}^+)]^{4+}$.

Energy transfer

As noted in the section “What exactly is $[\text{Ru}(\text{bpy})_3]^{2+*}$ ”, MLCT excitation of $[\text{Ru}(\text{dmb})_2(4\text{-Me-4'-(CH}_2\text{CH}_2\text{An)bpy)]^{2+}$ is followed by intramolecular energy transfer to $-^3\text{An}$ with components at $\tau \sim 23$ and 72 ps due to, $\text{Ru}^{\text{III}}(\text{bpy}^{\bullet-})\text{-CH}_2\text{CH}_2\text{-An} \rightarrow \text{Ru}^{\text{II}}(\text{bpy})\text{-CH}_2\text{CH}_2\text{-}^3\text{An}$, energy transfer and slower, $\text{Ru}^{\text{III}}(\text{dmb}^{\bullet-}) \rightarrow \text{Ru}^{\text{III}}(\text{bpy}^{\bullet-})\text{-CH}_2\text{CH}_2\text{-An}$, dipole rotation followed by energy transfer [65,214]. Direct $\pi \rightarrow \pi^*$ excitation of $-\text{An}$ in the near UV resulted in rapid appearance of $-^3\text{An}$ with the intervening $^1,3\text{MLCT}$ excited state manifold providing a “spin switch”. Once formed, the appended $-^3\text{An}$ excited state provided a longer time window for diffusional quenching by MV^{2+} .

Polymers

Derivatized polymers provide a way to integrate multiple functional groups in single assemblies. Derivatized polystyrenes have been especially useful with multiple chromophores available for potential antenna applications combined with functional elements for excited-state electron or energy transfer. In an initial series of experiments, free radical polymerization of *meta*- and *para*-methylchlorostyrenes with AIBN (azobisisobutyronitrile) as a radical initiator yielded a series of atactic polymers which were derivatized to give the series $[\text{co-}m,p\text{-PS-CH}_2\text{-R}]$ with $-\text{R} = [\text{Ru}(4\text{-Me-4'-(OCH}_2\text{)-bpy})(\text{bpy})_2]^{2+}$ ($-\text{OCH}_2\text{-Ru}^{\text{II}}$), $-\text{MQ}^{2+}$, or $-\text{PTZ}$. The polymers were of varying molecular weights and polydispersities, structures are shown in Fig. 20 [215–217]. In dilute solutions containing the derivatized $-\text{OCH}_2\text{-Ru}^{\text{II}}$, $-\text{MQ}^{2+}$, and $-\text{PTZ}$ polymers, photolysis led to no net photochemistry. However, with addition of 9-methylanthracene (9-MeAn) as an energy/electron transfer shuttle, the sequence of energy/electron transfer events shown in Scheme 7 occurred resulting in oxidative, $-\text{PTZ}^+$,

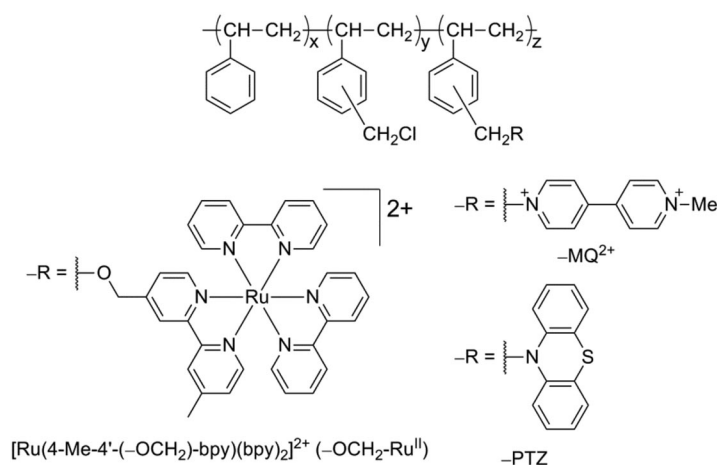
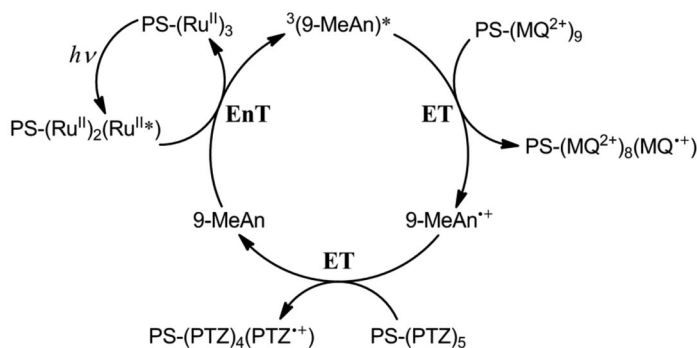


Fig. 20 Structures of the atactic, derivatized polymers [*co-m,p*-PS-CH₂-R] (–R = [Ru(4-Me-4'-(–OCH₂)bpy)(bpy)₂]²⁺ (–OCH₂-Ru^{II}), –MQ²⁺, and –PTZ).



Scheme 7 Electron- (ET) and energy-transfer (EnT) shuttle mechanism with added 9-MeAn.

and reductive equivalents, –MQ⁺, on separated polymer strands and greatly delayed back electron transfer.

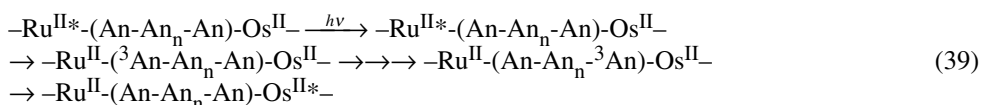
The polymer linkage chemistry was developed further, in one series with intervening –CH₂OCH₂– spacers in 1:1 (styrene:derivatized-styrene) copolymers [218,219]. Amide coupling of the chromophores to the polystyrene backbone gave the copolymer series [*co-p*-PS-CH₂NHCO-R], and the homopolymer series [*co-p*-PS-CH₂CH₂NHCO-R] with the extra –CH₂– spacer added to achieve full loading, Fig. 21.

Photophysical measurements on the resulting family of structurally related polymer assemblies were used to explore the role of local structure on inter- and intra-assembly energy and electron-transfer dynamics and the cataloging of some notable results:

- (i) *Multi-electron, multi-photon photochemistry.* Laser flash photolysis of [*co*-PS-CH₂-(–OCH₂-Ru^{II})₃₀]⁶⁰⁺ at high incident irradiances resulted in multiple excitation of Ru^{II} sites in single polymer chains. In the presence of excess phenothiazine (PTZ, Fig. 20) multiple excitation followed by multiple electron-transfer events during single laser flashes resulting in the transient storage of, on the average, seven reductive equivalents on single polymer strands, [*co*-PS-CH₂-(–OCH₂-Ru^{II})₃₀]⁶⁰⁺ + 7*hν* + 7PTZ → [*co*-PS-CH₂-(–OCH₂-Ru^{II})₂₃(–OCH₂-Ru^I)₇]⁵³⁺ + 7PTZ^{•+} [219].

- (ii) *Intrastrand energy transfer.* Flash photolysis of [co-PS-CH₂-(–OCH₂-Ru^{II})₃(–OCH₂-Os^{II})₃]⁶⁺, with only 6 of the 30 available sites derivatized by a Ru^{II} or Os^{II} polypyridyl complex, resulted in the photophysical behavior expected for isolated sites in the homo-polymers [co-PS-CH₂-(–OCH₂-M^{II})₃]⁶⁺. Ru^{II*} → Os^{II} energy transfer is favored by –0.36 eV [220]. With Os^{II} replaced by –An in [co-PS-CH₂-(–OCH₂-Ru^{II})₃(An)₆]³⁺, laser flash photolysis led to energy-transfer quenching of ³Ru²⁺* by –An, which is favored by –0.3 eV. The quenching rate constant was $k_q = 8 \times 10^6 \text{ s}^{-1}$ with energy transfer occurring, on the average, over an estimated separation distance of ~21 Å if the polymer were fully extended [221]. Energy-transfer quenching in this case was attributed to conformational flexibility in the partly loaded polymer.

With the remaining un-derivatized sites on the polymer occupied with added –An, to give [co-PS-CH₂-(–OCH₂-Ru^{II})₃(An)₁₂(–OCH₂-Os^{II})₃]⁶⁺, rapid Ru^{II*} → Os^{II} energy transfer occurred by an intra-strand “light pipe” mechanism, eq. 39, with Ru^{II*} → –An energy transfer followed by ³An → –An energy-transfer hopping and sensitization of Os^{II*} [215,216].



- (iii) *Linkage dependence, excited-state orientation with an amide linkage strategy.* Substituents in the 4,4'-positions on bpy, –CH₃ and –CH₂OCH₂– are electron-donating. Because of this substituent effect, in ether-linked, derivatized polymers based on [Ru(4-Me-4'-(–CH₂OCH₂-bpy)(bpy)₂]²⁺, the lowest MLCT excited-state dipole is oriented away from the polymer backbone and intra-strand energy transfer is slow. Overcoming this limitation led to the amide-linked polymers in Fig. 21 [222,223]. In these polymers, the lowest MLCT excited state is oriented toward the polystyrene backbone. The change in excited-state orientation promoted facile intra-strand energy and electron transfer.
- (iv) *Intra-strand energy migration in [co-PS-CH₂CH₂NHCO-(Ru^{II})₁₁(Os^{II})₅](PF₆)₃₂.* In this mixed Ru^{II}-Os^{II} co-polymer, Ru^{II} excitation leads to rapid intra-strand energy transfer migration, –Ru^{II*}-Ru^{II}– → –Ru^{II}-Ru^{II*}– to the Os^{II} trap sites where rapid energy transfer occurs, –Ru^{II*}-Os^{II}– → –Ru^{II}-Os^{II*}–. Intra-strand energy transfer occurred with an efficiency >90 % at 298 K [224].
- (v) *Sensitization of a redox separated state.* The amide-linked assembly [co-PS-CH₂NHC(O)-(Ru^{II})₁₇(RC)₃]⁴⁶⁺ was constructed as a functional mimic of the photosynthetic reaction center. The derivatized polystyrene polymer shown in Scheme 8 contains both poly-PS-Ru^{II} “antenna” units and a local “reaction center” mimic with PTZ electron-transfer donor and MQ²⁺ electron acceptors on separate bpy ligands. PS-Ru^{II} excitation and intra-strand energy transfer occur to the RC mimic followed by internal electron transfer to give appended Ru(bpy-MQ⁺)(bpy-PTZ⁺). In the redox separated state that results, 1.15 eV of the initial excitation energy was stored transiently formed with a quantum efficiency of 12 to 18 % depending on laser irradiance [225].

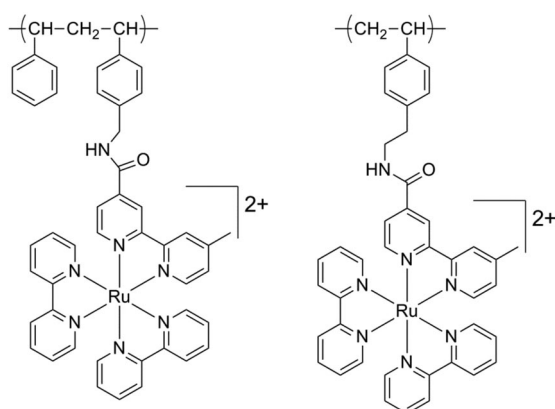
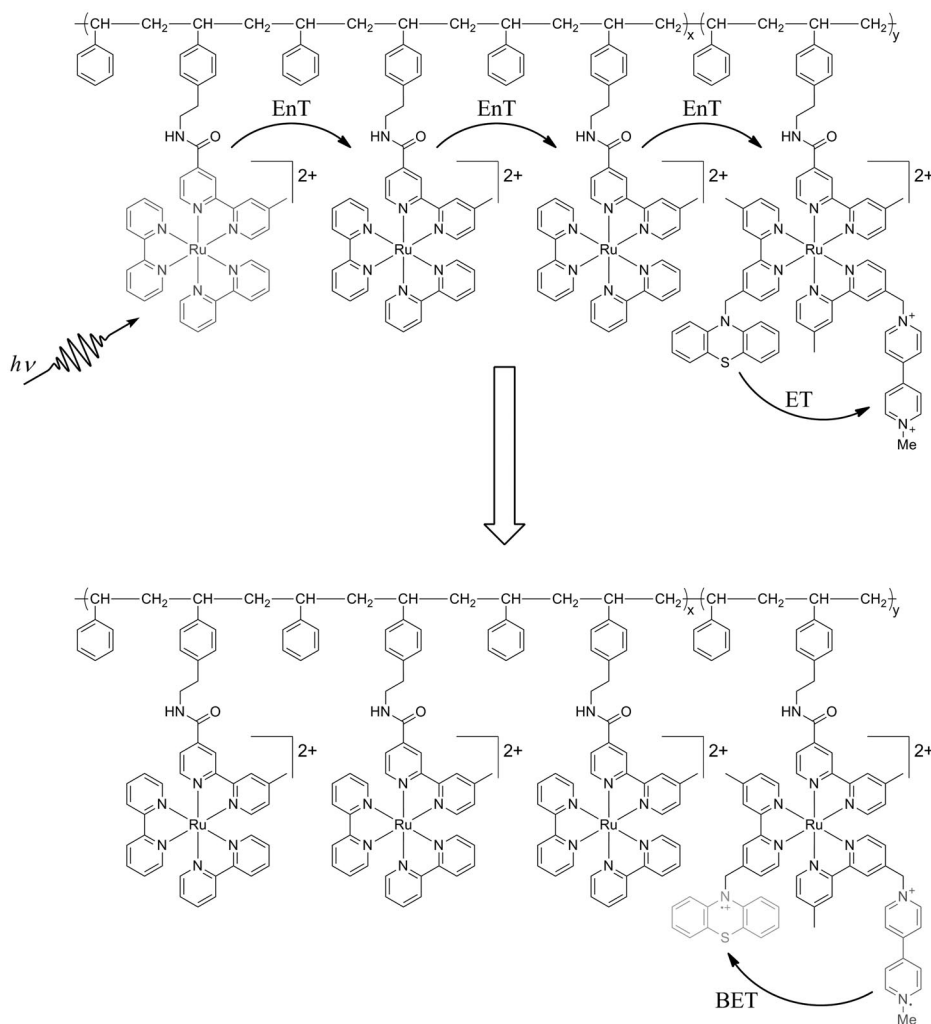


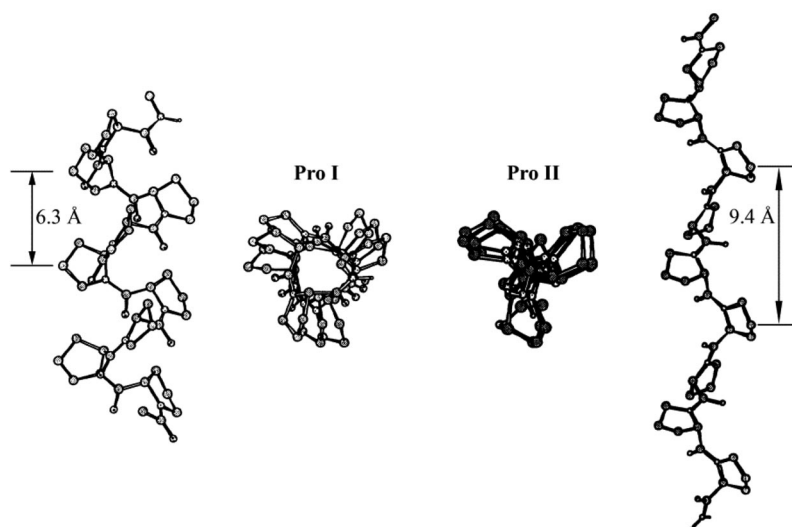
Fig. 21 Structures of amide-linked, Ru^{II}-derivatized polystyrene polymers.



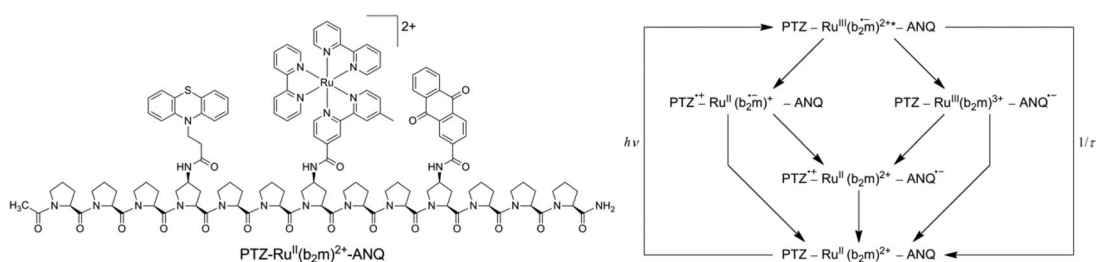
Scheme 8 Sensitization of electron transfer in the polystyrene-based antenna-reaction center model.

Oligoprolines

Derivatization of preformed polymers is inherently random in terms of the relative placement of chromophores and added electron- or energy-transfer functional groups on the polymer backbone. Spatial control at the molecular level was investigated by exploiting solid-state peptide synthesis and the Merrifield technique. In this step-by-step approach, assemblies are synthesized with controlled placement of individual groups in the growing peptide chain. In this approach, the order of synthesis controls content providing spatial control. With proline-based assemblies, oligoprolines that exceed six repeat units typically form 3D helical structures, either Pro I and Pro II, with the distribution between them solvent-dependent, Scheme 9. Pro I is a right-handed helix formed from local *cis*-amide bonds and is favored in less-polar solvents. Pro II, adopts a left-handed helical structure and is favored in polar solvents with a repeat spacing of 9.4 Å compared to 6.3 Å in Pro I [226–228]. A kinetic scheme for excitation and electron transfer in a Ru-bpy based oligoprolinone with both electron-transfer donor –PTZ and acceptor –ANQ (anthraquinone) groups, PTZ-Ru^{II}(b₂m)²⁺-ANQ, is shown in Scheme 10 [229,230].

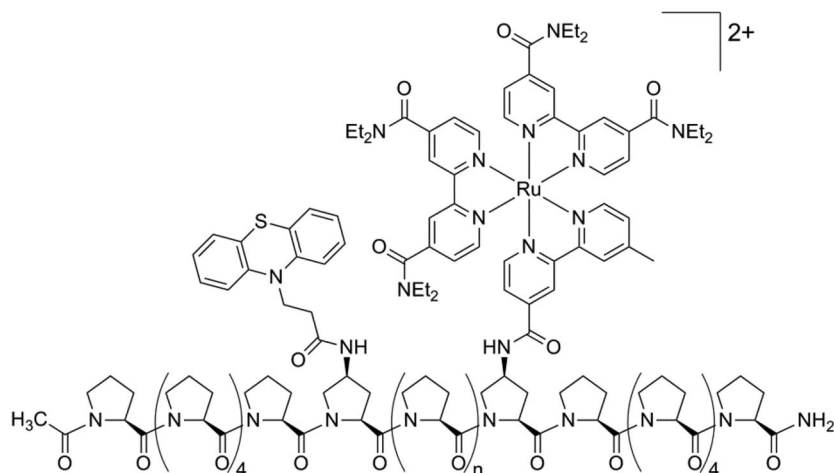


Scheme 9 Structures of oligoprolinone helices, Pro I and Pro II. Adapted from ref. [228]. Also shown is the separation distance for a full turn of the helix.



Scheme 10 Chemical structure of oligoprolinone assembly PTZ-Ru^{II}(b₂m)²⁺-ANQ and a kinetic scheme for events following excitation and electron transfer.

An important theme in electron-transfer research is the study of the distance dependence of electron transfer and whether electron transfer occurs through bond or through space. In the oligoproline assembly shown in Fig. 22, the distance between the chromophore and –PTZ electron-transfer donor was varied by increasing the number of proline residues from $n = 2$ to $n = 5$. Analysis of the distance dependence of –PTZ quenching of the Ru^{2+*} excited state, which occurs in the Marcus “normal” region with $|\Delta G^0| < \lambda$, and back electron transfer, which occurs in the inverted region with $|\Delta G^0| > \lambda$, revealed that, for both, electron transfer was through-space and not through-bond [231].



Scheme 11 Structures of the oligoproline-based Ru^{II} -PTZ assemblies with $n = 2$ –5.

A related study on energy transfer in a related series of oligoprolines containing the $-\text{Ru}^{\text{II}}-\text{Ru}^{\text{II}*}-\text{Os}^{\text{II}}-$ core has shown that the distance dependences of both $-\text{Ru}^{\text{II}*} \rightarrow -\text{Ru}^{\text{II}}$ and $-\text{Ru}^{\text{II}*} \rightarrow -\text{Os}^{\text{II}}$ energy transfer are consistent with the Dexter mechanism [232].

DYE-SENSITIZED PHOTOELECTROSYNTHESIS CELLS (DSPECs)

Something new emerged from Scheme 1 and the observation that $[\text{Ru}(\text{bpy})_3]^{2+*}$ could undergo electron transfer—an approach to artificial photosynthesis based on molecules and molecular-level phenomena. Using molecular-level reactivity and a “modular approach” is appealing since individual molecular components for light absorption, electron transfer, and catalysis can be investigated separately and integrated into multi-functional arrays. This is the strategy that natural photosynthesis uses, but the photosynthetic apparatus is amazingly complex and took eons to evolve. It is also inefficient with biomass yields typically $< 1\%$. A shorter timescale is needed with far higher efficiencies for a practical working device.

An integrated molecular strategy like the one used in photosynthesis poses enormous synthetic challenges arising from preparing and then assembling the required components in appropriate architectures. A shortcut is available by using a hybrid approach derived from DSSCs that use molecular-level excitation and excited states to produce a photovoltage and photocurrent [233–240].

DSSCs consist of mesoporous, nanoparticle films of optically transparent, wide bandgap semiconductors, typically TiO_2 , deposited on a transparent conducting substrate like tin-doped indium oxide (ITO). Surface binding and excitation of a chromophore or “dye” surface-bound to TiO_2 leads to electron injection into the conduction band of the semiconductor. The oxidized dye is subsequently reduced by the reduced component of a redox mediator couple, typically I_3^-/I^- . The excess I_3^- diffuses to an

external cathode where it is reduced by the photo-produced electrons at the conduction band potential of the photoanode. The maximum photopotential in a DSSC is given by the Nernst equation and the difference in potentials between the semiconductor conduction band potential and the potential of the I₃⁻/I⁻ couple.

DSPECs combine the advantages of DSSCs with the molecular/modular approach for producing solar fuels [8,9,241]. Instead of producing a photopotential and photocurrent, the oxidative equivalents produced by injection are used to produce oxygen at an anode and hydrogen or a reduced carbon product at the cathode. A cartoon illustrating a tandem DSPEC for water oxidation at a photoanode and CO₂ reduction at a photocathode is shown in Fig. 22. The first example of a DSPEC appeared in 1999 for the dehydrogenation of isopropanol [54], and Mallouk and co-workers have demonstrated water splitting with this approach [242,243]. Working DSPEC devices for hydrogen production with EDTA or triethanolamine added as reductive scavengers has been demonstrated with high per photon absorbed efficiencies with an added bias [244,245].

The heart of the DSPEC design in Fig. 22 originates in Scheme 1 and [Ru(bpy)₃]^{2+*} electron-transfer quenching. The key element at the photoanode is the “chromophore-catalyst” assembly. The chromophore absorbs light, the resulting excited state injects an electron into the conduction band of the semiconductor, and oxidative equivalents are transferred to the catalyst by intra-assembly electron transfer. Oxygen is released following the build-up of the four oxidative equivalents required for water oxidation. The right-hand electrode is a photocathode based on NiO or other p-type semiconductor. At the photocathode, light absorption and excitation by a second chromophore-quencher assembly results in electron transfer *from* the valence band of the semiconductor to the chromophore excited state. Intra-molecular electron transfer from the reduced chromophore activates an external catalyst toward water or CO₂ reduction.

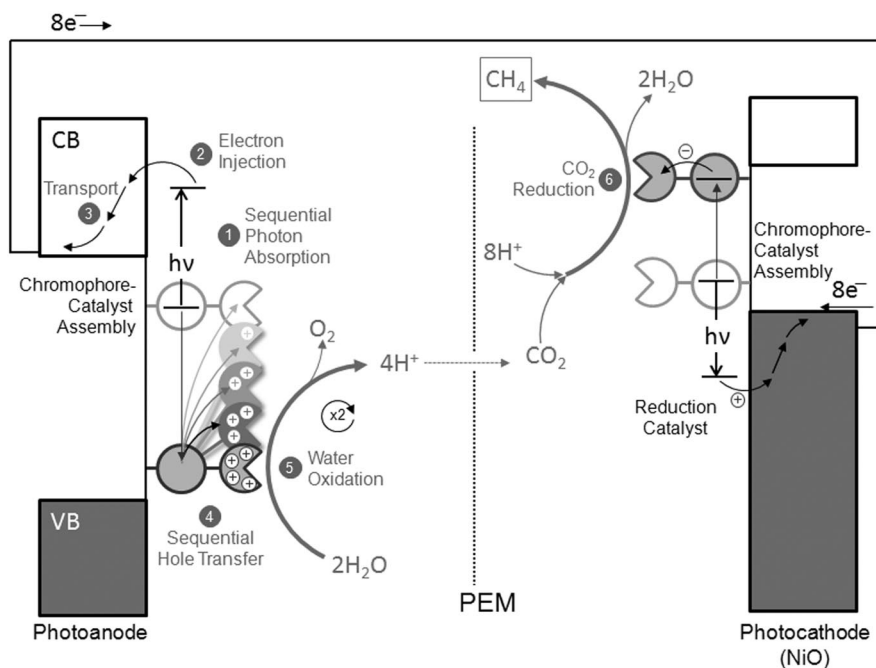


Fig. 22 Tandem DSPEC for water reduction of CO₂ to methane at a photocathode and light-driven water oxidation at a photoanode. The sequence of events illustrated at the photoanode are: (1) photon absorption, (2) excited-state electron injection, (3) electron transport to the cathode, (4) intramolecular hole transfer, (5) water oxidation, (6) light-driven CO₂ reduction at the photocathode. PEM is a proton exchange membrane.

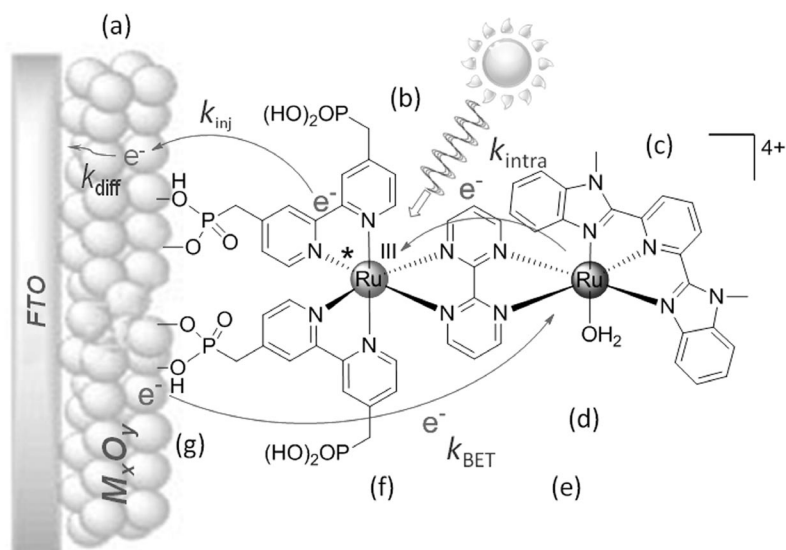


Fig. 23 Dynamic events and challenges for photoelectrochemical water oxidation in a DSPEC photoanode: (a) *Semiconductor*: surface binding, conduction band potential appropriate for water/ CO_2 reduction; electron collection efficiency; (b) *Light absorption*: near UV to ~ 900 nm; high injection efficiency; weak or non-light absorbing catalyst; (c) *Molecular catalysis*: catalysis rate \gg back electron transfer rate; 10–20 million turnovers/yr; (d) *Chromophore-catalyst*: light absorption; surface stability; electron injection-intra-assembly electron-transfer dynamics; (e) *Device evaluation*: I - V characteristics; product analysis; scale up; (f) *Electron-transfer dynamics*: high injection efficiencies; rapid intramolecular electron transfer; slow back electron transfer; (g) *Surface binding, stability*: Stable over a wide pH range; 10–20 million turnovers/yr. FTO: fluoride-doped tin oxide; M_xO_y : metal oxide, usually TiO_2 .

The DSPEC approach offers a way to “close the loop” on energy conversion by $[\text{Ru}(\text{bpy})_3]^{2+*}$ but there are many obstacles to success. Figure 23 provides a summary and illustrates the dynamic events that occur following excitation. It also provides an overview and the figure caption a summary. The figure illustrates a surface-bound phosphonate assembly bound to the nanoparticle semiconductor oxide M_xO_y on the optically transparent conducting oxide FTO, fluoride-doped tin oxide.

POSTSCRIPT

Much has happened since the first account of $[\text{Ru}(\text{bpy})_3]^{2+*}$ electron transfer appeared in 1974. The synthetic chemistry for preparing MLCT chromophores has blossomed, as has the synthesis of complex molecules and assemblies that incorporate them. The excited states themselves have provided an unprecedented opportunity to probe the intimate details of excited-state structure and dynamics, and techniques have evolved for looking ever more deeply. Theory combined with experiment has provided a framework for understanding and predicting excited-state properties in an impressive and productive way.

The combination of stability, light absorption, and excited-state dynamics has opened the door to important applications for $[\text{Ru}(\text{bpy})_2]^{2+*}$, its cousins, and their derivatives in a variety of areas. With the advent of the DSPEC approach to artificial photosynthesis, a systematic approach is available for returning to the initial promise of Scheme 1 with a hybrid molecular approach for utilizing the sun to make solar fuels. Progress has been impressive, there is more to come.

ACKNOWLEDGMENTS

The authors acknowledge support from the U.S. Department of Energy, Office of Science, Office of Basic Energy Sciences, under Award Number DE-FG02-06ER15788.

REFERENCES

1. V. Balzani, F. Scandola. *Supramolecular Photochemistry*, Horwood, Chichester (1991).
2. K. Kalyanasundaram. *Photochemistry of Polypyridine and Porphyrin Complexes*, Academic Press, London (1992).
3. D. M. Roundhill. *Photochemistry and Photophysics of Metal Complexes*, Plenum, New York (1994).
4. A. Juris, V. Balzani, F. Barigelletti, S. Campagna, P. Belsler, A. von Zelewsky. *Coord. Chem. Rev.* **84**, 85 (1988).
5. M. Z. Hoffman, F. Bolletta, L. Moggi, G. L. Hug. *J. Phys. Chem. Ref. Data* **18**, 219 (1989).
6. V. Balzani, A. Credi, M. Venturi. *Coord. Chem. Rev.* **171**, 3 (1998).
7. A. Vlček Jr., M. Busby. *Coord. Chem. Rev.* **250**, 1755 (2006).
8. T. J. Meyer. *Acc. Chem. Res.* **22**, 163 (1989).
9. J. H. Alstrum-Acevedo, M. K. Brennaman, T. J. Meyer. *Inorg. Chem.* **44**, 6802 (2005).
10. J. G. Vos, J. M. Kelly. *Dalton Trans.* 4869 (2006).
11. V. Balzani, G. Bergamini, P. Ceroni. *Coord. Chem. Rev.* **252**, 2456 (2008).
12. J. J. Concepcion, J. W. Jurss, M. K. Brennaman, P. G. Hoertz, A. O. T. Patrocínio, N. Y. Murakami Iha, J. L. Templeton, T. J. Meyer. *Acc. Chem. Res.* **42**, 1954 (2009).
13. F. H. Burstall. *J. Chem. Soc.* 173 (1936).
14. G. Morgan, F. H. Burstall. *J. Chem. Soc.* 1649 (1937).
15. F. H. Burstall. *J. Chem. Soc.* 1662 (1938).
16. G. Morgan, F. H. Burstall. *J. Chem. Soc.* 1672 (1938).
17. G. Morgan, F. H. Burstall. *J. Chem. Soc.* 1675 (1938).
18. F. H. Burstall, F. P. Dwyer, E. C. Gyarfas. *J. Chem. Soc.* 953 (1950).
19. F. P. Dwyer, E. C. Gyarfas. *J. Am. Chem. Soc.* **73**, 2322 (1951).
20. W. W. Brandt, F. P. Dwyer, E. D. Gyarfas. *Chem. Rev.* **54**, 959 (1954).
21. A. von Zelewsky. *Stereochemistry of Coordination Compounds*, John Wiley, New York (1996).
22. L. Flamigni, F. Barigelletti, N. Armaroli, J.-P. Collin, I. M. Dixon, J.-P. Sauvage, J. A. G. Williams. *Coord. Chem. Rev.* **190–192**, 671 (1999).
23. S. Fanni, T. E. Keyes, C. M. O'Connor, H. Hughes, R. Wang, J. G. Vos. *Coord. Chem. Rev.* **208**, 77 (2000).
24. L. Spiccia, G. B. Deacon, C. M. Kepert. *Coord. Chem. Rev.* **248**, 1329 (2004).
25. P. Sun, A. Krishnan, A. Yadav, S. Singh, F. M. MacDonnell, D. W. Armstrong. *Inorg. Chem.* **46**, 10312 (2007) and refs. therein.
26. E. C. Constable. *Coord. Chem. Rev.* **252**, 842 (2008).
27. T. J. Meyer, M. H. V. Huynh. *Inorg. Chem.* **42**, 8140 (2003).
28. J. J. Concepcion, J. W. Jurss, J. L. Templeton, T. J. Meyer. *Proc. Natl. Acad. Sci. USA* **105**, 17632 (2008).
29. D. J. Stufkens, A. Vlček Jr. *Coord. Chem. Rev.* **177**, 127 (1998).
30. A. Vlček Jr. *Coord. Chem. Rev.* **230**, 225 (2002).
31. J. K. Hurst. *Coord. Chem. Rev.* **249**, 313 (2005).
32. C. Kaes, A. Katz, M. W. Hosseini. *Chem. Rev.* **100**, 3553 (2000).
33. A. Fujishima, K. Honda. *Nature* **238**, 37 (1972).
34. C. R. Bock, T. J. Meyer, D. G. Whitten. *J. Am. Chem. Soc.* **96**, 4710 (1974).
35. D. Rehm, A. Weller. *Ber. Bunsen-Ges. Phys. Chem.* **73**, 834 (1969).

36. H. D. Gafney, A. W. Adamson. *J. Am. Chem. Soc.* **94**, 8238 (1972).
37. R. C. Young, T. J. Meyer, D. G. Whitten. *J. Am. Chem. Soc.* **97**, 4781 (1975).
38. S. A. Adeyemi, A. Dvletoglou, A. R. Guadalupe, T. J. Meyer. *Inorg. Chem.* **31**, 1375 (1992).
39. A. J. Morris, G. J. Meyer, E. Fujita. *Acc. Chem. Res.* **42**, 1983 (2009).
40. Z. Chen, J. J. Concepcion, M. K. Brennaman, P. Kang, M. R. Norris, P. G. Hoertz, T. J. Meyer. *Proc. Natl. Acad. Sci. USA* **109**, 15606 (2012).
41. J. Barber, B. Andersson. *Nature* **370**, 31 (1994).
42. V. K. Yachandra, K. Sauer, M. P. Klein. *Chem. Rev.* **96**, 2927 (1996).
43. K. N. Ferreira, T. M. Iverson, K. Maghlaoui, J. Barber, S. Iwata. *Science* **303**, 1831 (2004).
44. B. Loll, J. Kern, W. Saenger, A. Zouni, J. Biesiadka. *Nature* **438**, 1040 (2005).
45. J. Barber. *Biochem. Soc. Trans.* **34**, 619 (2006).
46. J. P. McEvoy, G. W. Brudvig. *Chem. Rev.* **106**, 4455 (2006).
47. J. Yano, J. Kern, K. Sauer, M. J. Latimer, Y. Pushkar, J. Biesiadka, B. Loll, W. Saenger, J. Messinger, A. Zouni, V. K. Yachandra. *Science* **314**, 821 (2006).
48. J. Kern, G. Renger. *Photosynth. Res.* **94**, 183 (2007).
49. T. J. Meyer, M. H. V. Huynh, H. H. Thorp. *Angew. Chem., Int. Ed.* **46**, 5284 (2007).
50. G. W. Brudvig. *Philos. Trans. R. Soc. B: Biol. Sci.* **363**, 1211 (2008).
51. G. Renger, T. Renger. *Photosynth. Res.* **98**, 53 (2008).
52. H. Dau, I. Zaharieva. *Acc. Chem. Res.* **42**, 1861 (2009).
53. J. J. Concepcion, R. L. House, J. M. Papanikolas, T. J. Meyer. *Proc. Natl. Acad. Sci. USA* **109**, 15560 (2012).
54. J. A. Treadway, J. A. Moss, T. J. Meyer. *Inorg. Chem.* **38**, 4386 (1999).
55. D. L. Ashford, W. Song, J. J. Concepcion, C. R. K. Glasson, M. K. Brennaman, M. R. Norris, Z. Fang, J. L. Templeton, T. J. Meyer. *J. Am. Chem. Soc.* **134**, 19189 (2012).
56. C. R. Bock, J. A. Connor, A. R. Gutierrez, T. J. Meyer, D. G. Whitten, B. P. Sullivan, J. K. Nagle. *J. Am. Chem. Soc.* **101**, 4815 (1979).
57. A. Ito, T. J. Meyer. *Phys. Chem. Chem. Phys.* **14**, 13731 (2012).
58. A. Ito, J. J. Concepcion, T. J. Meyer et al. Manuscript in preparation.
59. E. M. Kober, B. P. Sullivan, W. J. Dressick, J. V. Caspar, T. J. Meyer. *J. Am. Chem. Soc.* **102**, 7383 (1980).
60. E. M. Kober, T. J. Meyer. *Inorg. Chem.* **21**, 3967 (1982). Note that figures for low-temperature spectra of $[\text{Fe}(\text{bpy})_3]^{2+}$ and $[\text{Os}(\text{bpy})_3]^{2+}$ are reversed.
61. H. Riesen, E. Krausz. *J. Chem. Phys.* **99**, 7614 (1993).
62. H. Riesen, L. Wallace, E. Krausz. *Int. Rev. Phys. Chem.* **16**, 291 (1997).
63. E. M. J. Johansson, M. Odelius, S. Plogmaker, M. Gorgoi, S. Svensson, H. Siegbahn, H. Rensmo. *J. Phys. Chem. C* **114**, 10314 (2010).
64. D. M. Dattelbaum, E. M. Kober, J. M. Papanikolas, T. J. Meyer. *Chem. Phys.* **326**, 71 (2006).
65. J. R. Schoonover, D. M. Dattelbaum, A. Malko, V. I. Klimov, T. J. Meyer, D. J. Styers-Barnett, E. Z. Gannon, J. C. Granger, W. S. Aldridge, J. M. Papanikolas. *J. Phys. Chem. A* **109**, 2472 (2005).
66. W. H. Elfring, G. A. Crosby. *J. Am. Chem. Soc.* **103**, 2683 (1981).
67. E. M. Kober, T. J. Meyer. *Inorg. Chem.* **23**, 3877 (1984).
68. G. D. Hager, R. J. Watts, G. A. Crosby. *J. Am. Chem. Soc.* **97**, 7037 (1975).
69. R. A. Malone, D. F. Kelley. *J. Chem. Phys.* **95**, 8970 (1991).
70. C. Creutz, H. Taube. *J. Am. Chem. Soc.* **91**, 3988 (1969).
71. C. Creutz, H. Taube. *J. Am. Chem. Soc.* **95**, 1086 (1973).
72. K. D. Demadis, C. M. Hartshorn, T. J. Meyer. *Chem. Rev.* **101**, 2655 (2001).
73. J. J. Concepcion, D. M. Dattelbaum, T. J. Meyer, R. C. Rocha. *Philos. Trans. R. Soc., Ser. A* **366**, 163 (2008).
74. S. Boyde, G. F. Strouse, W. E. Jones, T. J. Meyer. *J. Am. Chem. Soc.* **112**, 7395 (1990).

75. G. F. Strouse, J. R. Schoonover, R. Duesing, S. Boyde, W. E. Jones Jr., T. J. Meyer. *Inorg. Chem.* **34**, 473 (1995).
76. N. H. Damrauer, T. R. Boussie, M. Devenney, J. K. McCusker. *J. Am. Chem. Soc.* **119**, 8253 (1997).
77. N. H. Damrauer, B. T. Weldon, J. K. McCusker. *J. Phys. Chem. A* **102**, 3382 (1998).
78. D. M. Dattelbaum, C. M. Hartshorn, T. J. Meyer. *J. Am. Chem. Soc.* **124**, 4938 (2002).
79. A. T. Yeh, C. V. Shank, J. K. McCusker. *Science* **289**, 935 (2000) and refs. therein.
80. H. Yersin, W. Humbs, J. Strasser. *Coord. Chem. Rev.* **159**, 325 (1997) and refs. therein.
81. M. K. De Armond, M. L. Myrick. *Acc. Chem. Res.* **22**, 364 (1989).
82. T. J. Meyer. *Pure Appl. Chem.* **58**, 1193 (1986).
83. M.-E. Moret, I. Tavernelli, M. Chergui, U. Rothlisberger. *Chem.—Eur. J.* **16**, 5889 (2010).
84. E. M. Kober, B. P. Sullivan, T. J. Meyer. *Inorg. Chem.* **23**, 2098 (1984).
85. D. H. Oh, S. G. Boxer. *J. Am. Chem. Soc.* **111**, 1130 (1989).
86. J. V. Caspar, T. D. Westmoreland, G. H. Allen, P. G. Bradley, T. J. Meyer, W. H. Woodruff. *J. Am. Chem. Soc.* **106**, 3492 (1984).
87. R. F. Dallinger, W. H. Woodruff. *J. Am. Chem. Soc.* **101**, 4391 (1979).
88. P. G. Bradley, N. Kress, B. A. Hornberger, R. F. Dallinger, W. H. Woodruff. *J. Am. Chem. Soc.* **103**, 7441 (1981).
89. K. M. Omberg, J. R. Schoonover, S. Bernhard, J. A. Moss, J. A. Treadway, E. M. Kober, R. B. Dyer, T. J. Meyer. *Inorg. Chem.* **37**, 3505 (1998).
90. A. B. P. Lever. *Inorg. Chem.* **29**, 1271 (1990).
91. H. Masui, A. B. P. Lever. *Inorg. Chem.* **32**, 2199 (1993).
92. S. S. Fielder, M. C. Osborne, A. B. P. Lever, W. J. Pietro. *J. Am. Chem. Soc.* **117**, 6990 (1995).
93. P. A. Anderson, G. F. Strouse, J. A. Treadway, F. R. Keene, T. J. Meyer. *Inorg. Chem.* **33**, 3863 (1994).
94. P. A. Anderson, F. R. Keene, T. J. Meyer, J. A. Moss, G. F. Strouse, J. A. Treadway. *J. Chem. Soc., Dalton Trans.* 3820 (2002).
95. S. K. Doorn, J. T. Hupp. *J. Am. Chem. Soc.* **111**, 4704 (1989).
96. W. Gawelda, M. Johnson, F. M. F. de Groot, R. Abela, C. Bressler, M. Chergui. *J. Am. Chem. Soc.* **128**, 5001 (2006).
97. K. D. Demadis, D. M. Dattelbaum, E. M. Kober, J. J. Concepcion, J. J. Paul, T. J. Meyer, P. S. White. *Inorg. Chim. Acta* **360**, 1143 (2007).
98. K. Huang, A. Rhys. *Proc. R. Soc. London, Ser. A* **204**, 406 (1950).
99. C. J. Ballhausen. *Molecular Electronic Structures of Transition Metal Complexes*, McGraw-Hill, New York (1979).
100. K. Maruszewski, K. Bajdor, D. P. Strommen, J. R. Kincaid. *J. Phys. Chem.* **99**, 6286 (1995).
101. G. H. Allen, R. P. White, D. P. Rillema, T. J. Meyer. *J. Am. Chem. Soc.* **106**, 2613 (1984).
102. R. S. Lumpkin, T. J. Meyer. *J. Phys. Chem.* **90**, 5307 (1986).
103. K. R. Barqawi, A. Llobet, T. J. Meyer. *J. Am. Chem. Soc.* **110**, 7751 (1988).
104. H.-B. Kim, N. Kitamura, S. Tazuke. *J. Phys. Chem.* **94**, 7401 (1990).
105. K. R. Barqawi, Z. Murtaza, T. J. Meyer. *J. Phys. Chem.* **95**, 47 (1991).
106. D. P. Rillema, C. B. Blanton, R. J. Shaver, D. C. Jackman, M. Boldaji, S. Bundy, L. A. Worl, T. J. Meyer. *Inorg. Chem.* **31**, 1600 (1992).
107. E. M. Kober, J. V. Caspar, R. S. Lumpkin, T. J. Meyer. *J. Phys. Chem.* **90**, 3722 (1986).
108. L. A. Worl, R. Duesing, P. Y. Chen, L. Dellaciana, T. J. Meyer. *J. Chem. Soc., Dalton Trans.* 849 (1991).
109. S.-Y. Lee, E. J. Heller. *J. Chem. Phys.* **71**, 4777 (1979).
110. E. J. Heller. *Acc. Chem. Res.* **14**, 368 (1981).
111. E. J. Heller, R. Sundberg, D. Tannor. *J. Phys. Chem.* **86**, 1822 (1982).
112. E. J. Heller, R. C. Brown. *J. Chem. Phys.* **79**, 3336 (1983).

113. D. G. Thompson, J. R. Schoonover, C. J. Timpson, T. J. Meyer. *J. Phys. Chem. A* **107**, 10250 (2003).
114. J. M. Butler, M. W. George, J. R. Schoonover, D. M. Dattelbaum, T. J. Meyer. *Coord. Chem. Rev.* **251**, 492 (2007).
115. J. R. Schoonover, K. C. Gordon, R. Argazzi, W. H. Woodruff, C. A. Bignozzi, R. B. Dyer, T. J. Meyer, K. A. Peterson. *J. Am. Chem. Soc.* **115**, 10996 (1993).
116. D. M. Dattelbaum, T. J. Meyer. *J. Phys. Chem. A* **106**, 4519 (2002).
117. D. M. Dattelbaum, K. M. Omberg, J. R. Schoonover, R. L. Martin, T. J. Meyer. *Inorg. Chem.* **41**, 6071 (2002).
118. A. Vlček Jr., S. Zálíš. *Coord. Chem. Rev.* **251**, 258 (2007).
119. A. Vlček Jr. In *Photophysics of Organometallics*, A. J. Lees (Eds.), p. 115, Springer, Berlin (2010).
120. D. M. Dattelbaum, R. L. Martin, J. R. Schoonover, T. J. Meyer. *J. Phys. Chem. A* **108**, 3518 (2004).
121. D. M. Dattelbaum, K. M. Omberg, P. J. Hay, N. L. Gebhart, R. L. Martin, J. R. Schoonover, T. J. Meyer. *J. Phys. Chem. A* **108**, 3527 (2004).
122. P. Chen, T. J. Meyer. *Chem. Rev.* **98**, 1439 (1998).
123. J. Ulstrup. *Charge Transfer Processes in Condensed Media*, Springer, New York (1979).
124. R. A. Marcus, N. Sutin. *Biochim. Biophys. Acta* **811**, 265 (1985).
125. K. K. Stavrev, M. C. Zerner, T. J. Meyer. *J. Am. Chem. Soc.* **117**, 8684 (1995).
126. J. C. Curtis, B. P. Sullivan, T. J. Meyer. *Inorg. Chem.* **22**, 224 (1983).
127. C. J. Timpson, C. A. Bignozzi, B. P. Sullivan, E. M. Kober, T. J. Meyer. *J. Phys. Chem.* **100**, 2915 (1996).
128. J. Ridley, M. Zerner. *Theor. Chim. Acta* **32**, 111 (1973).
129. A. Bacon, M. Zerner. *Theor. Chim. Acta* **53**, 21 (1979).
130. M. C. Zerner, G. H. Loew, R. F. Kirchner, U. T. Mueller-Westerhoff. *J. Am. Chem. Soc.* **102**, 589 (1980).
131. M. M. Karelson, M. C. Zerner. *J. Phys. Chem.* **96**, 6949 (1992).
132. J. Zeng, N. S. Hush, J. R. Reimers. *J. Phys. Chem.* **99**, 10459 (1995).
133. J. Zeng, N. S. Hush, J. R. Reimers. *J. Phys. Chem.* **100**, 19292 (1996).
134. J. Zeng, N. S. Hush, J. R. Reimers. *J. Am. Chem. Soc.* **118**, 2059 (1996).
135. V. Gutmann. *The Donor-Acceptor Approach to Molecular Interactions*, Plenum, New York (1978).
136. Y. Kawanishi, N. Kitamura, S. Tazuke. *Inorg. Chem.* **28**, 2968 (1989).
137. J. N. Demas, D. G. Taylor. *Inorg. Chem.* **18**, 3177 (1979).
138. R. S. Lumpkin, E. M. Kober, L. A. Worl, Z. Murtaza, T. J. Meyer. *J. Phys. Chem.* **94**, 239 (1990).
139. A. Harriman, G. Izzet. *Phys. Chem. Chem. Phys.* **9**, 944 (2007).
140. A. E. Friedman, J. C. Chambron, J. P. Sauvage, N. J. Turro, J. K. Barton. *J. Am. Chem. Soc.* **112**, 4960 (1990).
141. W. Chen, C. Turro, L. A. Friedman, J. K. Barton, N. J. Turro. *J. Phys. Chem. B* **101**, 6995 (1997).
142. B. M. Zeglis, V. C. Pierre, J. K. Barton. *Chem. Commun.* 4565 (2007).
143. M. H. Lim, H. Song, E. D. Olmon, E. E. Dervan, J. K. Barton. *Inorg. Chem.* **48**, 5392 (2009).
144. M. K. Brennaman, J. H. Alstrum-Acevedo, C. N. Fleming, P. Jang, T. J. Meyer, J. M. Papanikolas. *J. Am. Chem. Soc.* **124**, 15094 (2002).
145. M. K. Brennaman, T. J. Meyer, J. M. Papanikolas. *J. Phys. Chem. A* **108**, 9938 (2004).
146. P. C. Ford, D. Wink, J. Dibenedetto. In *Prog. Inorg. Chem.*, p. 213, John Wiley (1983).
147. J. R. Winkler, T. L. Netzel, C. Creutz, N. Sutin. *J. Am. Chem. Soc.* **109**, 2381 (1987).
148. B. Durham, J. L. Walsh, C. L. Carter, T. J. Meyer. *Inorg. Chem.* **19**, 860 (1980).
149. B. Durham, J. V. Caspar, J. K. Nagle, T. J. Meyer. *J. Am. Chem. Soc.* **104**, 4803 (1982).
150. D. V. Pinnick, B. Durham. *Inorg. Chem.* **23**, 1440 (1984).

151. D. V. Pinnick, B. Durham. *Inorg. Chem.* **23**, 3841 (1984).
152. L. J. Henderson, W. R. Cherry. *Chem. Phys. Lett.* **114**, 553 (1985).
153. J. T. Hupp, G. A. Neyhart, T. J. Meyer, E. M. Kober. *J. Phys. Chem.* **96**, 10820 (1992).
154. A. B. P. Lever. *Inorganic Electronic Spectroscopy*, Elsevier, Amsterdam (1984).
155. C. Brady, J. McGarvey, J. McCusker, H. Toftlund, D. Hendrickson. In *Spin Crossover in Transition Metal Compounds III*, P. Gütllich, H. A. Goodwin (Eds.), p. 1, Springer, Berlin (2004).
156. E. A. Juban, A. L. Smeigh, J. E. Monat, J. K. McCusker. *Coord. Chem. Rev.* **250**, 1783 (2006).
157. G. H. Allen, B. P. Sullivan, T. J. Meyer. *J. Chem. Soc., Chem. Commun.* 793 (1981).
158. J. R. Schoonover, G. F. Strouse, R. B. Dyer, W. D. Bates, P. Chen, T. J. Meyer. *Inorg. Chem.* **35**, 273 (1996).
159. T. J. Meyer, J. V. Caspar. *Chem. Rev.* **85**, 187 (1985).
160. K. Suzuki, A. Kobayashi, S. Kaneko, K. Takehira, T. Yoshihara, H. Ishida, Y. Shiina, S. Oishi, S. Tobita. *Phys. Chem. Chem. Phys.* **11**, 9850 (2009).
161. H. Ishida, S. Tobita, Y. Hasegawa, R. Katoh, K. Nozaki. *Coord. Chem. Rev.* **254**, 2449 (2010).
162. J. Van Houten, R. J. Watts. *J. Am. Chem. Soc.* **97**, 3843 (1975).
163. J. Van Houten, R. J. Watts. *J. Am. Chem. Soc.* **98**, 4853 (1976).
164. A. Cannizzo, F. van Mourik, W. Gawelda, G. Zgrablic, C. Bressler, M. Chergui. *Angew. Chem., Int. Ed.* **45**, 3174 (2006).
165. W. Henry, C. G. Coates, C. Brady, K. L. Ronayne, P. Matousek, M. Towrie, S. W. Botchway, A. W. Parker, J. G. Vos, W. R. Browne, J. J. McGarvey. *J. Phys. Chem. A* **112**, 4537 (2008).
166. S. Yoon, P. Kukura, C. M. Stuart, R. A. Mathies. *Mol. Phys.* **104**, 1275 (2006).
167. M. L. Horng, J. A. Gardecki, A. Papazyan, M. Maroncelli. *J. Phys. Chem.* **99**, 17311 (1995).
168. G. A. Voth, R. M. Hochstrasser. *J. Phys. Chem.* **100**, 13034 (1996) and refs. therein.
169. M. Maroncelli. *J. Mol. Liq.* **57**, 1 (1993).
170. L. F. Cooley, P. Bergquist, D. F. Kelley. *J. Am. Chem. Soc.* **112**, 2612 (1990).
171. N. H. Damrauer, G. Cerullo, A. Yeh, T. R. Boussie, C. V. Shank, J. K. McCusker. *Science* **275**, 54 (1997).
172. J. K. McCusker. *Acc. Chem. Res.* **36**, 876 (2003).
173. G. B. Shaw, C. L. Brown, J. M. Papanikolas. *J. Phys. Chem. A* **106**, 1483 (2002).
174. G. B. Shaw, D. J. Styers-Barnett, E. Z. Gannon, J. C. Granger, J. M. Papanikolas. *J. Phys. Chem. A* **108**, 4998 (2004).
175. R. Englman, J. Jortner. *Mol. Phys.* **18**, 145 (1970).
176. K. F. Freed, J. Jortner. *J. Chem. Phys.* **52**, 6272 (1970).
177. J. V. Caspar, E. M. Kober, B. P. Sullivan, T. J. Meyer. *J. Am. Chem. Soc.* **104**, 630 (1982).
178. J. V. Caspar, B. P. Sullivan, E. M. Kober, T. J. Meyer. *Chem. Phys. Lett.* **91**, 91 (1982).
179. J. V. Caspar, T. J. Meyer. *J. Phys. Chem.* **87**, 952 (1983).
180. W. J. Vining, J. V. Caspar, T. J. Meyer. *J. Phys. Chem.* **89**, 1095 (1985).
181. S. R. Johnson, T. D. Westmoreland, J. V. Caspar, K. R. Barqawi, T. J. Meyer. *Inorg. Chem.* **27**, 3195 (1988).
182. E. W. Schlag, S. Schneider, S. F. Fischer. *Annu. Rev. Phys. Chem.* **22**, 465 (1971).
183. K. F. Freed. *Acc. Chem. Res.* **11**, 74 (1978).
184. M. Bixon, J. Jortner, J. Cortes, H. Heitele, M. E. Michel-Beyerle. *J. Phys. Chem.* **98**, 7289 (1994).
185. J. V. Caspar, T. J. Meyer. *Inorg. Chem.* **22**, 2444 (1983).
186. J. V. Caspar, T. J. Meyer. *J. Am. Chem. Soc.* **105**, 5583 (1983).
187. D. W. Thompson, C. N. Fleming, B. D. Myron, T. J. Meyer. *J. Phys. Chem. B* **111**, 6930 (2007).
188. P. Y. Chen, R. Duesing, D. K. Graff, T. J. Meyer. *J. Phys. Chem.* **95**, 5850 (1991).
189. Y. Liu, D. B. Turner, T. N. Singh, A. M. Angeles-Boza, A. Chouai, K. R. Dunbar, C. Turro. *J. Am. Chem. Soc.* **131**, 26 (2008).
190. D. W. Thompson, J. F. Wishart, B. S. Brunshwig, N. Sutin. *J. Phys. Chem. A* **105**, 8117 (2001).

191. K. F. Mongey, J. G. Vos, B. D. MacCraith, C. M. McDonagh. *Coord. Chem. Rev.* **185–186**, 417 (1999).
192. G. D. Hager, G. A. Crosby. *J. Am. Chem. Soc.* **97**, 7031 (1975).
193. D. A. Duddell, R. J. Morris, J. T. Richards. *J. Chem. Soc., Chem. Commun.* 75 (1979).
194. A. A. Bhuiyan, J. R. Kincaid. *Inorg. Chem.* **37**, 2525 (1998).
195. J. R. Kincaid. *Chem.—Eur. J.* **6**, 4055 (2000).
196. T. E. Knight, A. P. Goldstein, M. K. Brennaman, T. Cardolaccia, A. Pandya, J. M. DeSimone, T. J. Meyer. *J. Phys. Chem. B* **115**, 64 (2011).
197. D. P. Rillema, G. Allen, T. J. Meyer, D. Conrad. *Inorg. Chem.* **22**, 1617 (1983).
198. B. J. Coe, D. W. Thompson, C. T. Culbertson, J. R. Schoonover, T. J. Meyer. *Inorg. Chem.* **34**, 3385 (1995).
199. T. J. Meyer. *Prog. Inorg. Chem.* **30**, 389 (1983) and refs. therein.
200. C. R. Bock, T. J. Meyer, D. G. Whitten. *J. Am. Chem. Soc.* **97**, 2909 (1975).
201. C. R. Bock, J. A. Connor, A. R. Gutierrez, T. J. Meyer, D. G. Whitten, B. P. Sullivan, J. K. Nagle. *Chem. Phys. Lett.* **61**, 522 (1979).
202. Z. Murtaza, A. P. Zipp, L. A. Worl, D. Graff, W. E. Jones, W. D. Bates, T. J. Meyer. *J. Am. Chem. Soc.* **113**, 5113 (1991).
203. Z. Murtaza, D. K. Graff, A. P. Zipp, L. A. Worl, W. E. Jones, W. D. Bates, T. J. Meyer. *J. Phys. Chem.* **98**, 10504 (1994).
204. M. Eigen. *Z. Phys. Chem. (Frankfurt am Main)* **1**, 176 (1954).
205. R. M. Fuoss. *J. Am. Chem. Soc.* **80**, 5059 (1958).
206. N. R. Kestner, J. Logan, J. Jortner. *J. Phys. Chem.* **78**, 2148 (1974).
207. J. Ulstrup, J. Jortner. *J. Chem. Phys.* **63**, 4358 (1975).
208. K. S. Schanze, D. Brent MacQueen, T. A. Perkins, L. A. Cabana. *Coord. Chem. Rev.* **122**, 63 (1993).
209. M. H. V. Huynh, D. M. Dattelbaum, T. J. Meyer. *Coord. Chem. Rev.* **249**, 457 (2005).
210. B. P. Sullivan, H. Abruna, H. O. Finklea, D. J. Salmon, J. K. Nagle, T. J. Meyer, H. Sprintschnik. *Chem. Phys. Lett.* **58**, 389 (1978).
211. T. D. Westmoreland, K. S. Schanze, P. E. Neveux, E. Danielson, B. P. Sullivan, P. Chen, T. J. Meyer. *Inorg. Chem.* **24**, 2596 (1985).
212. P. Y. Chen, T. D. Westmoreland, E. Danielson, K. S. Schanze, D. Anthon, P. E. Neveux, T. J. Meyer. *Inorg. Chem.* **26**, 1116 (1987).
213. J. A. Treadway, P. Chen, T. J. Rutherford, F. R. Keene, T. J. Meyer. *J. Phys. Chem. A* **101**, 6824 (1997).
214. C. Weinheimer, Y. Choi, T. Caldwell, P. Gresham, J. Olmsted III. *J. Photochem. Photobiol. A: Chem.* **78**, 119 (1994).
215. J. N. Younathan, S. F. McClanahan, T. J. Meyer. *Macromolecules* **22**, 1048 (1989).
216. L. A. Worl, G. F. Strouse, J. N. Younathan, S. M. Baxter, T. J. Meyer. *J. Am. Chem. Soc.* **112**, 7571 (1990).
217. J. N. Younathan, W. E. Jones, T. J. Meyer. *J. Phys. Chem.* **95**, 488 (1991).
218. W. E. Jones, S. M. Baxter, G. F. Strouse, T. J. Meyer. *J. Am. Chem. Soc.* **115**, 7363 (1993).
219. L. A. Worl, W. E. Jones, G. F. Strouse, J. N. Younathan, E. Danielson, K. A. Maxwell, M. Sykora, T. J. Meyer. *Inorg. Chem.* **38**, 2705 (1999).
220. G. F. Strouse, L. A. Worl, J. N. Younathan, T. J. Meyer. *J. Am. Chem. Soc.* **111**, 9101 (1989).
221. S. M. Baxter, W. E. Jones, E. Danielson, L. Worl, G. Strouse, J. Younathan, T. J. Meyer. *Coord. Chem. Rev.* **111**, 47 (1991).
222. L. M. Dupray, T. J. Meyer. *Inorg. Chem.* **35**, 6299 (1996).
223. D. A. Friesen, T. Kajita, E. Danielson, T. J. Meyer. *Inorg. Chem.* **37**, 2756 (1998).
224. C. N. Fleming, L. M. Dupray, J. M. Papanikolas, T. J. Meyer. *J. Phys. Chem. A* **106**, 2328 (2002).

225. M. Sykora, K. A. Maxwell, J. M. DeSimone, T. J. Meyer. *Proc. Natl. Acad. Sci. USA* **97**, 7687 (2000).
226. P. M. Cowan, S. McGavin. *Nature* **176**, 501 (1955).
227. W. Traub, U. Shmueli. *Nature* **198**, 1165 (1963).
228. C. A. Slate. Ph.D. dissertation, The University of North Carolina at Chapel Hill (1997).
229. D. G. McCafferty, D. A. Friesen, E. Danielson, C. G. Wall, M. J. Saderholm, B. W. Erickson, T. J. Meyer. *Proc. Natl. Acad. Sci. USA* **93**, 8200 (1996).
230. D. R. Striplin, S. Y. Reece, D. G. McCafferty, C. G. Wall, D. A. Friesen, B. W. Erickson, T. J. Meyer. *J. Am. Chem. Soc.* **126**, 5282 (2004).
231. S. A. Serron, W. S. Aldridge, C. N. Fleming, R. M. Danell, M. H. Baik, M. Sykora, D. M. Dattelbaum, T. J. Meyer. *J. Am. Chem. Soc.* **126**, 14506 (2004).
232. M. K. Brennaman, C. N. Fleming, C. A. Slate, S. A. Serron, S. E. Bettis, B. W. Erickson, J. M. Papanikolas, T. J. Meyer. *J. Phys. Chem. B* **117**, 6352 (2013).
233. H. Gerischer, M. E. Michel-Beyerle, F. Reberstrost, H. Tributsch. *Electrochim. Acta* **13**, 1509 (1968).
234. H. Tsubomura, M. Matsumura, Y. Nomura, T. Amamiya. *Nature* **261**, 402 (1976).
235. D. Duonghond, N. Serpone, M. Grätzel. *Helv. Chim. Acta* **67**, 1012 (1984).
236. J. Desilvestro, M. Grätzel, L. Kavan, J. Moser, J. Augustynski. *J. Am. Chem. Soc.* **107**, 2988 (1985).
237. B. O'Regan, M. Grätzel. *Nature* **353**, 737 (1991).
238. M. Grätzel. *J. Photochem. Photobiol. C: Photochem. Rev.* **4**, 145 (2003).
239. R. Jose, V. Thavasi, S. Ramakrishna. *J. Am. Ceram. Soc.* **92**, 289 (2009).
240. A. Yella, H.-W. Lee, H. N. Tsao, C. Yi, A. K. Chandiran, M. K. Nazeeruddin, E. W.-G. Diao, C.-Y. Yeh, S. M. Zakeeruddin, M. Grätzel. *Science* **334**, 629 (2011).
241. W. Song, Z. Chen, M. K. Brennaman, J. J. Concepcion, A. O. T. Patrocinio, N. Y. Murakami Iha, T. J. Meyer. *Pure Appl. Chem.* **83**, 749 (2011).
242. W. J. Youngblood, S.-H. A. Lee, Y. Kobayashi, E. A. Hernandez-Pagan, P. G. Hoertz, T. A. Moore, A. L. Moore, D. Gust, T. E. Mallouk. *J. Am. Chem. Soc.* **131**, 926 (2009).
243. W. J. Youngblood, S.-H. A. Lee, K. Maeda, T. E. Mallouk. *Acc. Chem. Res.* **42**, 1966 (2009).
244. W. Song, M. K. Brennaman, J. J. Concepcion, J. W. Jurss, P. C. Hoertz, H. Luo, C. Chen, K. Hanson, T. J. Meyer. *J. Phys. Chem. C* **115**, 7081 (2011).
245. H. Luo, W. Song, P. G. Hoertz, K. Hanson, R. Ghosh, S. Rangan, M. K. Brennaman, J. J. Concepcion, R. A. Binstead, R. A. Bartynski, R. Lopez, T. J. Meyer. *Chem. Mater.* **25**, 122 (2013).